ABSTRACT

Title of Document: SYNTHESIS AND CHARACTERIZATION OF LOW-VALENT ALUMINUM AND GALLIUM COMPOUNDS FROM METASTABLE ALUMINUM (I) AND GALLIUM (I) PRECURSORS

Dennis H. Mayo
Doctor of Philosophy, 2011

Directed By: Professor Bryan W. Eichhorn
Department of Chemistry and Biochemistry

In this thesis the design, assembly, and operation of a metal halide co-condensation reactor capable of generating metastable solutions of aluminum and gallium monohalides is described. In this reactor, gas-phase molecules are co-condensed with a mixed solvent at 77 K and the resultant metastable solutions are stored at 198 K. Upon warming, these solutions undergo disproportionation reactions to form metalloid cluster compounds. The optimization of multiple reactor settings for monohalide generation is described. The efficacy of the reactor was validated by reproducing the synthesis of large clusters of Ga and Al; namely $[Al_{77}(NTMS_2)_{20}]^{2-}$ and $[Ga_{12}Br_2(GaBrNTMS_2)_{10}]^{2-}$ which were first described by Schnockel *et al*.

In order to better understand the challenges of low-valent aluminum and gallium chemistry a comprehensive literature review is presented. This review describes the synthetic pathways by which low-valent aluminum and gallium compounds are prepared,

as well as in-depth discussion of structural and spectroscopic properties of these compounds.

Two new low oxidation state Al_3 clusters have been prepared by the reaction of lithium phosphides with metastable $AlCl{\bullet}Et_2O$. Both of these compounds have the general formula $Li_2[Al_3(PR_2)_6]{\bullet}2\ Et_2O$ (where R = C_6H_5 or C_6H_{11}) and formally contain $Al^{+1.3}$ ions . These compounds have been characterized by X-ray diffraction and their paramagnetic nature probed by ^1H NMR (Evans method) and EPR spectroscopy. The aluminum hydride cluster $[Al_3H_6]^{2-}$ has been modeled by DFT calculations (6–31G*, Hyperchem) to visualize the molecular orbitals in the $[Al_3(PR)_6]^{2-}$ clusters.

The preparation of three novel aluminum (III) amidinate compounds is described. These compounds ($Al(PhC(N^iPr)_2)_3$, $Al(PhC(N^iPr)_2)_2Cl$, and $Al(PhC(NCy)_2)_2Cl$) are formed as the result of ligand-exchange and disproportionation processes that occur during the reaction of lithium amidinates with metastable $AlCl{\bullet}Et_2O$. The synthesis of the gallium dimer $Ga_2Br_4{\bullet}2\ PHCy_2$ is also described.

SYNTHESIS AND CHARACTERIZATION OF LOW-VALENT ALUMINUM AND GALLIUM COMPOUNDS FROM METASTABLE ALUMINUM (I) AND GALLIUM (I) PRECURSORS

by

Dennis H. Mayo

Dissertation submitted to the Faculty of the Graduate School of the
University of Maryland, College Park, in partial fulfillment
of the requirements for the degree of
Doctor of Philosophy
2011

Advisory Committee:
Professor Jeffrey T. Davis, Chair
Professor Bryan W. Eichhorn, Advisor
Professor Hugh Bruck, Dean's Representative
Professor Dorothy Beckett
Professor Janice Reutt-Robey

Acknowledgements

My sincerest thanks go to advisor, Prof. Bryan Eichhorn. I showed up in his office one day asking for an opportunity to work on a project; I'm not sure either of us knew how things would end up. I knew that we would be starting a project together, but that was all. I'm extremely fortunate to have worked with someone that I could relate to, look up to, and be unabashedly honest with. I hope that I have made a positive impact during the time that I have spent in the lab – I certainly have grown as an experimentalist and as a person during my time in Bryan's lab, and imagine I'll look back on my time with Bryan fondly.

I'd like to thank my coworkers in the Eichhorn Labs – Selim Alayoglu, Pavan Bellamkonda, Tony Dylla, Zhufang Liu, Chris Sims, Chunjuan Zhang, Yi Yu, Aldo Ponce, Sanem Kocak, Domonique Downing, Yang Peng and Samantha DeCarlo. Your support, help, and camaraderie have been invaluable. I'd like to especially thank Sanem, Domonique, Yang, and Sam for challenging and teaching me and for making me feel strong because I'm able to open bottles and gas tanks.

My thanks go to Professor Kit Bowen and Dr. Xiang Li at The Johns Hopkins University. It was their hard work, assistance, and patience that helped us build and assemble our Schnöckelator. Thanks to Dr. Peter Zavalij for being able to solve our crystal data and Dr. Yiu-Fai Lam for discussions and help with NMR experiments. I'm also very grateful that Dr. J.J. Yin at the FDA has been so willing to work with me on short notice in obtaining EPR spectra.

I'd like to thank the American Society for Engineering Education and the SMART Fellowship Program. I can't imagine a better situation than the one I've been fortunate enough to be in. Thanks to everyone at ASEE and also at the Naval Postgraduate School

for your outreach, involvement, and assistance. Thanks to Dr. Chad Stoltz and Dr. Jim Lightstone at the Indian Head Division, Naval Surface Warfare Center. It was with your involvement that I came across this research project, and for that I am grateful.

I'd like to acknowledge the fine folks at The College Board, on whose AP Chemistry Exam I 'earned' a 1 out of 5 as a junior in high school. Thanks for the motivation.

I would also like to thank the many members of my incoming cohort at Maryland, including Seth Thomas, Fred Nytko, Matthew Hurley, Derick Lucas, Irene Kiburu, and Yu Liu, and all of the other graduate students and postdocs in our department. I've been extremely fortunate to have been surrounded by so many truly wonderful people.

I'd like to thank my parents for their encouragement and support. As far back as I can remember I've been given free rein to explore and learn everything I've wanted. Ever since the second grade, when my father gave a class presentation about acids and bases, I've been aware of acids and bases and somewhat aware of chemistry. Thanks for nudging me along a decent path.

Lastly, I'd like to thank my wife Kate. Without her patience and resolve I doubt I would have made it through graduate school. It hasn't always been the easiest getting through school but I'm ever grateful for her willingness to keep going – even if it meant spending a little more time in graduate school. *Le grá go deo*.

Table of Contents

List of Tables.

List of Figures and Schemes

Abbreviations.

Ar'	C_6H_3-2,6-(C_6H_3-2,6-iPr_2)$_2$
Ar''	C_6H_3-2,6-(C_6H_2-2,4,6-Me_3)$_2$)
Ar*	2,6-$Trip_2C_6H_3$
Cp	Cyclopentadienyl, C_5H_5
Cp*	Pentamethylcyclopentadienyl, $C_5(CH_3)_5$
Cy	Cyclohexyl, C_6H_{11}
Dipp	2,6-$^{i}Pr_2$-C_6H_3
EPR	Electron Paramagnetic Resonance
ESI	Electrospray Ionization
Et_2O	Diethyl ether, $C_4H_{10}O$
^{i}Pr	Isopropyl, $CH(CH_3)_2$
IPr	:C{(DippNCH)$_2$}
JHU	The Johns Hopkins University
KIT	Karlruhe Institute of Technology
Me	Methyl, CH_3
MFC	Mass Flow Controller
MHCR	Metal Halide Co-condensation Reactor
MO	Molecular Orbital
Nacnac	$[N(Dipp)C(Me)]_2CH]^-$
NEt_3	Triethylamine
NHC	N-Heterocyclic Carbene
NMR	Nuclear Magnetic Resonance
Ph	Phenyl, C_6H_5
Priso	$[(DippN)_2CR]_2N^{i}Pr_2$
^{t}Bu	tert-Butyl, $C(CH_3)_3$

THF	Tetrahydrofuran, C_4H_8O
TMS	Trimethylsilyl, $Si(CH_3)_3$
Trip	2,4,6-triisopropylphenyl
UMD	University of Maryland, College Park

1. Introduction.

In recent years there has been a renaissance in main group chemistry. This expansion of focus on main-group elements has been a boon to scientists in numerous fields, including chemistry, physics, and engineering. Semiconductors (including CdSe, CdTe, and GaAs quantum dots), photovoltaics, and superconducting materials have all been advanced due to a greater understanding of main-group chemistry.

As our knowledge of the chemical world has become increasingly developed, the 'typical' chemistries of most elements have become well-established. For example, typical aluminum chemistry involves the 0 and +3 oxidation states; for tin the typical chemistry involves the 0, +2, and +4 oxidation states. The atypical chemistries, however, are quite intriguing. In the context of main group chemistry, atypical chemistries often involve reduced oxidation states. While multiple oxidation states are common in the transition metals, the main group elements occur naturally in relatively few oxidation states. Catalytic processes involving transition or main-group metals often proceed via partially oxidized or reduced metal centers. By exploring reduced- or partially reduced-oxidation state compounds, insight into the main group elemental properties can be gained.

This study is focused on the reduced-state chemistry of aluminum and gallium. To better understand the challenges inherent to such chemistry a review of the general elemental (Section **1.1**), synthetic (Sections **1.2**) and structural properties (Section **1.3**) of aluminum and gallium is presented below.

1.1: Group 13 Elements – Boron, Aluminum, Gallium, Indium, Thallium.

The Group 13 elements are abundant on Earth and have found use in many applications. The chemistry of the Group 13 elements often occurs in the +3 oxidation state. However, boron's high relative electronegativity leads to a large degree of covalency in its compounds. This is manifested in rich borane chemistry, with boron forming hydrido species containing numerous B-B bonds. In the boranes the average boron oxidation state is typically around +1.

For the heavier Group 13 elements indium and thallium, the inert S-pair effect is prominent. As a result of weak element-element bonding due to poor orbital overlap and the large promotional energy of the s electrons, the +1 oxidation state is stabilized relative to the +3 state. The result is rich indium (I) and thallium (I) chemistry; numerous indium (I) and thallium (I) compounds are commercially available.[1]

Aluminum and gallium, however, do not have readily accessible reduced states. It is relevant, therefore, to discuss in brief the more 'typical' chemistries of these two elements.

1.1.1. Aluminum.

Aluminum metal is widely used as a structural material – computers, bicycles, foil, and many other common items are made from bulk aluminum metal. The alloys of aluminum are also important in many aspects of modern life: aluminum/nickel alloys are quite relevant in organic synthesis in the form of Raney Nickel; aluminum/magnesium alloys are important lightweight materials for the aerospace industry. Aluminum metal has a valence electronic configuration of $3s^2 3p^1$. It is highly oxophilic and electropositive (Pauling electronegativity value of 1.61).

In its oxidized form, aluminum forms numerous compounds, from the archetypical inorganic Al_2Cl_6 (aluminum trichloride), and Al_2O_3 (alumina, widely used as a ceramic), to organoaluminum compounds, such as triethylaluminum (commonly used as a co-catalyst in the Ziegler-Natta system) and Tebbe's Reagent ($Cp_2TiCH_2ClAlMe_2$, used in organic synthesis in the methylenation of carbonyl compounds). While a broad range of organoaluminum compounds are known, this chemistry is dominated by aluminum in the +3 oxidation state. Similarly, the aluminum found naturally on the earth is found primarily in minerals (e.g. gibbsite and diaspore), all containing aluminum in the +3 oxidation state. It is through industrial processes; primarily the Hall-Héroult process, that alumina is electrochemically converted to aluminum metal.

1.1.2. Gallium.

Metallic gallium is a low-melting silvery solid (T_m = 30 °C) that has few uses in its elemental form. Gallium forms low-melting alloys with most metals. Galinstan (Ga-In-Sn) is the most well-known of the gallium alloys, and is being used as a replacement for mercury in many applications.[2] Gallium (III) arsenides and nitrides are widely-used semiconductors, employed in integrated circuits.

1.2. Synthesis of Reduced Oxidation State Aluminum and Gallium Compounds.

This section focuses on synthetic pathways that have resulted in the formation of reduced-state (3 > oxidation state > 0) aluminum and gallium compounds. While not exhaustive, this section should serve as a representative sampling of the methods by which 'atypical' oxidation states are formed. Tables **1.1** and **1.2** are encyclopedic lists of nearly every reduced-state aluminum and gallium compound reported. Compounds discussed in this text are shown in bold.

Table 1.1: Reduced Oxidation State Aluminum Compounds

Formula	Al Atoms	Al Ox. State	Ref.
AlNacNac	1	1	3
Na_2[Ar'AlAlAr']	2	0	4
$Al_2[Si[C^tbu3]_3]_4$	2	2	5
Al_2Br_4•2Anisole	2	2	6
$[AlH_2(NHC)]_2$	2	2	7
Al_2Trip_4	2	2	8
$[Al_2Trip_4]^{\bullet-}$	2	1.5	8
$Al_2(Si^tBu_3)_4$	2	2	5
$Al_2(C(H)TMS_2)_4$	2	2	9
$Al_2(P^tBu_2)_4$	2	2	10
Na_2[AlAr"]$_3$	3	0.66	4
$Li_2[Al_3(PR_2)_6]$•2 Et_2O	3	1.33	This work
$(^tBu_3Si)_4Al_3$	3	1.33	11
[AlCp*]$_4$	4	1	12
[AlBr•NEt_3]$_4$	4	1	13
$Al_4(P^tBu_2)_6$	4	1.5	14
$[Al_2(O^tBu_2)_4]_2$	4	2	10
Al_5Br_7•5THF	5	1.4	15

$Cp^*_3Al_5I_6$	5	1.8	16
$[Al_7N[TMS_2]_6]^-$	7	0.714	17
$Al_7N[Me_2SiPh]_6$	7	0.857	18
$Al_8Br_8(P^tBu_2)_6$	8	1.75	19
$K_8Al_{12}(O^tBu)_{18}$	12	0.833	20
$Si@Al_{14}Cp^*_6$	14	0.428	21
$Si@Al_{14}(N(Dipp)TMS)_6$	14	0.428	22
$Al_{22}Cl_{20}D_{10}$	22	0.909	23
$Al_{50}Cp^*_{12}$	50	0.24	24
$Si@Al_{56}[N(dipp)TMS]_{12}$	56	0.214	25
$[Al_{69}[N(TMS_2)]_{18}]^{3-}$	69	0.217	26
$[Al_{77}[N(TMS_2)]20]^{3-}$	77	0.221	27

Table 1.2: Reduced Oxidation State Gallium Compounds

Formula	Ga Atoms	Ox. State	Ref
NacnacGa	1	1	28
$Cp^*GaCrCO_5$	1	1	29
$Ar^{\#}GaFeCO_4$	1	1	30
$Ga•3PPh_3^+ AlOR_4^-$	1	1	31
GaAr*	1	1	32
$GaAr^{\#}$	1	1	32
$NacnacGaFe(CO)_4$	1	1	32
$K_2[TripGa]_2Ga_2$	2	0	33
$[GaI_2PHCy_2]_2$	2	2	34
$[Ar^*Ga(I)]_2$	2	2	32
$Ga_2Br_4•2diox$	2	2	35
Na2[Ar'GaGaAr']	2	0	32
Ar'GaGaAr'	2	1	32
$(Ga(Ar^*)I)_2$	2	2	32

$(Ga(Ar^{\#})I)_2$	2	2	32
$(Ga(Ar')I)_2$	2	2	32
$[Ga_2Cp^*]^+$	2	1	36
$Ga_2(SiTMS_3)_2(SiTMS_2)_2$	2	2	37
$Ga_2(MeC(Ndipp)_2)_2I_2$	2	2	38
$Ga_2(C(H)TMS_2)_4$	2	2	39
$Ga_2(C(H)TMS_2)_2(acetate)_2$	2	2	40
Ga_2Trip_4	2	2	41
$[Ga_2Trip_4]^{\bullet-}$	2	1.5	41
$[Ga_2(SiTMS_3)_2(Ga(TMS)(SiTMS_3))SiTMS_2]^-$	3	2	37
$Ga_3(BuC(NCy)_2)_3I_2$	3	1.667	38
$Ga_4Cl_4(SiTMS_3)_4$	4	2	42
$[Ga_4(SiTMS_3)_3(TMS)(SiTMS)]^-$	4	1	43
$Ga_4(DippNTMS)_4$	4	1	44
$Ga_4(tmp)_4$	4	1	44
$Ga_4(CSiMe_2Et)_3)_4$	4	1	45
$Ga_4(SiTMS_3)_4$	4	1	46
$Ga_4(GeTMS_3)_4$	4	1	47
$[Na(THF)_2]_2[Ga_4(Si^tBu_3)_4]$	4	0.5	48
$Ga_4(C(H)TMS_2)_4$(1,6-hexanedicarboxylate)$_2$	4	2	49
Ga_5Cl_7•$5Et_2O$	5	1.4	50
$[Ga_6(SiPh_2Me)_8]^{2-}$	6	1	51
$[GaCp^*]_6$	6	1	52
$[Ga_2(CHTMS_2)_2F_2]_3$	6	2	53
$[Ga_2(CHTMS_2)_2(OH)_2]_3$	6	2	53
$[Ga_6(O(NTMS_2)_6]^-$	6	1.2	44
$[Ga_6(SiMePh_2)_8]^{2-}$	6	1	51
Ga_8Br_8•$6NEt_3$	8	1	54
$Ga_8(P^iPr_2)_8Cl_2$	8	1.25	55
$Ga_8(P^tBu_2)_8Cl_2$	8	1.25	55

$Ga_8(Si^tBu_3)_6$	8	0.75	56
Ga_8I_8•6 PEt_3	8	1	57
$Ga_8(Si^tBu_3)_6$	8	0.75	58
$Na_2Ga_8(Si^tBu3)_6$	8	0.5	58
$Ga_8(C(H)TMS_2)_8(squarate)_4$	8	2	59
$[Ga_9(SiTMS_3)_6]^-$	9	0.556	60
$Ga_9(^tBu)_9$	9	1	61
$[Ga_9(^tBu)_9]^{\bullet-}$	9	0.889	62
$Ga_{10}Br_{10}$•10 4-^{t}BuC_6H_4N	10	1	63
$Ga_{10}(SiTMS_3)_6$	10	0.6	64
$[Ga_{10}(SitBu_3)_6]^-$	10	0.5	64
$Ga_{11}Ar_4$"	11	0.364	32
$[Ga_{12}(fluorenyl)_{10}]^{2-}$	12	0.666	65
$Ga_{12}(PtBu_2)_6Br_2(nPrC(H)PBu_3)_2$	12	0.833	66
$[Ga_{13}(Si^tBu_3)_6]^-$	13	0.385	64
$Ga_{18}(Si^tBu_3)_8$	18	0.444	67
$Ga_{18}(Si^tBu_3)_8$	18	0.444	67
$[Ga_{19}(CTMS_3)_6]^-$	19	0.263	68
$Ga_{22}[P^tBu_2]_{12}$	22	0.545	69
$[Ga_{22}Br_{12}(N[TMS]_2)_{10}]^{2-}$	22	0.909	70
$[Ga_{22}Br_{11}(N[TMS]_2)_{10}]^-$	22	0.909	70
$[Ga_{22}(NTMS_2)_{10}]^{2-}$	22	0.364	71
$Ga_{22}(Si^tBu_3)_8$	22	0.364	67
$Ga_{22}(SiTMS_3)_8$	22	0.364	67
$Ga_{22}(GeTMS_3)_8$	22	0.364	47
$Ga_{22}(SiTMS_3)_8$	22	0.273	72
$Ga_{23}(NTMS_2)_{11}$	23	0.478	73
$Ga_{24}Br_{18}Se_2$	24	0.833	74
$Ga_{24}Br_{22}$•10THF	24	0.917	75
$[Ga_{26}(SiTMS_3)_8]^-$	26	0.269	76

$[Ga_{51}(P^tBu_2)_{14}Br_6]^{3-}$	51	0.333	77
$[Ga_{84}(NTMS_2)_{20}]^{4-}$	84	0.19	78

1.2.1: Binary Aluminum and Gallium Halides.

The archetypical binary compounds of a given element are those formed between any element E and the halogens with the formula E_nX_m (E = element, X = F, Cl, Br, I). For aluminum and gallium, the common form is that of EX_3.

1.2.1.1. Aluminum subhalides.

The only thermodynamically stable solid state binary phase formed between aluminum and the halogens is AlX_3 (see Figure **1.1**). Attempts to reduce these compounds with traditional reducing agents (alkali metals) fail to yield partially reduced aluminum halides – instead a stoichiometric amount of aluminum metal is formed along with one equivalent of MX.

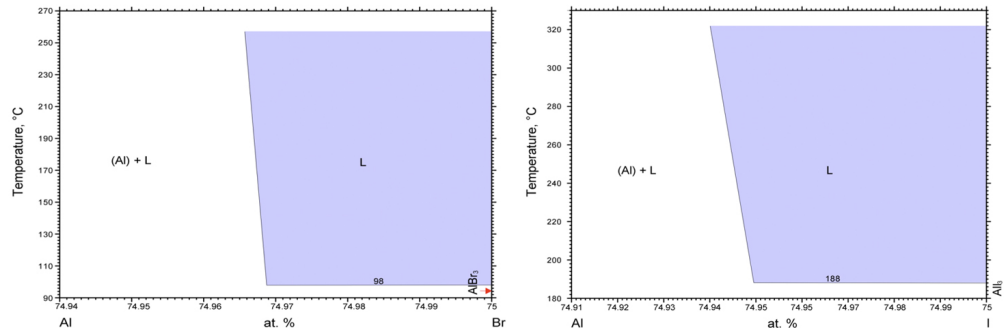

Figure 1.1: Binary phase diagrams for Al/Br (left) and Al/I (right). Adapted from ASM International Alloy Phase Diagrams Center. Single phase regions are represented in blue, biphasic regions in white.

1.2.1.2. Gallium subhalides.

In the case of gallium halides the thermodynamics are more amenable to formation of partially reduced forms. For gallium iodide there is a stable form of both GaI_2 and Ga_2I_3, as demonstrated in the Ga/I binary phase diagram (see Figure **1.2**).

Gallium subhalides were first reported in the 1950s by Worrall and coworkers. 'GaX_2' (X = Cl, Br, I) species were formed via a direct solid-liquid reaction between gallium metal and gallium trihalides at elevated temperatures (180-200 °C). While the reaction proceeded in a straightforward fashion, the yields are limited due to the product purification by sublimation.[79] (Equation **1.1**)

$$Ga_{(l)} + 2\ GaCl_{3\,(l)} \xrightarrow{200°C} 3\,GaCl_{2\,(s)} \qquad (1.1)$$

Twenty years after the initial reports, Worrall reported an improved synthetic method, employing conproportionation in solution rather than directly between elements.[80] By dissolving the reactants in benzene the reaction could be carried out at 60 °C and the products isolated as yellow powders. While this procedure is facile and straightforward, the lowest oxidation state subhalide formed by this method is Ga_2I_3, a compound with the average oxidation state of +1.5.

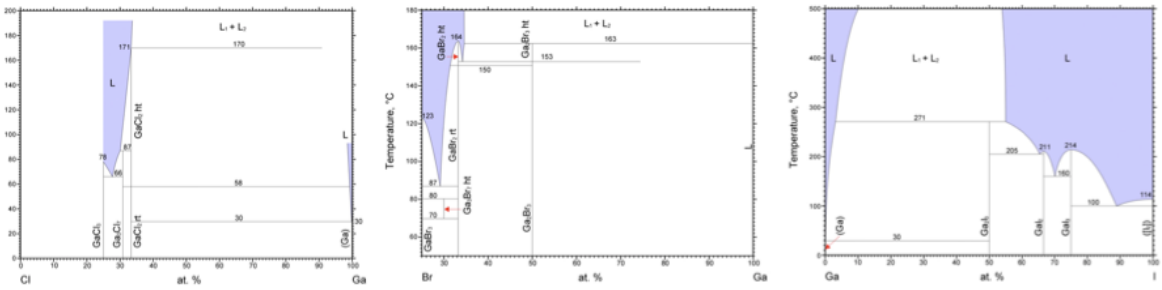

Figure 1.2: Binary Phase Diagrams for Ga/Cl (left), Ga/Br (center) and Ga/I (right). Adapted from ASM International Alloy Phase Diagrams Center.

The GaX_2 products have been dissolved in Lewis-donor solvents such as THF, dioxane, and pyridine. These donor-stabilized gallium (II) species dimerize in solution to form compounds with the molecular formula Ga_2X_4•2L (X = Cl, Br, I and L = THF, dioxane, pyridine).[35]

Worrall's solution method was expanded upon by Green and coworkers in 1990.[81] By directly reacting gallium metal with molecular iodine (rather than gallium triiodide) in toluene and subjecting the reaction mixture to ultrasonic activation, a green powder with the empirical formula GaI was formed. (Equation **1.2**)

$$Ga_{(l)} + I_2 \xrightarrow{sonication\,/\,benzene} {'GaI'}_{(s)} \qquad (1.2)$$

1.2.1.3. Ligand substitution reactions of gallium subhalides.

A number of gallium subhalides have been used as starting materials in the formation of organogallium (II) compounds. Upon reaction with alkylsodium and alkyllithium reagents, Worrall's Ga_2Br_4•2dioxane affords organogallium (II) compounds, which have shown to be stable in the presence of water.[39,53]

Green's 'GaI' product has been employed in the synthesis of a large number of organogallium compounds, and reviews on the subject can be found elsewhere.[82] As representative examples, GaI is capable of oxidatively inserting into iron-iodine bonds as well as carbon-iodine bonds, as reported by Green (see Equation **1.3**).[81] 'GaI' also reacts with the lithium Nacnac reagent [Li{[N(Dipp)C(Me)]$_2$CH}] (Dipp = 2,6-^{i}Pr$_2$-C$_6$H$_3$) to form the monomeric gallium (I) compound [Ga{[N(Dipp)C(Me)]$_2$CH}] (see Equation **1.4**).[28]

$$Cp(CO)_2FeI + GaI \xrightarrow[Et_2O]{} Cp(CO)_2FeGaI_2 \bullet Et_2O \qquad (1.3)$$

$$[Li\{N(Dipp)C(Me)\}_2CH] + {'GaI'} \rightarrow [Ga\{N(Dipp)C(Me)\}_2CH] + LiI \qquad (1.4)$$

1.2.2. Reductive Methods.

1.2.2.1. Aluminum.

The aluminum-aluminum bond was first reported as an 'accessible structural unit in organometallic compounds' by Hoberg and Krause in 1976.[83] Though no crystalline product was obtained, the material obtained upon reduction of diisobutylaluminum chloride with potassium metal in hexane was hypothesized to contain Al-Al bonding based on a number of factors. Presented as evidence were the lack of aluminum metal formation in the reaction mixture, methanolysis studies, and induction of disproportionation upon addition of (and resultant alkyl exchange with) triethylaluminum. While the proposed structure was later determined to be incorrect,[84] the potential of Al-Al bond formation had been demonstrated.

The first structurally characterized compound containing a covalent aluminum-aluminum bond was reported by Uhl in 1988.[9] The tetraalkyldialuminum compound $(Al_2(C(H)TMS_2)_4$ was prepared by reduction of the dialkylchloroaluminum precursor with one equivalent of potassium metal (Equation **1.5**), yielding a crystalline product characterized by X-ray diffraction (for structural details see Section **2.5.1.2.2**). The analogous gallium and indium compounds were reported by Uhl and coworkers shortly thereafter.[39,85]

$$2\ Al(C(H)TMS_2)_2Cl\ +\ 2\ K(s)\ \rightarrow\ Al_2(C(H)TMS_2)_4\ +\ 2\ KCl \qquad (1.5)$$

In 1991 Klinkhammer *et al.* reported the reaction of diisobutylaluminum chloride with potassium metal as producing the anionic $[Al_{12}{}^{i}Bu_{12}]^{2-}$ cluster in moderate yield.[84] This nearly perfect icosahedron is the first aluminum cluster compound reported.

While reductive chemistry has been successfully applied using alkali metals (Na, K, KC_8) to synthesize a handful of aluminum (II) compounds from dialkylaluminum halides (R_2AlX), reduction of monoalkylaluminum dihalides ($RAlX_2$, see Equation **1.6**) has proven to be much more challenging.

$$RAlX_2 + M \rightarrow {}'AlR' + MX \qquad R = alkyl,\ aryl;\ X = Cl,\ Br,\ I;\ M = Na, K \tag{1.6}$$

Cui *et al.* utilized a bulky diaryl Nacnac ligand to prepare the monomeric, donor-free aluminum (I) compound $[Al\{[N(Dipp)C(Me)]_2CH\}]$.[3] By reduction of a diiodide aluminum (III) precursor $Al\{[N(Dipp)C(Me)]_2CH\}I_2$ with potassium metal, $[Al\{[N(Dipp)C(Me)]_2CH\}]$ is prepared in moderate yield. This resulting compound contains an aluminum-based electron lone pair analogous to that of a carbene. Not surprisingly the aluminum (I) atom reacts similarly to carbenes, undergoing [2 + 2] cycloaddition reactions with alkynes, inserting into organic azides, and oxidatively adding oxygen.[86-89] Worth noting in all of these reactions is the tendency of the aluminum (I) center in the precursor compound to oxidatively react, yielding aluminum (III) products.

Similarly, pentamethylcyclopentadienyl (Cp*) aluminum dichloride can be reduced by potassium metal to produce the tetrameric compound $Al_4Cp^*_4$. This compound undergoes oxidative reactions with Group 15 (P) and Group 16 (E = Se, Te) main-group elements to form cage-like $[(Cp^*Al)_6P_4]$ and regular heterocubane $[(Cp^*Al)_4E_4]$ structures.[90,91] In solution the tetrameric compound is in equilibrium with its monomeric AlCp* form, which reacts as an electron pair donor analogous to CO. It

has been shown that AlCp* can donate its lone pair to low-valent transition metals, forming complexes including $[Cr(CO)_5AlCp^*]$ and $[Co_2(CO)_6(\mu_2\text{-}AlCp^*)_2]$.[30,92]

Terphenyl ligands have been shown to stabilize low-valent transition metal and main-group elements and promote metal-metal multiple bonding.[93] Reduction of $Ar'AlI_2$ ($Ar' = C_6H_3\text{-}2,6\text{-}(C_6H_3\text{-}2,6\text{-}iPr_2)_2$) with excess sodium metal afforded the triply-bonded dialuminyne compound $Na_2[Ar'AlAlAr']$. Interestingly, the reduction results in an Al-Al triple bond, balanced in charge by the two intramolecularly-bound sodium cations (see Equation **1.7**). The reduction of the less sterically-hindered $Ar''AlI_2$ ($Ar'' = C_6H_3\text{-}2,6\text{-}(C_6H_2\text{-}2,4,6\text{-}Me_3)_2$) with sodium metal results in the three-atom aluminum cluster $Na_2[Ar''Al]_3$. Rather than forming an Al-Al triple bond, three aluminum atoms form a cyclotrialuminene core, surrounded by three Ar'' ligands (see Equation **1.8**).

$$2\ Ar'AlI_2 \xrightarrow{2\ Na} I(Ar')AlAl(Ar')I \xrightarrow{2\ Na} Ar'AlAlAr' \xrightarrow{2\ Na} Na_2[Ar'AlAlAr'] \quad (1.7)$$

$$3\ Ar''AlI_2 \xrightarrow{8\ Na} Na_2[(AlAr'')_3] \quad (1.8)$$

In addition to direct reduction with alkali metals, aluminum (III) compounds such as the ligand-stabilized alane derivates $IPr{:}AlH_3$ (IPr = :C{(DippNCH)$_2$}, Dipp = 2,6-diisopropylphenyl) and $[(Priso)AlH_2]_2$ (Priso = $^{i}Pr_2NC(NDipp)_2$) have been reduced using Jones' dimeric Mg^{I}-Mg^{I} compound.[7] The highly-reducing magnesium complex reacts with both alane derivatives, forming ligand-stabilized dialane compounds $(Dipp{:}AlH_2)_2$ and $(PrisoAlH)_2$. This facile transformation is noteworthy as it presents the first synthesis of an aluminum (II) hydride compound.

While traditional reductive methods have afforded a number of compounds containing Al-Al bonds, the scope of reductive methods is highly limited in large part due to the instability of the +1 and +2 oxidation states of aluminum relative to the 0 and +3 states. Reduction with alkali or alkali earth metals often leads to deposition of metallic aluminum unless performed in the presence of ligands with high steric bulk. It is believed that this bulk kinetically stabilizes the resulting reduced-state Al compounds from thermal decomposition. Though these compounds are quite interesting based solely on their unusual oxidation state, few applications have been found for these two- or three-aluminum atom-containing molecules. The aluminum hydrides introduced by Bonyhady *et al*. are particularly promising, but these systems are relatively novel and have not been further developed.[7]

1.2.2.2. Gallium.

Much of the reduced-state gallium chemistry that has been reported has come via ligand metathesis reactions with gallium subhalides. However, there have been a few compounds that have been produced via reductive pathways, analogous to their aluminum counterparts. Reduction of Ar'$GaCl_2$ (Ar' = C_6H_3-2,6-(C_6H_3-2,6-iPr_2)$_2$) with sodium metal affords the gallyne compound Na_2[Ar'Ga]$_2$ (see Equation **1.9**).[94] Similarly, the reduction of Ar"$GaCl_2$ (Ar" = C_6H_3-2,6-(C_6H_2-2,4,6-Me_3)$_2$) with potassium metal yields the cyclotrigallenide dianon Na_2[Ar"Ga]$_3$.[95] Neutral ligand-stabilized gallium precursors such as L:Ga(Mes)Cl_2 (where L: = :C{(iPr)NCMe}$_2$ and Mes = 2,4,6-$Me_3C_6H_2$) undergo reduction with potassium metal to yield the neutral octahedral Ga_6 cluster [L:$_2$$Mes_4Ga_6$] (Equation **1.10**).[96] It has been demonstrated that it is possible to

synthesize gallium cluster compounds (Ga_n, where n≤6) via reductive methods, but few other examples have been presented.

$$Ar'GaCl_2 \xrightarrow{6\ Na} Na_2[Ar'GaGaAr'] \quad (1.9)$$

$$L:Ga(Mes)Cl_2 \xrightarrow{K\ (excess)} L:_2\ Mes_4Ga_6 \quad (1.10)$$

1.2.3. Oxidative Methods.

Traditional methods for producing reduced-state main group compounds typically involve reduction of a stable precursor. These reactions occur with varying success, as seen in Section **1.2.2**. In theory it should also be possible to produce reduced-state compounds via oxidation of the element or of zero-valent molecular precursors (Equation **1.11**).

$$M^0 \rightarrow M^I + e^- \quad (1.11)$$

1.2.3.1. Aluminum.

To date, no reduced-state aluminum compounds have been prepared by oxidative methods.

1.2.3.2. Gallium.

Gallium (I) halides have been directly prepared via oxidation of gallium metal by utilizing the sonication methods employed by Green[81] and Jutzi, as previously discussed in Section **1.1**.[29] In the presence of ultrasonic activation and $Ag[Al(OC(CF_3)_3)_4]$, gallium metal is oxidized by silver (I) ions, forming $[Ga][Al(OC(CF_3)_3)_4]$ and silver metal (see Equation **1.12**). The product was found to contain $[Ga(toluene)_2]^+$ cations in the solid state. If the reaction is carried out in the presence of a Lewis donor such as triphenylphosphine, $[Ga(PPh_3)_3]^+$ is formed. This method presents a straightforward and

facile method for preparing naked Ga^+ ions in solution. However, this method is currently limited to non-coordinating anions.

$$Ga + Ag[Al(OC(CF_3)_3)_4] \xrightarrow{sonication} Ga[AlOC(CF_3)_3)_4] + Ag \quad (1.12)$$

1.2.4. High Temperature Synthesis of Aluminum and Gallium Monohalides.

1.2.4.1. Synthesis.

The synthesis of binary gallium subhalides has been well-described, but there are no examples of easily accessible aluminum subhalides prepared by traditional methods. It is possible, however, to prepare metastable aluminum and gallium subhalides in a high-temperature metal halide co-condensation reactor.[97]

Aluminum monohalide gases can be generated at high-temperature (approximately 1200 K) and low pressure (ca. 10^{-5} torr) via the reaction of hydrogen halide gas and molten aluminum metal. The interaction between aluminum and HX results in the gas-phase molecule AlX and hydrogen gas (see Equations **1.13** and **1.14**). Under normal conditions this reaction results in only formation of AlX_3 via Equation **1.13**. At high temperature, a secondary reaction proceeds in the gas phase via Equation **1.14** resulting in the formation of primarily AlX with less than 5% of the reacted aluminum atoms forming AlX_3, though this ratio depends on the hydrogen halide used.

$$Al_{(l)} + 3\ HX_{(g)} \xrightarrow{1000\ °C} 3/2\ H_{2\ (g)} + AlX_{3\ (g)} \quad (1.13)$$

$$AlX_{3\ (g)} + 2\ Al_{(l)} \xrightarrow{1000\ °C} 3\ AlX_{(g)} \quad (1.14)$$

The initial studies of these aluminum monohalide systems utilized infrared spectroscopy to observe AlX deposited onto argon matrices. In order to produce further

evidence of the existence of AlX and to produce increased quantities for a preparative scale, the reactor system was modified to co-condense the generated AlX molecules at 77 K in an organic solvent matrix.

It is worth noting the design of the co-condensation reactor, as this instrument is essential in generating AlX molecules. The reactor chamber (**A**) is a stainless steel bell jar with an approximate volume of 30 L (see Figure **1.3**). The outside of the bell jar is cooled to 77 K by filling the outer steel jacket with liquid nitrogen. Inside the bell jar is a resistively-heated furnace (**B**) surrounded by a water-cooled jacket (**C**). The furnace holds open graphite crucibles filled with aluminum metal that allow for the reaction between the incoming HX gas and the aluminum. The HX gas flow is controlled via a needle valve and is monitored by a capacitance manometer.

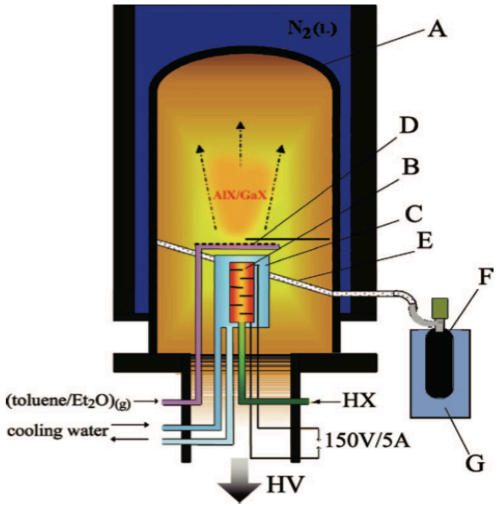

Figure 1.3: Schematic representation of the co-condensation apparatus: A) stainless steel vessel (30 L); B) Al or Ga in the graphite cell with resistive heating; C) cooling shield; D) solvent vapor inlet; E) drainage channel; F) Schlenk flask; G) Dewar with dry ice (-78 °C); HX) hydrogen halide gas; HV) high vacuum. Figure adapted from *Chem. Rev.*, 2010, *110*, 4125–4163.

The co-condensation solvent vapor is introduced via a stainless steel halo (**D**). A diffusion pump (**HV**) is utilized as the evacuation system. Upon completion of the reaction (a typical reactor run involves reaction of HX and Al for 2 hours) the heaters are turned off, the liquid nitrogen is drained, and the chamber back-filled with ultrapure argon. Upon warming the matrix thaws, runs down an internal trough (**E**) and is collected in an externally-connected Schlenk vessel (**F**) cooled to -78 °C in a Dewar (**G**). The resultant reddish-brown solution can be stored for months at -80 °C.[98] The resultant metal-to-halide ratio is inversely proportional to the furnace temperature (i.e. lower temperature yields $AlBr_{1.2}$ while higher temperature will yield $AlBr_{0.9}$).

In addition to use in forming 'AlX' solutions, this method can be exploited to form gallium (I) halides in solution as well. The nature of the species in solution is not known, though the solutions produced by the high-temperature reaction methods are yellow (GaCl) or red-orange (GaBr) compared to the pale-green color of the 'GaI' produced by the method of Green.

1.2.4.2. Further reactions of metastable AlX compounds.

The stability of the generated AlX solutions is highly dependent on the composition of the solvent system. In pure hydrocarbon solvents such as pentane and toluene, the aluminum (I) halide undergoes disproportionation to form aluminum metal and aluminum (III) halide at low temperatures (See Equation **1.15**).[97] However, in a mixed-solvent system containing an aromatic hydrocarbon (toluene or xylene) and a Lewis-donor solvent the solutions are metastable at -78 °C for months. Compatible Lewis donor co-solvents used include diethyl ether, THF, triethylamine, tributylamine and tributylphosphine.

$$AlX \xrightarrow{heat} 2\ Al + AlX_3 \qquad (1.15)$$

The resulting metastable aluminum (I) halide solutions undergo disproportionation reactions and form aluminum metal and aluminum trihalides at temperatures above –78 ºC.[97] In order to stabilize metalloid aluminum clusters (see Section **1.3.1.4**), anionic ligands are added to undergo ligand metathesis reactions. Bulky ligands are known to stabilize low-valent transition metal and main group elements.[93,99] Due to the high reactivity of many aluminum monohalide solutions, these reactions are typically begun at –78 ºC and subsequently allowed to warm. The simplest model for these reactions is a ligand metathesis reaction followed by subsequent disproportionation of 'AlR' compounds (Equation **1.16**). However, evidence for this mechanism is not abundant and it is possible for the reaction to proceed via disproportionation followed by ligand metathesis (Equation **1.17**), or for the processes to occur concurrently.

$$3\ AlCl \bullet Et_2O + 3\ LiR \xrightarrow{-LiCl} 3\ AlR \bullet Et_2O \xrightarrow{heat} 2\ Al + AlR_3 \qquad (1.16)$$

$$3\ AlCl \bullet Et_2O + 3\ LiR \xrightarrow{heat} 2\ Al + AlCl_3 \xrightarrow{LiR} AlR_3 + 3\ LiCl \qquad (1.17)$$

There are multiple variables that contribute to the disproportionation reactions of Group 13 subhalides: the elemental makeup of the subhalide used, the solvent mixture used during co-condensation, the temperature of the co-condensation reaction (and therefore the metal-to-halide ratio), the temperature profile and reactant combination method of the disproportionation reaction, and the crystallization medium all have a significant influence on the resultant chemistry.

As a representative example of ligand metathesis and subsequent cluster formation via disproportionation, reactions of 'AlX' and 'GaX' with lithium hexamethyldisilazide Li[N{$SiMe_3$}$_2$] are highlighted. This ligand is the most extensively studied ligand presented by Schnöckel and coworkers, resulting in numerous crystallographically-characterized products.

1.2.4.2.1. Reactions of 'AlX' with Li[N{$SiMe_3$}$_2$]:

AlCl: To date, three distinct compounds have been reported as formed by the reaction of metastable 'AlCl' and Li[N{$SiMe_3$}$_2$]. Mixing of a xylene/diethyl ether solution of AlCl with solid ligand at -78 °C and subsequent warming to -7 °C gives the $[Al_7R_6]^-$ cluster.[17] By mixing a toluene/diethyl ether solution with solid ligand at -78 °C and quick heating to 60 °C for 2 hours the $[Al_{12}R_8]^-$ cluster is formed at room temperature.[100] By mixing the solution with ligand at -78 °C followed by heating to 60 °C for 1.5 h, filtration, and storage at 60 °C for two months a much larger $[Al_{69}R_{18}]^{3-}$ cluster is formed as red-brown cubes.[26] From these results it can be inferred that the size of the produced cluster is directly related to the temperature of the reaction medium.

AlI: Similarly, the reaction of metastable AlI•Et_2O with Li[N{$SiMe_3$}$_2$] has produced two separate cluster compounds: the $[Al_{14}R_6I_6]^{2-}$ cluster **is** formed at room temperature[101] and the $[Al_{77}R_{20}]^{2-}$ cluster formed at 60 °C.[27] The Al_{77} cluster is the largest reported aluminum cluster compound to date.

1.2.4.2.2. Reactions of 'GaX' with Li[N{$SiMe_3$}$_2$]:

GaCl: Much like aluminum, metastable gallium (I) halides react with Li[N{$SiMe_3$}$_2$] to form metalloid cluster compounds via disproportionation. The reaction of GaCl•Et_2O produces the neutral $Ga_{23}R_{11}$ cluster upon mixing at -78 °C, warming to room

temperature for 24 h then heating to 55 °C for 24 h.[73] There has only been one reported product of this reaction.

GaBr: The reaction of GaBr•THF (toluene:THF 3:1) with Li[N{SiMe$_3$}$_2$] at 55 °C produces the cluster compounds $[Ga_{84}R_{20}]^{4-}$ and $[Ga_{22}R_{10}]^{2-}$ as crystalline products from the reaction solution and subsequent pentane extract, respectively.[71,78] Changing the reaction medium to the less polar toluene:THF 4:1 mixture produces the structurally identical $[Ga_{84}R_{20}]^{3-}$ cluster compound.[102] The reaction mixture was later shown to also form the cluster compound $[Ga_{22}R_{10}Br_{12}]^{2-}$. By warming a mixture of GaBr•THF and Li[N{SiMe$_3$}$_2$] to room temperature, a very similar $[Ga_{22}R_{10}Br_{11}]^{3-}$ cluster is formed.[70]

GaI: No reactions between metastable GaI solutions with Li[N{SiMe$_3$}$_2$] have been reported. However, non-metalloid gallium iodide clusters have been produced by these methods.[57] It is also worth noting that Green's 'GaI' powder can undergo ligand metathesis and subsequent disproportionation to form cluster compounds such as the $Ga_{10}[Si\{^tBu\}_3]_6$ cluster compound.[103]

The resultant air-sensitive products have been predominantly characterized by X-ray crystallography. Many of the crystalline products cannot be redissolved in any solvent mixture without decomposition and thus cannot be studied by NMR spectroscopy.

1.3. Structural Properties of Aluminum and Gallium Compounds

This section will discuss the structural properties of aluminum and gallium compounds in a variety of oxidation states. The majority of this section will focus on reduced-state Al and Ga. A complete table of bond distances with bond errors is presented at the end of this section for reference.

When discussing shell-to-shell bond distances in metalloid aluminum clusters, atoms in the innermost shell will be denoted Al(1), atoms in the second shell Al(2), etc. This convention will also be used to discuss shell-to-shell bonding in both aluminum and gallium – for example, a bond between the innermost shell and second shell in a Ga_n cluster would be denoted as Ga(1)–Ga(2).

1.3.1. Aluminum-containing structures

1.3.1.1. Aluminum (0)

Bulk aluminum metal contains aluminum atoms organized in a face-centered cubic (fcc) lattice (see Figure **1.4**).[104] The atomic radius for aluminum is 1.43(1) Å and the bond length in fcc aluminum metal is 2.86(1) Å. When aluminum metal is exposed to oxygen or water an amorphous aluminum oxide coating forms on the surface, passivating the aluminum metal.[105] These Al_2O_3 layers are typically 25 Å (10-15 Al atoms) thick.

Aside from the bulk metal and its alloys very few Al^0 compounds have been reported in the literature. One particular example is the matrix-isolated aluminum dicarbonyl compound (see Figure **1.4**).[106] Based on *ab initio* calculations, the Al–C distance is found to be 2.05 Å and the C–Al–C angle = 74°.[107]

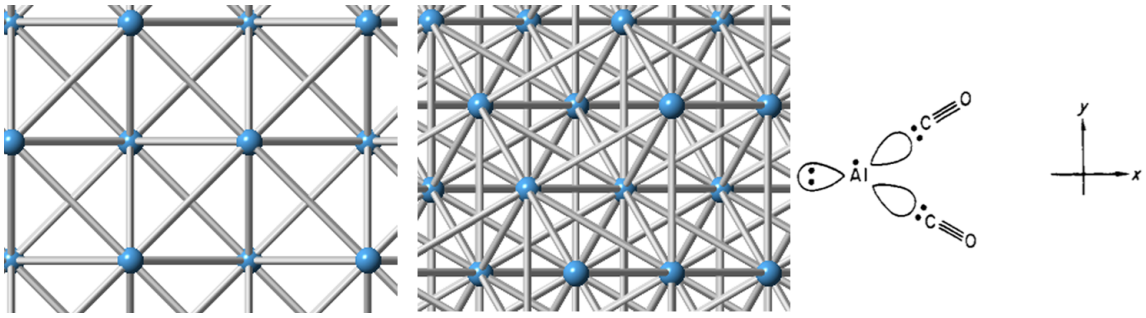

Figure 1.4: X-ray crystal structure of aluminum viewed along the 100 (left) and 110 (center) lattice planes and the calculated structure of $Al(CO)_2$ (right). Image of $Al(CO)_2$ adapted from Chem. Comm. 1972, 338–339.

The 'dialuminyne' $Na_2[Ar'AlAlAr']$ has been prepared via reductive methods (see Section **2.2**) and structurally characterized.[4] The dimeric $Na_2[Ar'AlAlAr']$ (Ar' = C_6H_3-2,6-(C_6H_3-2,6-$^iPr_2$)$_2$) has an Al–Al distance of 2.43(1) Å, a distance far shorter than the other Al–Al bonds reported previously. The C–Al bond distance is 2.04(2) Å. The $[Ar'AlAlAr']^{2-}$ anionic unit is balanced by two closely-bound sodium ions ($d_{Na\text{-}Al}$ = 3.15(1) Å, $d_{Na–C}$ = 2.99(10) Å).

As the term 'dialuminyne' suggests, $Na_2[Ar'AlAlAr']$ contains what is presented as a formal aluminum–aluminum triple bond. However, DFT calculations suggest the bond order in $Na_2[Ar'AlAlAr']$ is actually 1.13 (Wiberg bond order) and that significant non-bonding electron density is present at each aluminum center.

1.3.1.2. Aluminum (I)-containing compounds.

Aluminum (I) ions have two valence electrons available for bonding, allowing for a variety of possible bonding modes. The steric properties of the ligands coordinated to aluminum have a pronounced effect on any potential Al–Al bonding.

1.3.1.2.1. Aluminum (I) compounds containing no Al–Al bonds

The monomeric Al[Nacnac] (Nacnac = $HC(C(Me)NDipp)_2$; Dipp = 2,6-$^{i}Pr_2C_6H_3$)) provides insight into the structural aspects of donor-free aluminum (I). The C_{2v} symmetric structure contains two Al–N bonds between the Al (I) center and the bidentate Nacnac ligand (see Figure **1.5**).[3] The length of the Al–N bonds (d = 1.96(1) Å) is longer than in the related compound Al[Nacnac]Me_2 (d = 1.92(1) Å).[108] Similarly, the N–Al–N bond angles in monomeric Al[Nacnac] are 89.9°, suggesting participation of two orthogonal Al 3p orbitals in covalent bonding to the Nacnac ligand (compared to the 96.1° N–Al–N bond angle in Al[Nacnac]Me_2).

The aluminum atom in Al[Nacnac] is notable for a number of reasons. In contrast to Al[Nacnac]Me_2 the aluminum atom is essentially coplanar with the conjugated N–C–C–C–N plane of the ligand. The aluminum-centered lone pair in Al[Nacnac] is co-planar with the six-membered ring. This lone pair, combined with the steric bulk of the flanking diisopropylphenyl rings of the ligand, strongly contributes to the two-coordinate nature of the aluminum atom. This non-bonding lone pair is isolobal with a silene ($:SiR_2$) and has similar reactivity.[86]

1.3.1.2.2. Aluminum (I) compounds containing Al–Al single bonds

The first compound reported containing aluminum (I) was the tetrahedral $[AlCp^*]_4$ cluster compound.[12] The four aluminum atoms form a regular tetrahedron, with Al-Al bonds measuring 2.77(1) Å. The pentamethylcyclopentadienyl ligands each bind in a η^5 fashion to one of the aluminum atoms, with an Al–$C_{centroid}$ bond distance of 2.01(1) Å. The Al–Al bonds in this compound fall in between the Al–Al bond distances in metallic aluminum (d = 2.86(1) Å) and Uhl's Al^{II} compound ($Al_2(C(H)TMS_2)_4$ (d =

2.66(1) Å, see *Section 1.3.1.3*).[9] The Al–Al–Al bond angles in $[AlCp^*]_4$ are 60.0° (see Figure **1.5**).

In contrast to $[AlCp^*]_4$, a markedly different Al_4 cluster compound is formed by solutions of 'AlBr•NEt_3' formed during a high-temperature co-condensation of AlBr and toluene:triethylamine. The resulting tetrameric $[AlBr•NEt_3]_4$ contains a planar Al_4 ring (Figure **1.5**).[13] The structure of $[AlBr•NEt_3]_4$ exhibits D_{2d} symmetry as a result of the alternating 'up–down–up–down' orientation of the triethylamine ligands. In this compound the Al–Al bonds are 2.64(1) Å, and the Al–Br distances are 2.41(1) Å. This Al–Br distance is much longer than the corresponding terminal Al–Br distance in Al_2Br_6 (2.22(1) Å). The Al–Al–Al bond angles in compound $[AlBr•NEt_3]_4$ are 90.0±0.1°.

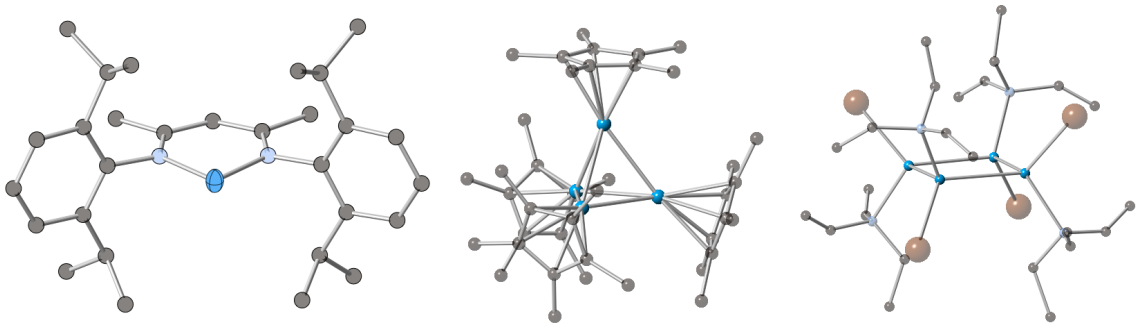

Figure 1.5: X-ray crystal structures of Al[Nacnac] (left), $[AlCp^*]_4$ (center), and $[AlBr•NEt_3]_4$ (right). Blue = aluminum, light blue = nitrogen, black = carbon, brown = bromine. Hydrogen atoms omitted for clarity, thermal ellipsoids (Al in Al[Nacnac]) shown at 50% probability.

1.3.1.2.3: Aluminum (I) compounds containing Al–Al double bonds

No Al–Al double bonds have been isolated to date. There is evidence of Al–Al double bond formation during the reduction of Ar'AlI_2, though the purported dialuminene intermediate undergoes a [2 + 4] cycloaddition with toluene to form the Al (II) dimer $[C_7H_8$(Ar'AlAlAr')] (see Figure **1.6**). The resultant Al–Al single bond in **31** has a distance of 2.58(1) Å and the Al–C bond measures 1.99(1) Å.

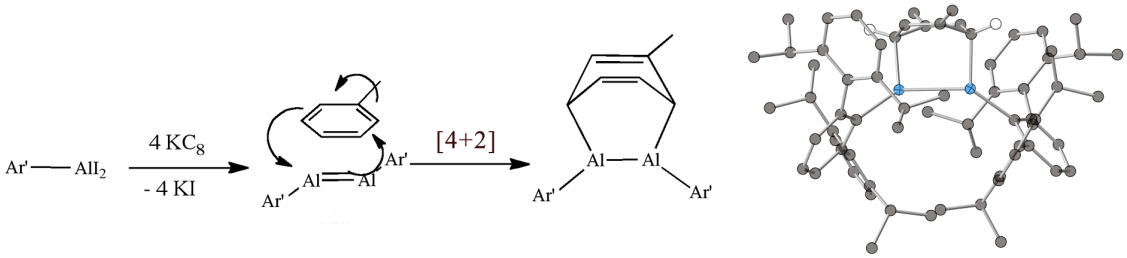

Figure 1.6: Reduction of Ar'AlI_2 and subsequent cycloaddition with toluene to form [C_7H_8(Ar'AlAlAr')] (left) and X-ray crystal structure of [C_7H_8(Ar'AlAlAr')] (right, aluminum = blue, carbon = black, hydrogen = white). Hydrogen atoms except those bound to aluminum-bearing carbons omitted for clarity. Thermal ellipsoids (Al) shown at 50% probability.

1.3.1.2.4. Aluminum (I) compounds containing Al–Al triple bonds.

Aluminum (I) only has two valence electrons and is not capable of forming metal–metal triple bonds.

1.3.1.3. Aluminum (II) containing compounds.

Aluminum (II) contains only one valence electron (electronic configuration $3p^1$), and therefore should only be capable of forming Al–Al single bonds. It has been shown, however, that it is possible to reductively insert an additional electron into Al (II) dimers to form a radical anion.[109]

1.3.1.2.1. Aluminum (II) compounds containing Al–Al single bonds.

The first example of an Al (II) compound is Uhl's [$(TMS_2C\{H\})_2Al]_2$ compound. In this dimeric structure the Al–Al bond is found to be 2.66(1) Å.[9] The four ligands in [$(TMS_2C\{H\})_2Al]_2$ are coplanar, as is the case in the analogous Ga and In compounds.[39,85]

The N-heterocyclic carbene (NHC) stabilized dialane derivative $(IPrH_2Al)_2$ (IPr = :C{$(DippNCH)_2$}, Dipp = 2,6-diisopropylphenyl) contains an Al–Al bond that is 2.64(1) Å in length.[7] In this compound, the aluminum atoms are staggered, and the NHC groups are oriented anti- to each other (see Figure **1.7**). The Al–C bond length of 2.09(1) Å is

slightly longer than the Al–C bond in the precursor IPr•AlH_3 (d_{Al-C} = 2.06(1) Å).[110] The Al–H bonds in [$(IPrH_2Al)_2$ are 1.52(1) Å, compared to 1.53(1) for IPr•AlH_3.

In the related guanidato-substituted dialane $(PrisoAlH)_2$ (Priso = $[(DippN)_2CR]_2R$; R = N^iPr_2, Dipp = 2,6-$^i Pr_2C_6H_3$) the Al–Al bond is 2.68(3) Å.[7] The Al–H bond distances in this compound are 1.53(3) Å. In $(PrisoAlH)_2$ the hydrides occupy anti-staggered positions (see Figure **1.7**). The Al–N bond lengths average 1.95(1) Å, compared to 1.94(1) Å in the guanidato-subsituted alane $PrisoAlH_2$.

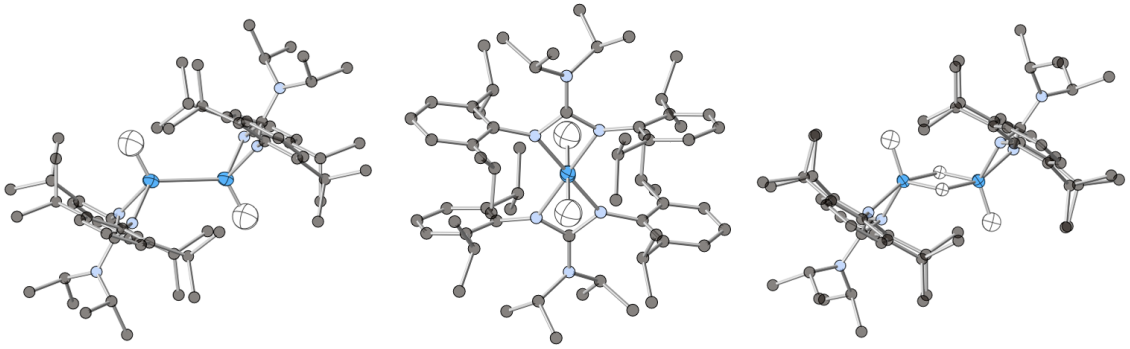

Figure 1.7: X-ray crystal structures of $(PrisoAlH)_2$ (side view: left; view down Al–Al bond axis, center) and $[PrisoAlH_2]_2$ (side view, right). Aluminum = blue, carbon = black, nitrogen = light blue, hydrogen = white. Only hydrogens bonded to aluminum are shown for clarity. Thermal ellipsoids (Al, H) are shown at 50% probability.

An iodo-substituted analog of $(PrisoAlH)_2$, namely $(PrisoAlI)_2$, has also been prepared and reported. The aluminum (III) precursor $PrisoAlI_2$ is monomeric in the solid state and therefore the Al–I bonds of the two iodoaluminum compounds can be compared directly. In $PrisoAlI_2$ the Al–I bond distances average 2.51(1) Å, compared to 2.49(1) Å in $(PrisoAlI)_2$ (a 0.02 Å difference). The Al–N bond distances differ similarly, averaging 1.92(1) Å in $(PrisoAlI)_2$ and 1.87(1) Å in $PrisoAlI_2$ (a 0.05 Å difference). These numbers

suggest that the difference in covalent radius between Al^{II} and Al^{III} is approximately 0.04 Å.

1.3.1.3. Aluminum (III) containing compounds.

Given the lack of electrons capable of forming Al–Al bonds in aluminum (III) species there are no reported Al^{III}–Al^{III} bonds. It is possible, however, to compare the bonding distances in Al(I) and Al(II) species with corresponding Al(III) compounds. For example, the Al–Br bond in $[AlBr•NEt_3]_4$ is 2.41(1) Å.[13] This Al–Br distance is much longer than the corresponding terminal Al–Br distance in Al_2Br_6 (2.22(1) Å). The Al–C bond distances in the dimeric Al_2Me_6 are 1.93(1) (terminal) and 2.15(1) Å (terminal) as determined by neutron diffraction.[111]

1.3.1.4. Metalloid Aluminum Clusters.

Metalloid clusters contain more metal–metal bonds than metal–ligand bonds. In these compounds the oxidation state of aluminum varies but is typically between 0 and 1. These metalloid clusters vary in size, ranging from 7 to 77 atoms for aluminum.[17,27]

1.3.1.4.1. Metalloid Aluminum Clusters Containing One Aluminum Shell.

Clusters are three-dimensional entities, often viewed as models of bulk metal formation. Currently, there have been no examples of metalloid aluminum cluster compounds that contain only one shell of aluminum atoms. It should be noted that in these structures the discussion of bonding interactions are generally limited to those Al–Al distances ranging between 2.5 and 3.0 Å. Especially in the case of the larger multi-shell clusters, there are intra-shell Al–Al distances of upwards of 5.70 Å (in $[Al_{69}(N\{TMS\}_2)_{18}]^{3-}$, *see Section 1.3.1.4.4* for details). While there is no significant

orbital overlap in these outer shells, intra-shell interactions will be presented as bonding in order to better illustrate the spatial orientation of the atoms in these shells.

1.3.1.4.2. Metalloid Aluminum Clusters Containing Two Aluminum Shells. *$Al_{12}[Al_{10}X_{20}D_{10}]$*. The structurally-similar aluminum subhalides $Al_{12}[Al_{10}X_{20}D_{10}]\bullet D_2$ (where X = Cl, and D = THF or THP[23] and X = Br and D = THF[112]) are composed of two aluminum shells. In the solid state the interior icosahedral shell of twelve aluminum atoms is surrounded by ten $[AlX_2\bullet D]$ moieties (see Figure **1.8**). The interior icosahedron is compressed along the axis located between the two aluminum atoms bound to solvent, similar to the $B_{10}C_2$ icosahedron in the *para*-carborane $B_{10}C_2(CCl_2H)_{10} \bullet 2H$ (Figure **1.8**).[113]

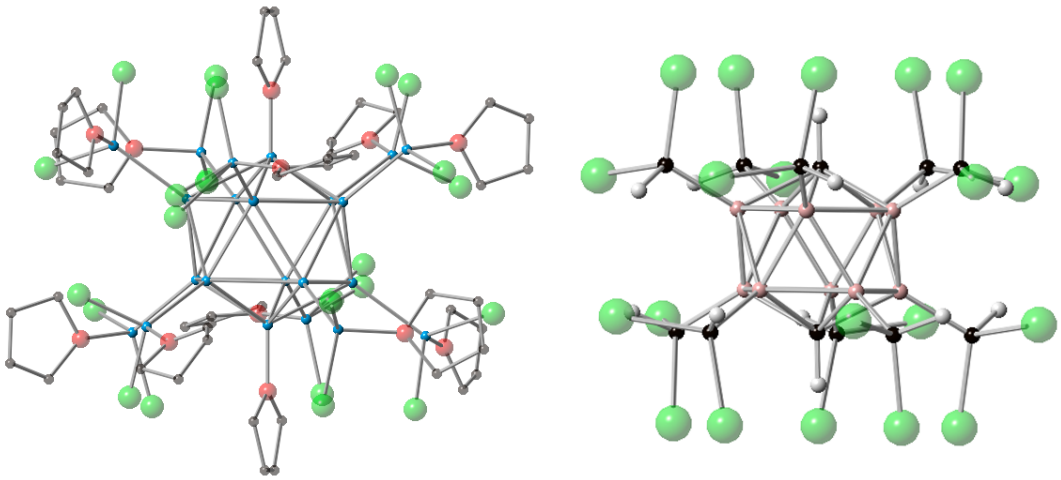

Figure 1.8: X-ray crystal structures of $Al_{12}[Al_{10}Cl_{20}THF_{10}]\bullet THF_2$ (left) and $B_{10}C_2(CCl_2H)_{10} \bullet 2H$ (right). Blue = aluminum, green = chlorine, red = oxygen, pink = boron, white = hydrogen. Hydrogen atoms in 38 omitted for clarity.

The inner Al_{12} shell of $Al_{12}[Al_{10}Cl_{20}THF_{10}]\bullet 2$ THF contains Al(1)–Al(1) bonds averaging 2.71(7) Å. The Al(1)–Al(2) bonds average 2.55(2) Å. The shorter Al(1)–Al(2) bonds can be explained by considering the smaller covalent radius of aluminum (II),

which comprises the outer shell. In $Al_{12}[Al_{10}Cl_{20}THF_{10}]$•2 THF the Al–Cl bond distances are 2.30 Å . In the partially substituted $Al_{20}Cp^*_8X_{10}$ clusters (X = Cl, Br)[114] a similar Al_{12} icosahedron is found in the core shell. The Al(1)–Al(1) distances in $Al_{20}Cp^*_8Cl_{10}$ are 2.68(4) Å, the Al(1)–Al(2) bonds 2.53(3) Å.

$[Al_7[N(TMS)_2]_6]^-$. The seven-atom cluster $[Al_7[N(TMS)_2]_6]^-$ is formed during the reaction of AlCl•Et_2O with $Li[N(TMS)_2]$.[17] The resulting cluster contains one central naked aluminum atom contained inside a distorted aluminum octahedron (see Figure **1.9**). The two $Al_3[N(TMS)_2]_3$ planes in $[Al_7[N(TMS)_2]_6]^-$ are staggered with respect to each other; the central aluminum atom has been described as a model for the atomic contacts in aluminum metal.[17]

It has been noted in passing that other compounds having the general $[Al_7R_6]^-$ structure (R = $N(SiMe_2R')$, R' = hexyl, butyl, isopropyl) have been reported, suggesting that the $[Al_7R_6]^-$ structure is particularly stable in the solid state for aluminum disilazides.[115]

The Al(1)–Al(2) bond distances in $[Al_7[N(TMS)_2]_6]^-$ are 2.74(1) Å, comparable to the Al(1)–Al(1) separations in $[Al_7[N(TMS)_2]_6]^-$. The Al(2)–Al(2) bond distances in the exterior planes are 2.54(1) Å. The Al–N bond distances are 1.84(1) Å, longer than those in $Al[N(TMS)_2]_3$ (Al–N bond distance 1.78(2) Å).[116] The average oxidation state of the entire cluster compound is +0.71. The bond distances are shorter than those in bulk aluminum metal and vary significantly between Al(1)–Al(2) and Al(2)–Al(2) though the layered structure of the Al_7 core superimposes very well over the bulk structure of aluminum metal (see Figure **1.9**).

[Al$_7${N(SiMe$_2$Ph)$_2$}$_6$]. The neutral Al$_7$ cluster compound [Al$_7${N(SiMe$_2$Ph)$_2$}$_6$] is formed during the reaction of AlCl•Et$_2$O with Li[N(SiMe$_2$Ph)$_2$].[18] This cluster is at first glance nearly identical to [Al$_7$[N(TMS)$_2$]$_6$]$^-$, especially the Al$_7$ core (Figure **1.9**). The Al(1)–Al(2) bond distances are 2.73(1) Å in **42**, strikingly similar to the [Al$_7$[N(TMS)$_2$]$_6$]$^-$ (2.74 Å). In [Al$_7${N(SiMe$_2$Ph)$_2$}$_6$] the Al(2)–Al(2) bond distances in the exterior planes are 2.61(1) Å, 0.07 Å longer than the corresponding bonds in [Al$_7$[N(TMS)$_2$]$_6$]$^-$ (2.54(1) Å).

These differences in the Al$_3$ bond distances are the result of the one-electron difference between [Al$_7${N(SiMe$_2$Ph)$_2$}$_6$] and [Al$_7$[N(TMS)$_2$]$_6$]$^-$. It is noted that the greater homogeneity of the Al–Al bond distances in [Al$_7${N(SiMe$_2$Ph)$_2$}$_6$] make it a more accurate model for bulk aluminum bonding than [Al$_7$[N(TMS)$_2$]$_6$]$^-$, though neither compound has a 12-coordinate central aluminum atom (See Figure **1.9**).

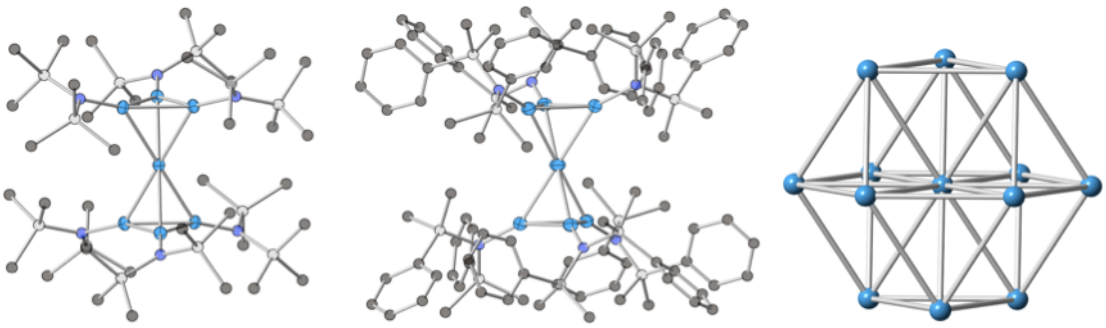

Figure 1.9: X-ray crystal structures of anionic [Al$_7$[N(TMS)$_2$]$_6$]$^-$ (left), neutral radical [Al$_7${N(SiMe$_2$Ph)$_2$}$_6$] (center), and Al$_{13}$ unit in bulk aluminum metal (right). Aluminum = light blue, carbon = black, nitrogen = dark blue, silicon = light gray. Hydrogen atoms omitted for clarity, thermal ellipsoids (Al) shown at 50%

K$_8$Al$_{12}$(O^{t}Bu)$_{18}$. The structure of K$_8$Al$_{12}$(O^{t}Bu)$_{18}$ is noteworthy for a number of reasons. Firstly, it is currently the only reported metalloid aluminum cluster containing oxyanion

ligands.[20] The Al_6 core is a highly-charged distorted octahedron, stabilized by bonding interactions with the outer [$K_8Al_6O^tBu_{18}$] shell (See Figure **1.10**).

The X-ray crystal data for $K_8Al_{12}(O^tBu)_{18}$ is not high quality; the bonding is not reported with high precision but is supported by DFT calculations. The Al_6 core (dark blue) is ordered in the solid state and therefore was used as a reference for the computational data. The Al(1)–Al(1) bond distances in the Al_6 core average 2.67(4) Å and the Al(2)–Al(2) bonds are reported as 2.61(1) Å based on DFT calculations. The ion-paired potassium ions clearly play a role in the stabilization of the cluster, coming in close contact with twelve of the eighteen *tert*-butoxide ligands. As such, it is difficult to assign formal oxidation states to the aluminum atoms in the inner and outer shells — the outer shell could be viewed as either a shell of Lewis-acidic $Al(O^tBu)_3$ moieties or as partially-reduced $Al(O^tBu)•KO^tBu$ units. A more accurate depiction of the bonding in $K_8Al_{12}(O^tBu)_{18}$ likely is a hybrid of these two models. It is worth noting that the Al_6 core in $K_8Al_{12}(O^tBu)_{18}$ is the only reported example of a Zintl-type aluminum core.

1.3.1.4.3. Metalloid Aluminum Clusters Containing Three Aluminum Shells.
$Al_{50}Cp^*_{12}$. The pseudofullerene $Al_{50}Cp^*_{12}$ (perhaps more accurately described as [$Al_8@Al_{30}$•12AlCp*]) is synthesized by reaction of AlBr•THF with $MgCp^*_2$.[24] The Al_{50} cluster contains a naked Al_8 core surrounded by a polyhedral Al_{30} shell. The bond distances in the highly disordered Al_8 core average 2.66(11) Å (blue, Figure **1.11**). The average Al(1)–Al(2) distance is 2.81(20) Å. Within the Al_{30} second shell the Al(2)–Al(2) bonds average 2.76(7) Å (light green, Figure **1.10**).

Twelve AlCp* moieties are located on the pentagonal faces of the Al_{30} shell. The Al_2–Al_3 bond distances are 2.87(10) Å (Al_3 shell depicted in yellow). The Al–$C_{centroid}$

distances average 1.98(1) Å (comparable with the 2.01(1) Å Al–$C_{centroid}$ distance in $[AlCp^*]_4$.[12] As is typical in multi-shell metalloid clusters, the intra-shell bonds in $Al_{50}Cp^*_{12}$ are much shorter than the inter-shell bonds.

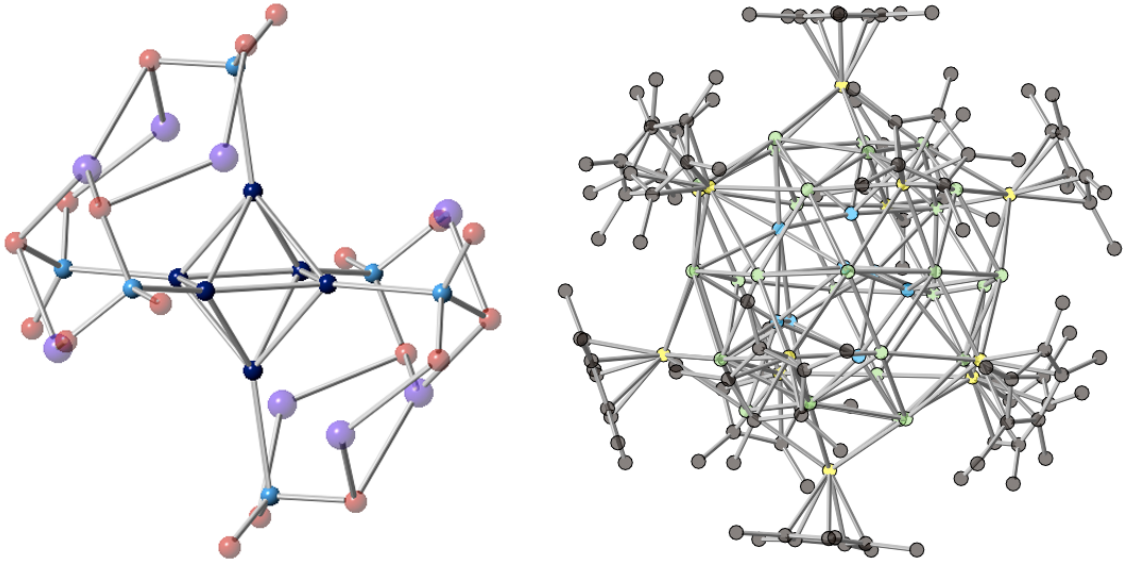

Figure 1.10: X-ray crystal structures of $K_8Al_{12}(O^tBu)_{18}$ (left; dark blue = Al_6 core, light blue = Al_6 periphery, red = O, purple = K. Disordered carbons and hydrogens omitted for clarity) and $Al_{50}Cp^*_{12}$ (right; light blue = disordered Al_8 core, green = Al_{30} second shell, yellow = outer $[AlCp^*]_{12}$ shell. Hydrogens omitted for clarity, thermal ellipsoids (Al) shown at 50% probability).

1.3.1.4.4. Metalloid Aluminum Clusters Containing Four Aluminum Shells. $[Al_{69}(N\{TMS\}_2)_{18}]^{3-}$ and $[Al_{77}(N\{TMS\}_2)_{20}]^{2-}$. To date, the largest metalloid aluminum clusters that have been characterized are the $[Al_{69}(NTMS_2)_{18}]^{2-}$ and $[Al_{77}(NTMS_2)_{20}]^{2-}$ clusters produced by the reaction of $Li[N(TMS)_2]$ and $AlCl{\bullet}Et_2O$ and $AlI{\bullet}Et_2O$ respectively (see Figure **1.11**).[27,117] The overall size of the two clusters is similar. However, there are marked differences in the two structures aside from the obvious differences in the number of atoms and ligands.

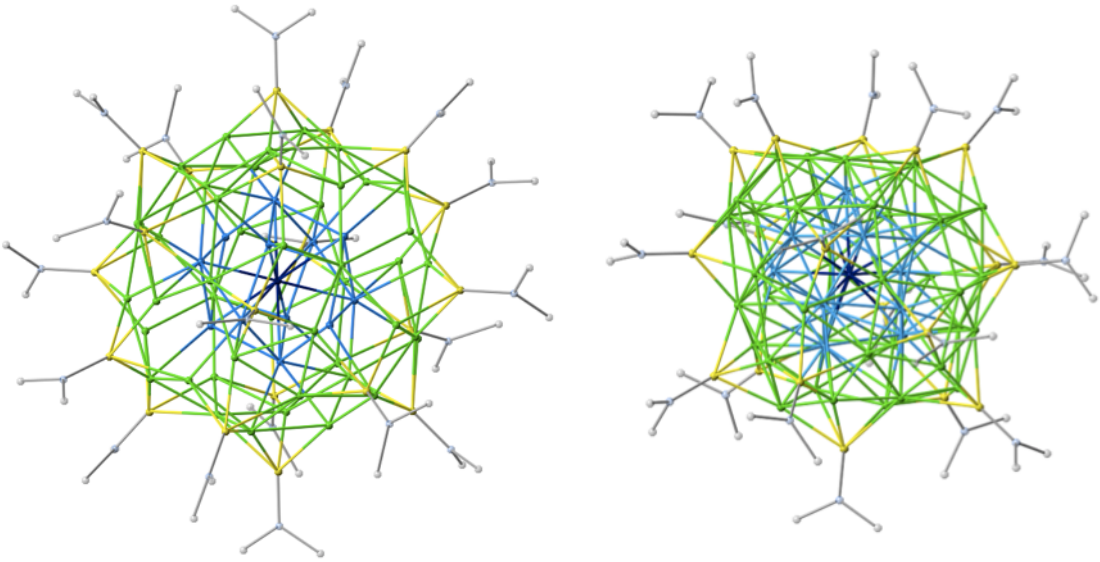

Figure 1.11: Combined-shell view of Al_{77} (left) and Al_{69} (right) clusters. Dark blue = Al(1), blue = Al(2), green = Al(3), yellow = Al(4), light blue = nitrogen, gray = silicon. Methyl groups omitted for clarity.

At the core of both clusters is a single aluminum atom with a coordination number of 12. Moving outward to the second shell the structural differences are immediately noticeable (see Figure **1.12**). In Al_{77} the second shell contains 12 aluminum atoms in a decahedral arrangement with distorted D_{5h} symmetry, and Al(2)–Al(2) bonds averaging 2.78(15) Å; the Al(1)–Al(2) bond distances also average 2.78(10) Å. In Al_{69} the second shell is a 12-atom distorted icosahedron with Al(2)–Al(2) distances averaging 2.80(14) Å; the Al(1)–Al(2) distances average 2.76(10) Å. The structural differences in the second shell have a pronounced effect on the atomic packing in Al_{77} and Al_{69}, reminiscent of the difference between hcp and ccp bonding.

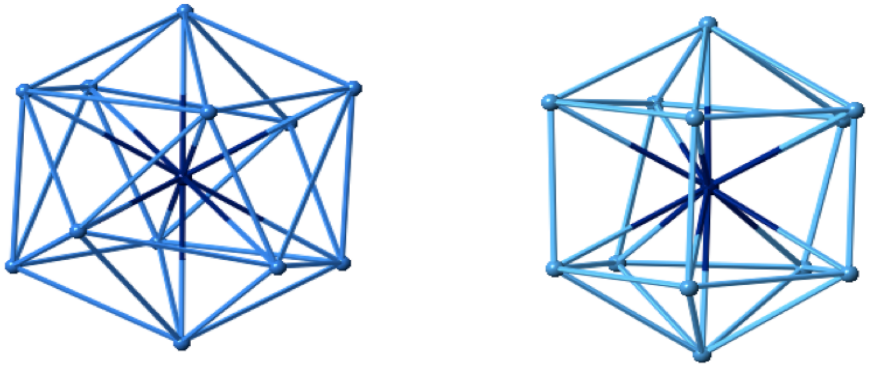

Figure 1.12: First and second shells of Al_{77} (left) and Al_{69} (right). Central Al atom = dark blue, Al_{12} second shell = light blue.

The third shells of Al_{69} and Al_{77} are markedly different (Figure **1.13**). In Al_{69} the third shell contains 38 atoms arranged in an arrangement containing triangular, quadrangular and pentagonal faces. The Al(3)–Al(3) bonding interactions average 2.80(18) Å, ranging from 2.60 to 2.98 Å. In Al_{77} the third shell consists of 44 Al atoms. These atoms are arranged in a shell similar in size to the third shell in Al_{69}. The Al(3)–Al(3) bonding interactions in the third shell of Al_{77} average 2.76(22) Å. The slightly closer packing in Al_{77} is a result of the closer packing required to fit an additional six atoms in a similarly-sized shell.

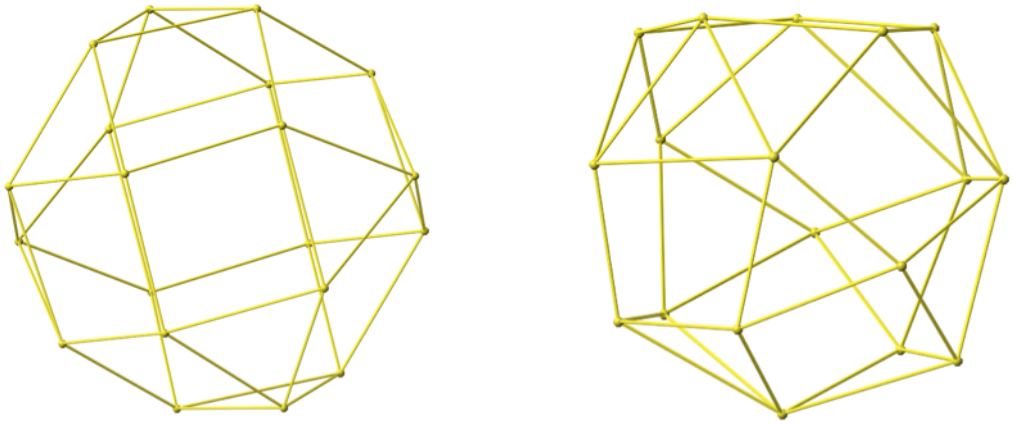

Figure 1.13: Third shells of Al_{77} (left, 44 atoms) and Al_{69} (right, 38 atoms).

The peripheral shells of Al_{69} and Al_{77} consist of 18 and 20 $Al[N(TMS)_2]$ units, respectively (see Figure **1.14**). These moieties have average Al(3)–Al(4) bond distances of 2.68(17) Å in Al_{69} (ranging from 2.54 to 2.88 Å) and 2.69(14) Å in Al_{77} (ranging 2.57-2.85 Å). Moving outward from the core aluminum atom to the periphery the bond distances steadily decrease (see Table **1.2** for details). The Al(4)–N bond distances in both Al_{77} and Al_{69} are 1.83(2) Å.

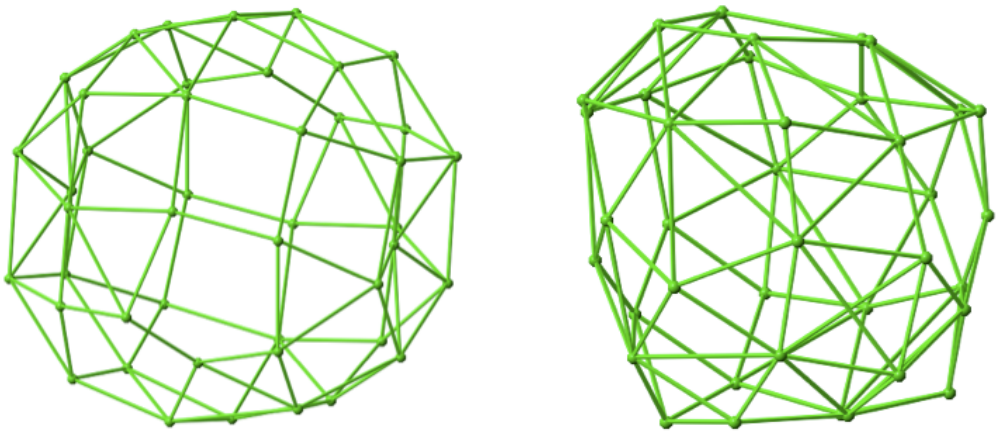

Figure 1.14: Outer Al shells of Al_{77} (20 atoms, left) and Al_{69} (18 atoms, right). Bound $[N(TMS)_2]$ units are omitted for clarity.

The bonding in Al_{77} and Al_{69} show the pronounced structural differences that

result due to small changes in bonding geometry. A slight rotation (~36º) of one Al_5 unit in the Al_{12} second shell with respect to the other results in significantly altered cluster packing. These structural changes are not only manifested in the number of atoms per shell but also in the overall cluster size.

As is shown in Table **1.2**, the shell-to-shell distances in metalloid aluminum clusters decrease towards the periphery. This is due to the core atoms being more metallic in nature – these atoms generally have higher coordination numbers, and lower oxidation states than the ligand-bound atoms at the cluster surface. This trend is similar in metalloid gallium clusters, as will be demonstrated in Section **1.3**.

Table 1.3: Bond distances in non-metalloid Al compounds**.**

Formula	Al–Al	Al–R	Al–D	Ox State	Ref
$NacNacAlMe_2$	—	1.92 (N)	1.96 (C)	3	118
$Al[NTMS_2]_3$	—	1.78(2)	—	3	116
$Al_2[Si[C^tBu_3]_3]_4$	2.75(1)	2.72(1)	–	2	5
Al_2Br_4•2Anisole	2.53(1)	2.30(2)	1.93(1)	2	6
$[AlH_2(NHC)]_2$	2.64(1)	1.54(1)	2.09(1)	2	7
$[AlCp^*]_4$	2.77(1)	2.01(2)	—	1	12
AlNacNac	—	1.96(1)	—	1	3
$[AlBr•Et_3N]_4$	2.64(1)	2.10(1)	2.42(1)	1	13
Na_2[Ar'AlAlAr']	2.43(1)	2.04(2)	3.15(1)	0	4

Table 1.4: Bond distances in selected metalloid aluminum clusters**.**

Formula	Al(1)–Al(1)	Al(1)–Al(2)	Al(2)–Al(2)	Al(2)–Al(3)	Al(3)–Al(3)	Al(3)–Al(4)	Al–R	Al–D	Ref
Al_n	2.86	2.86	2.86	2.86	2.86	2.86	—	—	104
$[Al_7N[TMS_2]_6]^-$	—	2.74(1)	2.54(1)	—	—	—	1.84(1)	—	17
$Al_7N[Me_2SiPh]_6$	—	2.73(1)	2.61(1)	—	—	—	1.81(1)	—	18
$K_8Al_{12}(O^tBu)_{18}$	2.67(4)	2.61(1)	—	—	—	—	*	—	20
$Al_{22}Cl_{20}THF_{10}$	2.70(5)	2.55(2)	—	—	—	—	2.17(2)	1.88(1)	23
$Al_{50}Cp^*_{12}$	2.66(11)	2.81(20)	2.76(7)	2.87(10)	—	—	1.98(1)	—	24
$[Al_{69}[N(TMS_2)]_{18}]^{3-}$	—	2.78(10)	2.78(15)	2.78(15)	2.80(18)	2.68(17)	1.83(2)	—	26
$[Al_{77}[N(TMS_2)]_{18}]^{3-}$	—	2.76(10)	2.80(14)	2.81(17)	2.76(22)	2.69(14)	1.83(2)	—	27

*As the crystal data for the outer shell of **44** is poor, Al–O bond distances are not included.

1.3.2. Gallium-containing structures.

1.3.2.1. Gallium (0).

Gallium metal has a covalent radius of 1.22 Å(1), resulting in a covalent Ga–Ga bond distance of 2.44(1) Å. In its crystal form that is present at standard conditions each gallium atom has one nearest neighbor 2.48(1) Å away and also has six other gallium atoms within 2.79(1) Å.[119] Gallium metal has its own unique crystal structure that is not present in any other metal. The 010 and 100 projections of crystalline gallium can be seen in Figure **1.15**.

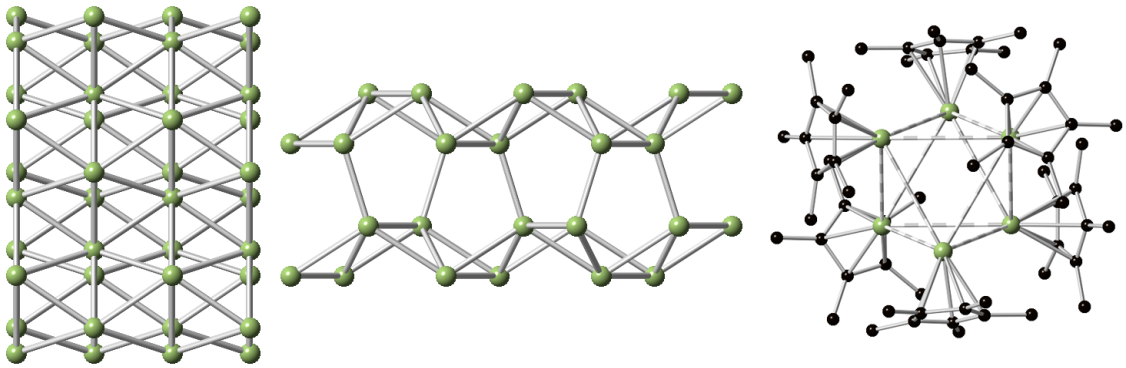

Figure 1.15: Gallium metal along the 010 (*left*) and 100 (center) projections ($d_{Ga–Ga}$ = 2.44–2.83 Å). At right is the loosely associated [GaCp*] hexamer in the solid state ($d_{Ga–Ga}$ = 4.14 Å, $d_{Ga–C}$ = 2.10 Å). Green = gallium, black = carbon. Hydrogen atoms have been omitted for clarity.

The 'digallyne' Na_2[Ar'GaGaAr'] is readily produced via reduction of a digallene precursor.[95] The bonding in Na_2[Ar'GaGaAr'] can be described as containing a formal Ga–Ga triple bond, with pseudo-axial Ar' ligands and two sodium ions (see Figure **1.16**). The Ga–Ga bonding distance in Na_2[Ar'GaGaAr'] is 2.35(1) Å (0.28 Å shorter than the Ga–Ga bond in Ar*Ga), consistent with a higher bond order. The structure of Na_2[Ar'GaGaAr'] is quite similar to the 'dialuminyne' described in Section **1.2.5.1.1**.[4]

1.3.2.2. Gallium (I)-containing structures.

The green 'GaI' reported by Green in 1990 comprises a mixture of gallium subhalides, as determined by Raman spectroscopy.[120] The predominant species is reported to be $[Ga]_2[Ga_2I_6]$, though a number of other species are present. No single crystal X-ray structure has been reported to date.

The GaCp* unit contains η^5 bonding from the Cp* ring to the gallium center. Unlike $[AlCp^*]_4$, GaCp* crystallizes in a hexameric unit $(GaCp^*)_6$. The Ga–$C_{centroid}$ bond distances average 2.10(1) Å. The Ga–Ga separations in $(GaCp^*)_6$ average 4.12(5) Å. This Ga–Ga distance is far longer than typical Ga–Ga bonds and is certainly far longer than the bond distances in gallium metal (2.44-2.83 Å). The crystal structure of $(GaCp^*)_6$ and its hexagonal packing can be seen in Figure **1.15**.

A weak Ga–Ga bonding interaction with more pronounced Ga–Ga bonding character than $(GaCp^*)_6$ has been reported in the solid-state structure of the 'gallene' Ar'GaGaAr' (Ar' = 2,6-$Dipp_2C_6H_3$, Dipp = 2,6-diisopropylphenyl).[121] The Ga–Ga distance of 2.63 Å suggests very weak bonding between the gallium atoms (see Figure **1.16**). The Ga–C bond distance of 2.05 Å is longer than the corresponding Ga–C bond in monomeric gallium (I) terphenyl compounds (e.g. Ar*Ga where Ar* = 2,6-$Trip_2C_6H_3$, Trip = 2,4,6 triisopropylphenyl).[32] In hydrocarbon solution, the UV-Vis spectrum of Ar*Ga is nearly identical with Ar'Ga, suggesting a monomeric state in solution. In solution Ar'Ga is green; in the solid state it forms red blocks. It should be noted that the term 'digallene' only implies the number of electrons present in the gallium species. The long Ga–Ga bond in Ar'Ga does not contain a Ga–Ga double bond and has a bond order less than 1 based on the evidence presented.

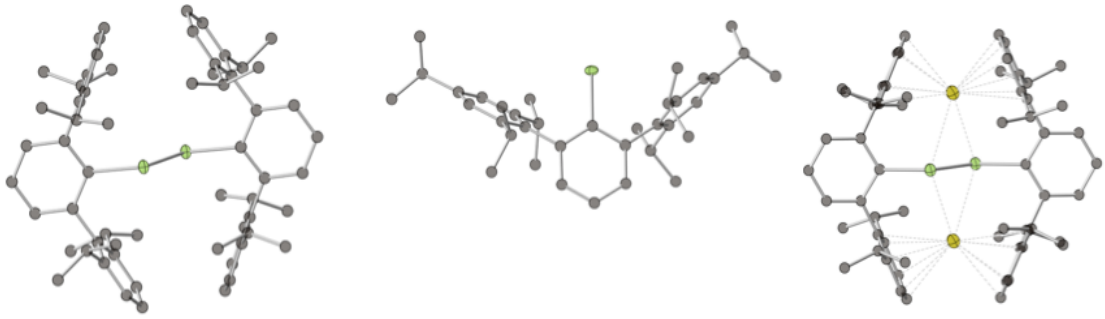

Figure 1.16: X-ray crystal structures of digallane $[Ar'Ga]_2$ (left), monomeric organogallium Ar*Ga (middle), and digallyne $Na_2[Ar'GaGaAr']$. Gallium = green, carbon = translucent black, sodium = yellow. Hydrogen atoms omitted for clarity, thermal ellipsoids shown at 50%.

The $[Ga(C_6H_5F)_{2.5}]^+[Al(OC(CF_3)_3)_4]^-$ and $[Ga(PPh_3)_3]^+[Al(OC(CF_3)_3)_4]^-$ salts and have been characterized and reported by Slattery *et al.*[31] These compounds are noteworthy due to their simple synthesis (see Section **1.2.3.2***)* and for their arene- and phosphene-stabilized Ga^+ ions. The structure of $[Ga(C_6H_5F)_{2.5}]^+[Al(OC(CF_3)_3)_4]^-$ contains both $[Ga(C_6H_5F)_2]^+$ and $[Ga(C_6H_5F)_3]^+$ ions in the solid state. The average Ga–C bond distances in $[Ga(C_6H_5F)_2]^+$ are 3.00(9) Å, compared to 3.17(9) Å in $[Ga(C_6H_5F)_3]^+$. In $[Ga(C_6H_5F)_3]^+$ the Ga–C bonds are longer due to the higher coordination at gallium. The homoleptic gallium phosphine compound $[Ga(PPh_3)_3]^+[Al(OC(CF_3)_3)_4]^-$ contains Ga–P bonds that average 2.39(3) Å (See Figure **1.17**).

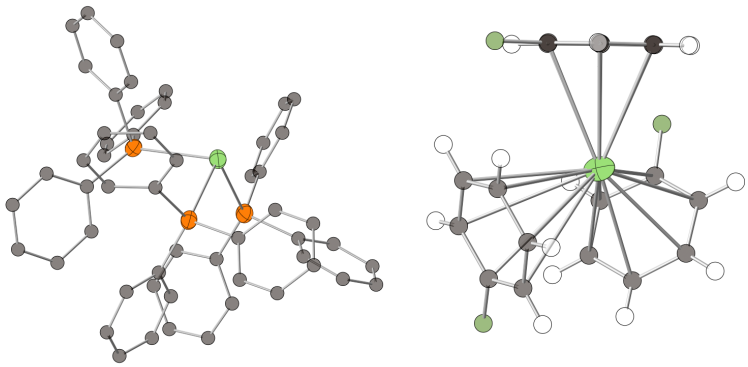

Figure 1.17: X-ray crystal structures of the $[Ga(PPh_3)_3]^+$ and $[Ga(C_6H_5F)_3]^+$ ions. Gallium = light green, Carbon = black, Fluorine = green, Phosphorous = orange. Hydrogen atoms in $[Ga(PPh_3)_3]^+$ omitted for clarity, thermal ellipsoids displayed at 50% probability.

1.3.2.3. Gallium (II)-containing structures

Worrall's X-ray work elucidating the structure of [Ga_2Cl_4 • 2 dioxane] has proven to be quite seminal, providing the first example of a neutral molecule containing a Ga–Ga bond.[122] The Ga–Ga bond distance in [Ga_2Cl_4 • 2 dioxane] is 2.41(3) Å (see Figure **1.18**). The gallium atoms adopt a nearly eclipsed conformation, with the O–Ga–Ga–O dihedral angle measuring 95.9.±0.1°. This eclipsed conformation is notable when contrasted with the reported staggered conformation in $[Ga_2Cl_6]^{2-}$ ion.[123] The Ga–Ga bonding distance in $[Ga_2Cl_6]^{2-}$ is 2.39(1) Å, in close agreement with the Ga–Ga bond in [Ga_2Cl_4 • 2 dioxane].

Structures of bromide analogs [Ga_2Br_4 • 2 dioxane] and [Ga_2Br_4 • 2 pyridine] (see Figure **1.18**) were subsequently reported by Worrall and coworkers.[35] The structure of [Ga_2Br_4 • 2 dioxane] is very similar to [Ga_2Cl_4 • 2 dioxane], containing a Ga–Ga bond distance of 2.40(3) Å and an O–Ga–Ga–O dihedral angle of 96.1±0.1°. Like in [Ga_2Cl_4 • 2 dioxane], the gallium atoms adopt an eclipsed conformation. The Ga_2Br_4 pyridine adduct adopts a staggered conformation, with the pyridine moieties occupying anti positions. The Ga–Ga bond distance is 2.42(6) Å.

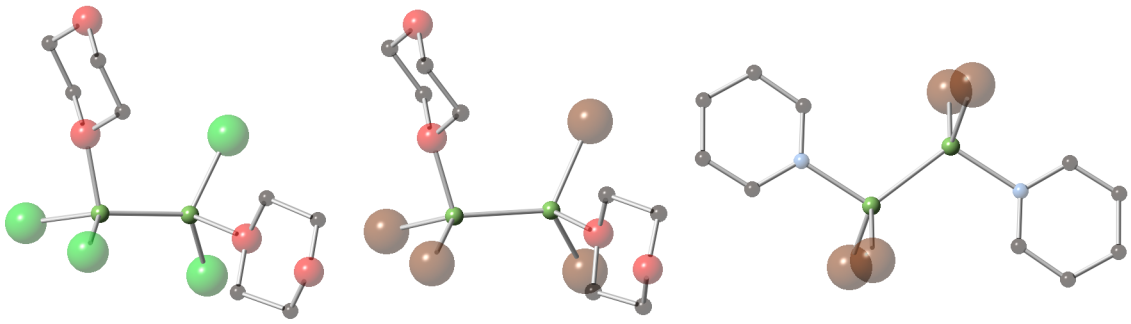

Figure 1.18: X-ray crystal structures of [Ga_2Cl_4 • 2 dioxane] (left), [Ga_2Br_4 • 2 dioxane] (center), and [Ga_2Br_4 • 2 pyridine] (right). Light green = gallium, green = chlorine, brown = bromine, black = carbon, red = oxygen, blue = nitrogen.

The Ga–Ga bonding distance in [Ga_2Br_4 • 2 pyridine] is slightly shorter than those in Ga_2R_4 (R = $C(H)TMS_2$, TMS = trimethylsilyl) compound.[39] In the latter digallane the

Ga–Ga bond distance is 2.54(1) Å, with all four of the alkyl groups residing in the same plane (see Figure **1.19**). Addition of an electron into the system via reaction with ethyllithium results in a shortening of the Ga–Ga bond to 2.40(1) Å in the $[Ga_2R_4]^{\bullet-}$ radical anion.[124]

Surprisingly, the Ga–Ga bonds in $Ga_2(C(H)TMS_2)_4$ are retained upon reaction with water.[53] Rather than oxidative cleavage of the Ga–Ga bond, an acid–base reaction between water and the $C(H)TMS_2$ ligands occurs. The D_{3h}-symmetric product $[Ga_2(C(H)TMS_2)_2(OH)_2]_3$ is thereby formed, undergoing protonolysis of two syn- Ga–C bonds and subsequent trimerization, forming the trimeric product (see Figure **1.19**). The three Ga–Ga bonds in $[Ga_2(C(H)TMS_2)_2(OH)_2]_3$ average 2.44(1) Å.

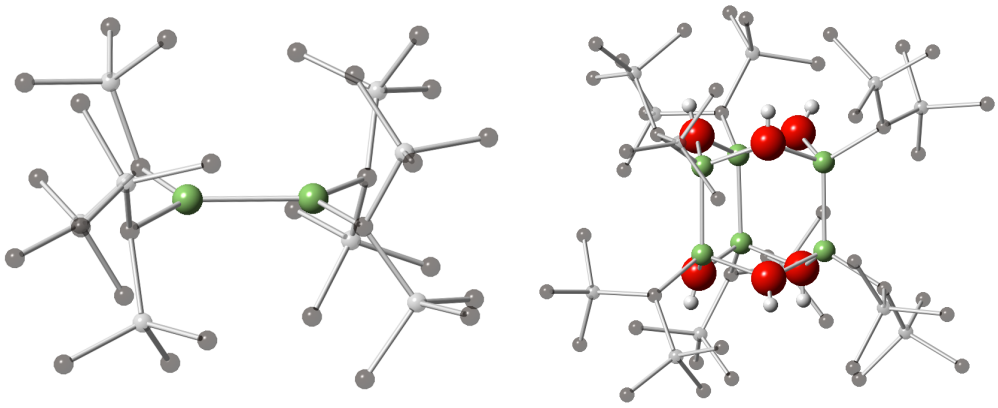

Figure 1.19: X-ray crystal structures of $Ga_2(C(H)TMS_2)_4$ (left) and $[Ga_2(C(H)TMS_2)_2(OH)_2]_3$ (right). Light green = Ga, black = C, gray = Si, red = O, white = H. Hydrogen atoms not attached to oxygen omitted for clarity.

In general, gallium (II) halides seem to be stabilized by Lewis donors. The amine- and phosphine-stabilized Ga_2I_4•2 $EHCy_2$ (E = N (56a) or P (56b)) have been shown to be quite stable in solution and in the solid-state.[34] The Ga–Ga bond in 56a is 2.45(1) Å, identical to the Ga–Ga bond in 56b (d = 2.45(1) Å). The substituent atoms in both 56a and 56b are in the staggered conformations. Ga_2Br_4•2 $PHCy_2$ 57 has been prepared from GaBr•THF and $PHCy_2$ and contains a Ga–Ga bond distance of 2.44(1) Å.[125]

1.3.2.4. Gallium (III)-containing structures.

Like aluminum, gallium (III) halides are dimeric in the solid state. The terminal Ga–Cl bond in Ga_2Cl_6 is 2.06 Å.[126] In $Ga(NTMS_2)_3$ the Ga–N bond distances average 1.91(10) Å.[127] Gallium (III) has an ionic radius of 0.62 Å.[128] Numerous other examples of Ga^{III} compounds are present in the literature.

1.3.2.5. Structural characteristics of metalloid gallium clusters.

The formation of metalloid gallium clusters has provided insight into the structural stability of Ga–Ga bonding. The structural variety of gallium metalloid clusters formed is quite astonishing, especially considering the similarity in cluster size for many of the reported compounds. This section will discuss a number of representative metalloid gallium clusters, with the aim of discussing the structural variety of compounds reported. As was the convention with metalloid aluminum clusters, the longest Ga–Ga bonding interaction to be discussed as a bond is 3.0 Å.

As was the convention in Section **1.3.1**, intrashell and shell-to-shell bond distances will be discussed as Ga(1)–Ga(1) or Ga(1)–Ga(2). A table of selected bond distances of the clusters discussed is attached at the end of this section.

1.3.2.5.1. Single-shell metalloid gallium clusters.

$K_2[Ar^*Ga]_2Ga_2$. The planar four-atom cluster $K_2[Ar^*Ga]_2Ga_2$ (Ar*= 2,6-$Trip_2C_6H_3$, Trip = 2,4,6-$iPr_3C_6H_2$) is formed upon reduction of Ar^*GaCl_2.[33] This tetragallane cluster contains a square Ga_4 core with Ga–Ga bond distances of 2.47(1) Å (see Figure **1.20**). The Ga_4 cluster is coordinated by two Ar* units with Ga–C distances of 2.01(1) Å. Two potassium ions reside above and below the plane of the Ga_4 cluster, with Ga–K bonds averaging 3.43(18) Å and K–C distances averaging 3.57(39) Å. The potassium ions in

$K_2[Ar^*Ga]_2Ga_2$ have a significant stabilizing effect on the $[Ga_4R_2]^{2-}$ core; the corresponding lithium- and sodium-containing compounds were not successfully characterized.

$[Ga_{12}(fluorenyl)_{10}]^{2-}$. The $[Ga_{12}(fluorenyl)_{10}]^{2-}$ ion (fluorenyl = $C_{13}H_9$) is formed from the reaction of fluorenyllithium with GaBr•THF.[65] The central Ga_{12} icosahedron is slightly elongated as a result of the lower coordination at the two non-ligated gallium atoms (see Figure **1.20**). The Ga–Ga bonds in $[Ga_{12}(fluorenyl)_{10}]^{2-}$ average 2.64(11) Å. The ten fluorenyl ligand moieties are coordinated in an η^1 fashion, with an average Ga–C bond distance of 2.06(3) Å.

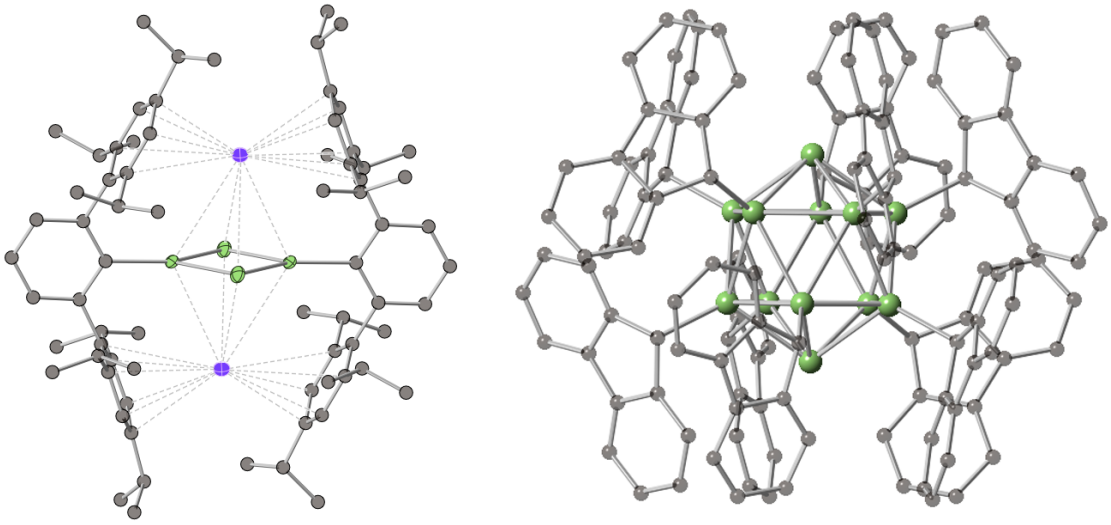

Figure 1.20: X-ray crystal structures of $K_2[Ar^*Ga]_2Ga_2$ (left) and $[Ga_{12}(fluorenyl)_{10}]^{2-}$ (right). Light green = gallium, black = carbon, purple = potassium. Thermal ellipsoids in $K_2[Ar^*Ga]_2Ga_2$ shown at 50% probability, hydrogen atoms omitted for clarity.

1.3.2.5.2. Two-shell metalloid gallium clusters.

$Ga_{22}[P^tBu_2]_{12}$. The neutral D_{2d}-symmetric cluster $Ga_{22}[P^tBu_2]_{12}$ comprises two shells of gallium atoms.[69] The central shell is a distorted Ga_{12} icosahedron (see Figure **1.21**) with Ga(1)–Ga(1) bonds averaging 2.68(15) Å. Within the icosahedron six gallium atoms are

externally bound to gallium atoms of the second shell and six are bound to bridging phosphorous atoms. The outer shell contains two V-shaped Ga_5 units that sit on opposite faces of the central icosahedron. The twelve Ga(1)–Ga(2) bond distances average 2.76(7) Å. The Ga(2)–Ga(2) bond distances average 2.48(3) Å. The Ga–$P_{terminal}$ bond distances average 2.38(5) Å, the Ga–P_{bridge} distances 2.45(5) Å.

$[Ga_{12}Br_2(GaBrN[TMS]_2)_{10}]^{2-}$. The disproportionation and partial bromide exchange of GaBr•THF in the presence of $Li[N(TMS)_2]$ produces $[Ga_{12}Br_2(GaBrN[TMS]_2)_{10}]^{2-}$ ions.[70] This dianion is similar in structure to the $Al_{22}Br_{20}$•12 THF clusters discussed in Section **1.3.1.4.2**.[112] The central Ga_{12} icosahedron in $[Ga_{12}Br_2(GaBrN[TMS]_2)_{10}]^{2-}$ is fully ligated, surrounded by ten $[GaBrN(TMS)_2]$ units and two bromide ions(see Figure **1.21**). The Ga(1)–Ga(1) distances in the core average 2.53(1) Å. These bonds are 0.11 Å shorter than those in the icosahedral Ga_{12} cluster $[Ga_{12}(fluorenyl)_{10}]^{2-}$. The gallium in $[Ga_{12}Br_2(GaBrN[TMS]_2)_{10}]^{2-}$ is slightly more oxidized (average oxidation state = +0.91) than $[Ga_{12}(fluorenyl)_{10}]^{2-}$ (average = +0.67), resulting in a smaller covalent radius and shorter Ga–Ga bonds. The Ga(1)–Ga(2) bonds in $[Ga_{12}Br_2(GaBrN[TMS]_2)_{10}]^{2-}$ are 2.40(1) Å. The ten $N(TMS)_2$ ligands reside are cofacial, with Ga(2)–N bond distances averaging 1.86(2) Å. Ten bromide ligands form a belt connecting the ten Ga(2) atoms. All ten Br atoms in this 'belt' bridge the outer gallium atoms. The remaining two bromide atoms occupy two gallium atoms in the core not bound to external gallium atoms (Figure **1.21**). The Ga–Br bonds in $[Ga_{12}Br_2(GaBrN[TMS]_2)_{10}]^{2-}$ average 2.40(11) Å.[70]

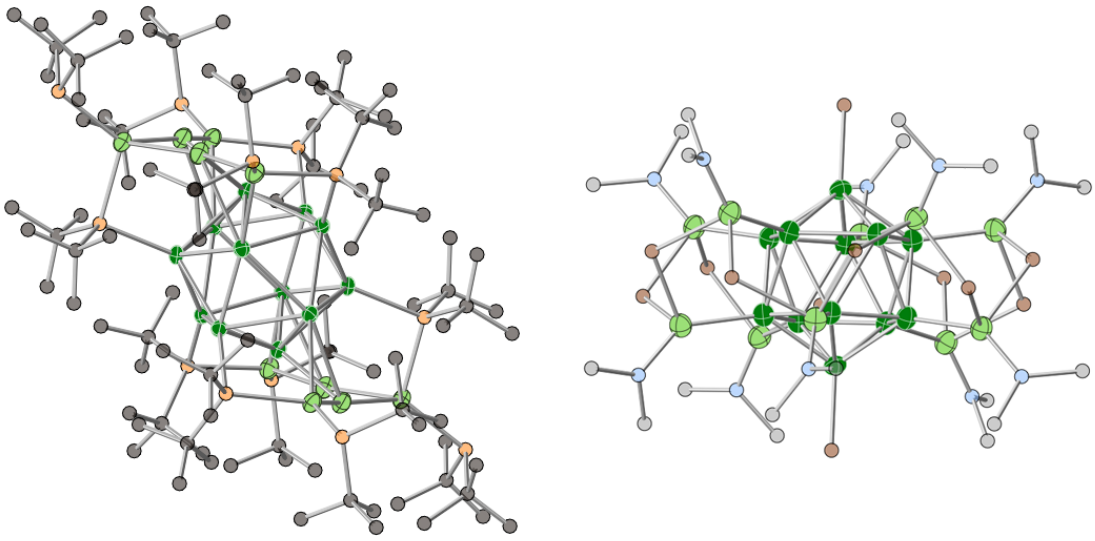

Figure 1.21: X-ray crystal structures of $Ga_{22}[P^tBu_2]_{12}$ (left) and $[Ga_{12}Br_2(GaBrN[TMS]_2)_{10}]^{2-}$ (right). Dark green = Ga(1), light green = Ga(2), orange = phosphorous, black = carbon, light blue = nitrogen, grey = silicon, brown = bromine. Thermal ellipsoids shown at 50% probability, hydrogen atoms in $Ga_{22}[P^tBu_2]_{12}$ and carbon + hydrogen atoms in $[Ga_{12}Br_2(GaBrN[TMS]_2)_{10}]^{2-}$ omitted for clarity.

1.3.2.5.3. Three-shell metalloid gallium clusters.

$[Ga_{19}(C\{TMS\}_3)_6]^-$. The anionic Ga_{19} cluster $[Ga_{19}(C\{TMS\}_3)_6]^-$ (R = $C(TMS)_3$) is produced during the reaction of GaBr•THF with $LiC(TMS)_3$.[68] The structure of $[Ga_{19}(C\{TMS\}_3)_6]^-$ is D_{3d} symmetric comprising three stacked Ga_6 rings (see Figure **1.22**). At the center is a central 12-coordinate gallium atom with distorted hexagonal closest-packed coordination (it should be noted that no stable hcp elemental modification of gallium has been reported).[68] The average Ga_1–Ga_2 bond distances are 2.84(11) Å. The 12-atom second shell in $[Ga_{19}(C\{TMS\}_3)_6]^-$ contains a slightly distorted chair Ga_6 ring surrounding the central Ga atom and six Ga atoms above and below the plane of the Ga_6 ring. The Ga_2–Ga_2 bond distances average 2.71(7) Å. The third shell contains six four-coordinate Ga atoms, each bound to three Ga atoms in shell 2 and one ligand moiety. The average Ga_2–Ga_3 bond distance is 2.50(5) Å, and the Ga_3–C bonds are 2.01(1) Å.

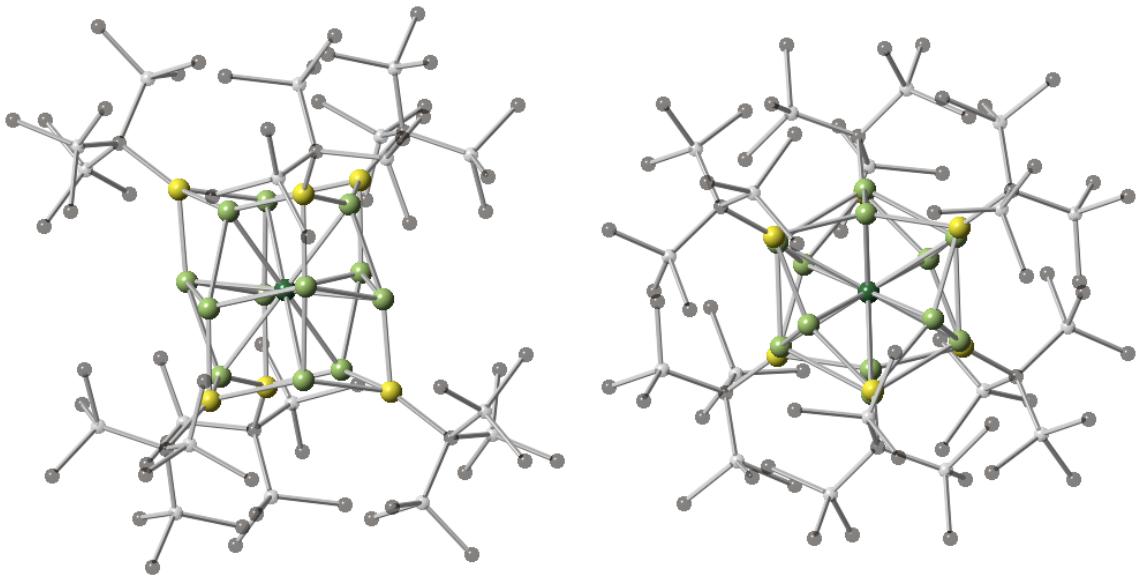

Figure 1.22: X-ray crystal structure of $[Ga_{19}(C\{TMS\}_3)_6]^-$ viewed along the C_2 (left) and C_3 (right) axes. Dark green = center Ga atom, light green = Ga_{12} second shell, yellow = $[Ga(CTMS_3)]_6$ outer shell, black = carbon, grey = silicon. Hydrogen atoms omitted for clarity.

1.3.2.5.4. Four-shell metalloid gallium clusters.

$[Ga_{51}(P^tBu_2)_{14}Br_6]^{3-}$. The *$D_{2d}$*-symmetric metalloid gallium cluster $[Ga_{51}(P^tBu_2)_{14}Br_6]^{3-}$ has been prepared via partial substitution of a GaBr•THF solution with LiP^tBu_2.[77] The core Ga atom (blue, see Figure **1.23**) is surrounded by twelve gallium atoms (dark green) in an hcp arrangement similar to the arrangement in the $[Ga_{19}R_6]^-$ cluster (R = $C(TMS)_3$).[68] The Ga(1)–Ga(2) bond distances in $[Ga_{51}(P^tBu_2)_{14}Br_6]^{3-}$ average 2.84(8) Å. Within the distorted hexagonal-closest-packed second shell the Ga(2)–Ga(2) distances average 2.82(8) Å.

The third layer (light green, Figure **1.23**) of $[Ga_{51}(P^tBu_2)_{14}Br_6]^{3-}$ comprises six square Ga_4 rings. These Ga_4 units sit staggered on the square faces of the Ga_{12} second shell. The average Ga(2)–Ga(3) distances are 2.68(10) Å. The Ga(3)–Ga(3) bonds are 2.77(18) Å. The outer shell of Ga atoms in $[Ga_{51}(P^tBu_2)_{14}Br_6]^{3-}$ contains both the capping $Ga(P^tBu_2)$ units which form six square pyramidal subunits and bridging GaBr units which

span the Ga(3) subunits. The Ga(3)–Ga(4) bonding interactions average 2.56(11) Å, consistent with the partial oxidation of the outer shell. The average Ga–P bond in $[Ga_{51}(P^tBu_2)_{14}Br_6]^{3-}$ measures 2.37(4) Å, and the average Ga–Br bond distance 2.43(1) Å.

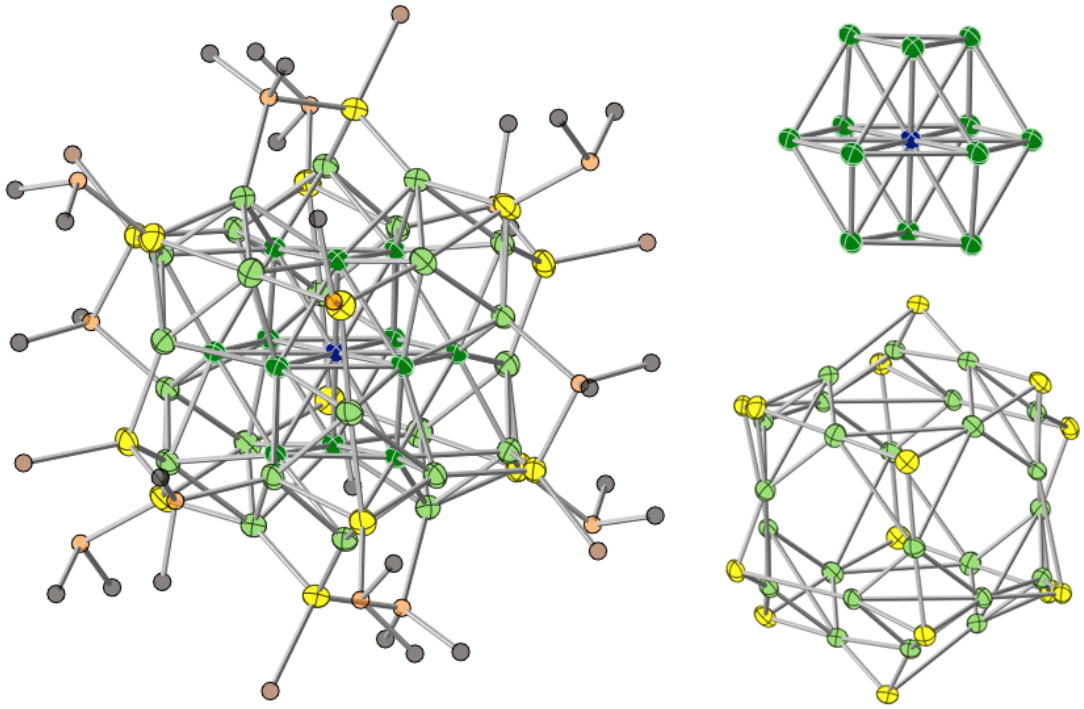

Figure 1.23: X-ray crystal structure of $[Ga_{51}(P^tBu_2)_{14}Br_6]^{3-}$, viewed as a whole molecule (left), Ga(1)–Ga(2) shells (top right), and Ga(3)–Ga(4) shells (bottom right). Dark blue = central Ga(1), dark green = Ga(2), light green = Ga(3), Yellow = Ga(4), orange = phosphorous, black = carbon. Thermal ellipsoids shown at 50% probability, methyl groups omitted for clarity.

$[Ga_{84}(N\{TMS\}_2)_{20}]^{4-}$ and $[Ga_{84}(N\{TMS\}_2)_{20}]^{3-}$. The largest reported gallium metalloid clusters are the $[Ga_{84}(N\{TMS\}_2)_{20}]^{n-}$ compounds (where n = 4 and 3, respectively).[78,102] The two compounds are structurally identical aside from the crystal packing due to the difference in overall charge. For brevity both ions will be discussed as one compound. Disregarding the highly-disordered Ga_2 core the overall symmetry of the anionic portions of $[Ga_{84}(N\{TMS\}_2)_{20}]^{n-}$ is distorted D_{5d} (see Figure **1.24**).

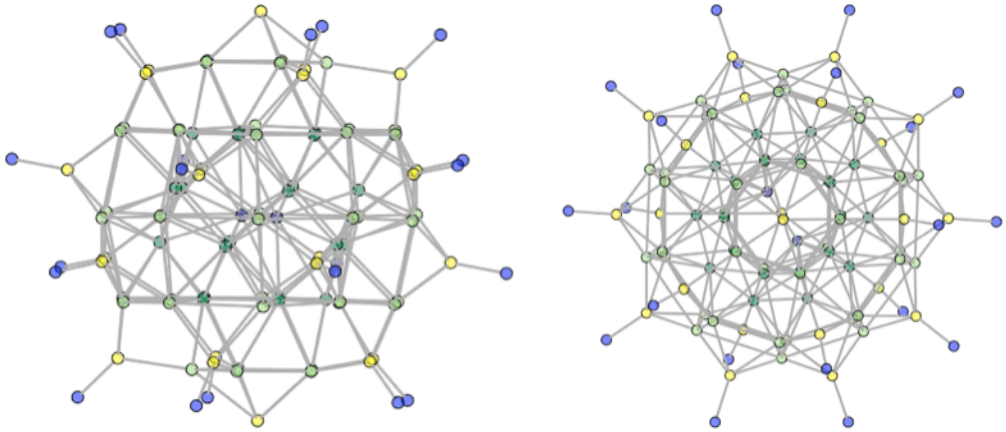

Figure 1.24: X-ray crystal structure of $[Ga_{84}]^{n-}$ ionic cluster compound $[Ga_{84}(N\{TMS\}_2)_{20}]^{n-}$. Methyl groups and silicon atoms omitted for clarity.

At the core of $[Ga_{84}(N\{TMS\}_2)_{20}]^{n-}$ is a highly disordered Ga_2 unit with a Ga(1)–Ga(1) bonding distance of 2.25(2) Å (dark blue, Figure **1.25**). Surrounding the Ga_2 core is a Ga_{20} unit comprised of alternating staggered Ga_5 pentagons (dark green). The average Ga(1)–Ga(2) bond is 2.99(30) Å. The Ga_{20} unit is approximately spherical in shape, with an average Ga(2)–Ga(2) bond length 2.83(5) Å.

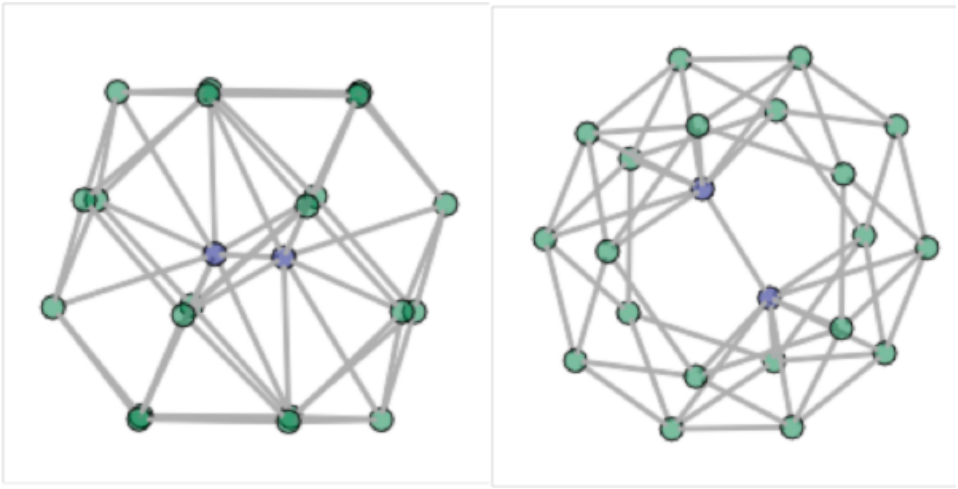

Figure 1.25: X-ray crystal structure of the inner two shells of Ga_{84} cluster. Side view along C_2 axis (left) and top view down C_5 axis (right) are shown. Blue = core Ga_2 unit, dark green = Ga_{20} second shell.

The third Ga shell in $[Ga_{84}(N\{TMS\}_2)_{20}]^{n-}$ contains 40 gallium atoms (light green, Figure **1.26**). Three 'belts' of ten gallium atoms run parallel around the circumference of the cluster, having average intra-belt distances of 3.15(35) Å and inter-belt distances of 2.95(5) Å. Two planar Ga_5 pentagons sit above and below the outer belts, having average intra-ring bonds of 2.62(1) Å. These Ga_5 rings sit atop the outer pentagons of the second shell in a staggered configuration. The average Ga(2)–Ga(3) bonds are 2.72(10) Å.

The fourth shell in $[Ga_{84}(N\{TMS\}_2)_{20}]^{n-}$ contains 22 Ga atoms (yellow in Figure **1.26**), 20 of which are ligand-bearing. These ligand-bearing $GaN(TMS)_2$ moieties sit between the Ga_{10} belts in shell three, on alternating square faces. The average Ga(3)–Ga(4) bond for these species is 2.63(14) Å. The two remaining Ga atoms in the outer shell sit along the C_5 axis, capping the pentagonal faces in the third shell. The average Ga(3)–Ga(4) bonds for these two atoms are 2.80(1) Å. The Ga–N bonds in $[Ga_{84}(N\{TMS\}_2)_{20}]^{n-}$ average 1.91(1) Å.

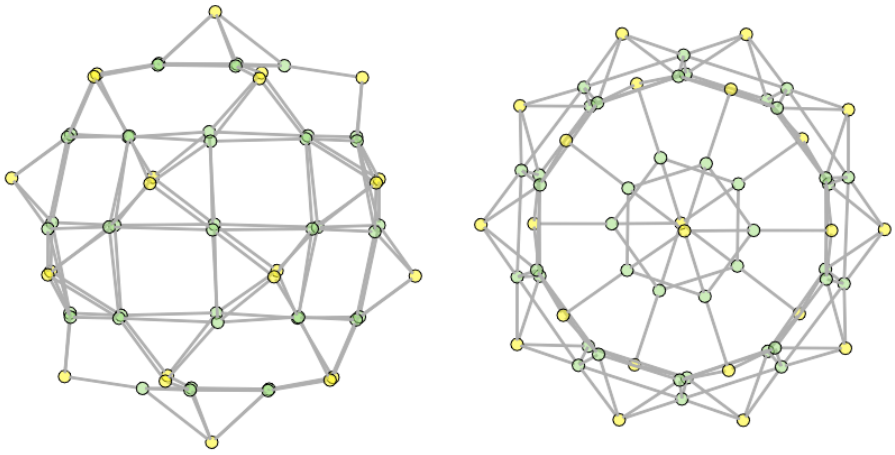

Figure 1.26: X-ray crystal structure of the outer two shells of $[Ga_{84}(N\{TMS\}_2)_{20}]^{n-}$. Side view along C_2 axis (left) and top view down C_5 axis (right) are shown. Light green = Ga_{40} third shell, yellow = Ga_{20} outer shell.

Table 1.5: Bond distances of selected non-metalloid gallium compounds.

Compound	Ga–Ga (ave)	Ga–R	Ga–X	Ox State	Ref
$Ga(NTMS_2)_3$	—	1.91(10)	—	3	127
$[GaI_2PHCy_2]_2$	2.44(1)	2.42(1)	2.59(1)	2	34
$[Ar^*Ga(I)]_2$	2.48(3)	1.98(1)	2.53(3)	2	32
Ga_2Br_4•2diox	2.40(1)	2.05(1)	2.31(1)	2	35
Ar'GaGaAr'	2.63(1)	2.03(1)	—	1	121
NacnacGa	—	2.05(1)	—	1	28
$Cp^*GaCrCO_5$	—	2.26(2)	2.40(1)	1	29
Ar#GaFeCO_4	—	1.94(1)	2.22(1)	1	129
Ga•3PPh_3^+ $AlOR_4^-$	—	2.69(3)	—	1	31

Table 1.6: Bond distances of selected metalloid gallium compounds.

Formula	Ga1-Ga1	Ga1-Ga2	Ga2-Ga2	Ga2-Ga3	Ga3-Ga3	Ga3-Ga4	Ga-R	Ga–X	Ref
$K_2[TripGa]_2Ga_2$	2.47(1)	—	—	—	—	—	2.01(1)	—	33
$[Ga_{12}(fluorenyl)_{10}]^{2-}$	2.64(11)	—	—	—	—	—	2.06(3)	—	65
$Ga_{22}[P^tBu_2]_{12}$	2.68(15)	2.76(7)	2.48(3)	—	—	—	2.44(5)	—	69
$[Ga_{22}Br_{12}(N[TMS]_2)_{10}]^{2-}$	2.53(1)	2.40(1)	—	—	—	—	1.86(2)	2.40(11)	70
$[Ga_{19}(CTMS_3)_6]^-$	—	2.84(11)	2.71(7)	2.50(5)	—	—	2.01(1)	—	68
$[Ga_{51}(P^tBu_2)_{14}Br_6]^{3-}$	—	2.84(8)	2.82(8)	2.68(10)	2.77(18)	2.56(11)	2.37(4)	2.43(1)	77
$[Ga_{84}(NTMS_2)_{20}]^{4-}$	2.25(2)	2.99(30)	2.83(5)	2.72(10)	2.89(19)	2.63(14)	1.91(2)	—	78

1.4. Spectroscopic and applied properties of reduced-state Al and Ga compounds.

The most common characterization technique employed to describe reduced-state Group 13 compounds is single-crystal x-ray diffraction, as discussed in Section 3. Other methods utilized to characterize these compounds include Raman spectroscopy, mass spectrometry, and Nuclear Magnetic Resonance (NMR) spectroscopy.

1.4.1. Raman Spectroscopy

Raman spectroscopy has been employed specifically to shed light on the structural makeup of the gallium subhalide 'GaX_2' and 'GaI' species. The first structural elucidation of a gallium subhalide was presented by Woodward in 1956.[130] 'Fused $GaCl_2$' was melted and the Raman frequencies recorded. The Raman spectrum of $GaCl_2$ contains absorbances at 115, 153, 346, and 380 cm^{-1}. These absorbances are in close agreement with those in the aqueous $[GaCl_4]^-$ ion. Based on this information '$GaCl_2$' was determined to be a mixed-valent species comprised of $[Ga]^+$ and $[GaCl_4]^-$ ions. A similar comparison of the Raman spectrum of '$GaBr_2$' to that of aqueous $[GaBr_4]^-$ ions results in the conclusion that '$GaBr_2$' is comprised of $[Ga]^+$ and $[GaBr_4]^-$ in the liquid state.[79]

Raman spectroscopy has also been utilized to characterize Green's 'GaI'. The green powder was found to be comprised predominantly of $[Ga]^+_2[Ga_2I_6]^{2-}$.[120] The mixture was reported to also contain other gallium sub-iodides.[64]

In the case of low-valent aluminum, little Raman work has been presented. A footnote in the initial report of metastable aluminum chloride attributed the lack of Raman data to the degradation of solution upon exposure to light.[97] Raman spectra of concentrated AlX solutions have not been reported, nor have those of solid AlX.

1.4.2. Mass Spectrometry

Like Raman spectroscopy, mass spectrometry (MS) can be utilized to gain insight into the structure and stoichiometry of reduced-state Group 13 compounds. In theory, cluster growth via disproportionation or reductive methods could be monitored by use of MS techniques over time. In practice, however, no examples of such reaction monitoring have yet been reported.

The tetrameric $[AlCp^*]_4$ is rather air-stable (especially when compared to the majority of reduced-state Group 13 compounds).[131] As a result of this stability $[AlCp^*]_4$ can be handled in air and introduced into typical MS systems (i.e. $[AlCp^*]_4$ does not have the same challenges as most reduced-state Al and Ga compounds). Consequently, crystalline $[AlCp^*]_4$ has been subjected to direct UV laser irradiation in a FT-ICR MALDI mass spectrometer.[132] The energy input from the laser source proved sufficient to initiate cluster growth — numerous cationic compounds were observed, including the $[Al_8Cp^*_4]^+$ ion (see Figure **1.27**).

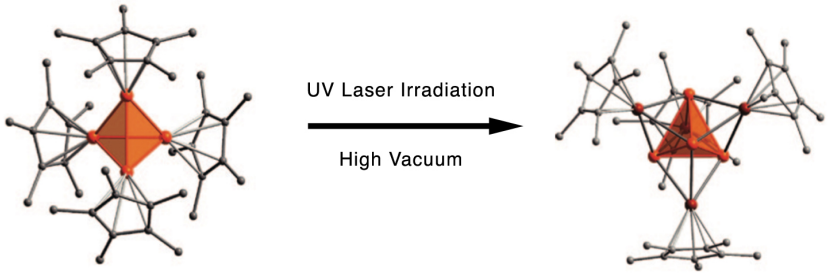

Figure 1.27: Formation and calculated structure of the $[Al_8Cp^*_4]^+$ ion by UV laser irradiation.

While limited MS data has been collected, these results demonstrate a fundamentally important concept: in order to grow larger clusters, energy must be

introduced to the system.[131] In many instances this activation energy is low (and thus disproportionation processes are fast), but in all cases an input of energy is required.

1.4.3. Nuclear Magnetic Resonance and Electron Paramagnetic Resonance

Many low-valent and cluster compounds of aluminum and gallium have been the subjects of Nuclear Magnetic Resonance (NMR) experiments. Such compounds can in theory be characterized by ^{1}H, ^{13}C, ^{19}F, ^{27}Al, ^{29}Si, ^{31}P, and ^{69}Ga NMR, depending on the elemental constitution of the compound in question.

Covalent compounds containing traditional two center – two electron bonding such as Jones' dialane $(PrisoAlH)_2$ and Power's terphenyl-substituted $[Ar_3Al_3]^{2-}$ and $[Ar_2Ga_4]^{2-}$ clusters exhibit expected ^{1}H and ^{13}C NMR spectra.[4,7,33] The chemical shifts for the alkyl and aromatic protons in $(PrisoAlH)_2$ appear in their respective regions with only slight variation from the starting alane (for instance the NHC proton shifts from 6.55 ppm in the alane to 6.42 in the dialane). In $[Ar_3Al_3]^{2-}$ and $[Ar_2Ga_4]^{2-}$ the aromatic and alkyl chemical shifts are also typical, with no large change in chemical shift resonances due to local electronic effects. In general, the NMR spectra for classical organometallic derivatives of reduced aluminum and gallium contain ^{1}H and ^{13}C NMR chemical shifts appearing in their characteristic ranges.

Attempts at obtaining ^{27}Al and ^{69}Ga NMR spectra for these compounds have proven much more difficult. Both aluminum and gallium are quadrupolar (I = 5/2 for aluminum and 3/2 for both ^{69}Ga and ^{71}Ga), oftentimes making signals difficult to obtain. For both $(PrisoAlH)_2$ and $[Ar_3Al_3]^{2-}$ no ^{27}Al signal was observed. Similarly, ^{69}Ga signals in $[Ar_2Ga_4]^{2-}$ were not found.

The solution ^{27}Al NMR spectrum of $[AlCp^*]_4$ has been reported, with a chemical shift found at –80.8 ppm at room temperature ($\omega_{1/2}$ = 140 Hz, referenced to external $[Al(H_2O)_6]^{3+}$).[12] More interestingly, variable-temperature experiments have been utilized to demonstrate the equilibrium between the tetrameric $[AlCp^*]_4$ and monomeric AlCp* (δ = –150 ppm, $\omega_{1/2}$ = 100 Hz) species in solution (see Figure **1.29**).[133] Based on this data, the tetramerization energy for AlCp* has been determined to be –150 kJ mol^{-1}.

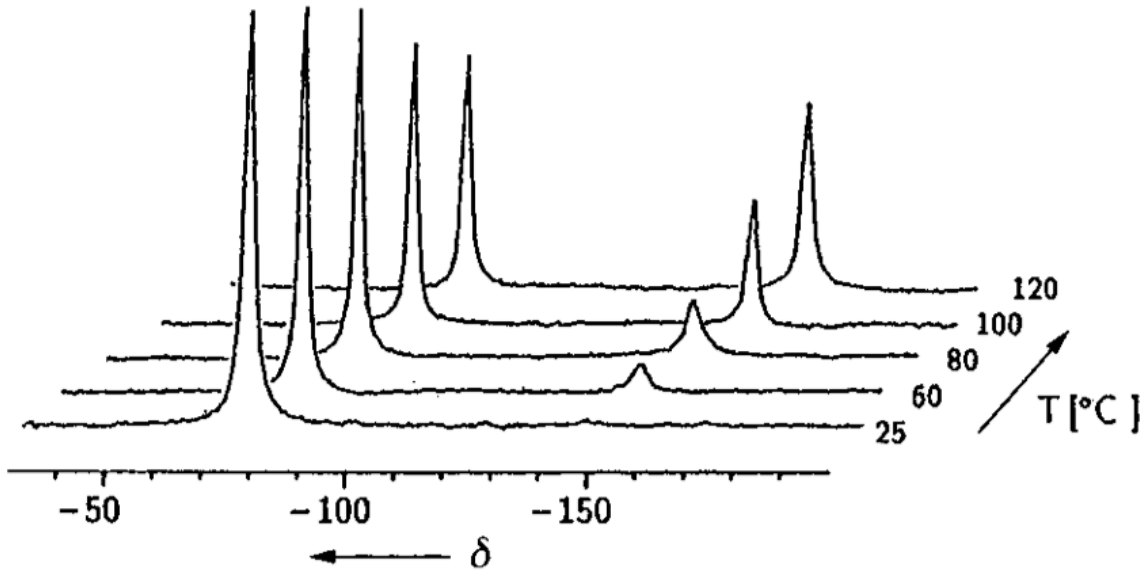

Figure 1.28: Variable-temperature ^{27}Al HMR spectrum of $[AlCp^*]_4$ (recorded in toluene at 70.4MHz, external standard $[AI(H,O),]^{3+}$). Adapted from J. Am. Chem. Soc. **1993**, *115*, 2402–2408**.**

Significant challenges have arisen in attempting to obtain spectra for metalloid cluster compounds, the most daunting of which is the insolubility of most reported compounds in organic solvent. The majority of reported metalloid clusters are not soluble in common deuterated solvents without degradation, prohibiting solution NMR studies. In addition, many of the metalloid clusters are paramagnetic. Looking at alternative and complimentary techniques, solid-state NMR spectroscopy has been employed with limited success.[134]

Limited EPR (Electronic Paramagnetic Resonance) data have been reported for metalloid clusters. In samples that are paramagnetic, similar challenges to those involving NMR arise when obtaining EPR spectra. A few EPR absorbance values have been reported in metalloid clusters: a broad signal is reported for the $[Al_{77}(NTMS_2)_{20}]^{2-}$ cluster, but little further information (including the frequency of the absorbance) is given. The neutral radical $Al_7(SiPhMe_2)_6$ cluster has a solid-state EPR signal with a *g* value of 2.00 but no hyperfine coupling is observed, giving rise to little information about the nature of the radical. Solution spectra were not reported for either compound.

1.4.4. Conductivity of Metalloid Gallium Clusters

Gallium-containing compounds (e.g. gallium (III) arsenide) are commonly used in the semi-conductor industry, and the conducting properties of the metalloid $[Ga_{84}(N[TMS]_2)_{20}]^{4-}$ have been investigated. It was found that at relatively high temperatures (7 K), $[Ga_{84}(N[TMS]_2)_{20}]^{4-}$ acts as a superconductor. This was confirmed using both crystal conductivity and ^{69}Ga NMR experiments.[135,136] While the number of samples for testing is currently limited, metalloid gallium clusters have demonstrated potential as superconductors.

1.5. Overview of Thesis and Objectives.

The objectives of this study have been to first replicate and then expand the chemistry of metastable aluminum and gallium monohalides (discussed in Chapter **2**) at the University of Maryland. This field has been pioneered by Prof Hansgeorg Schnöckel at the University of Karlsruhe.[137] This study marks the beginning of a strong collaboration between Professor Schnöckel, the Bowen group in JHU and the Eichhorn group at UMD; the author trained in Karlsruhe in November 2009 for two weeks with Dr. Christian Schenk, Prof. Eichhorn visited Karlsruhe three times between 2007 and 2009, and Samantha DeCarlo (Eichhorn Group) trained with Dr. Patrick Henke and Dr. Florian Henke for two weeks in June 2011.

To successfully produce aluminum and gallium monohalides, a Metal Halide Co-condensation Reactor (MHCR) was designed, fabricated, and assembled in collaboration with Professor Schnöckel, the Bowen Research Group at The Johns Hopkins University and Dr. James Lightstone of the Indian Head Division, Naval Surface Warfare Center (details of the MHCR design, operation, and replication of Schnöckel's work can be found in Chapter **2**). Over the course of six months (October 2009 – March 2010) the reactor was built in the Bowen Labs by the author and Dr. Xiang Li.

In late February 2010 the MHCR was transferred to the Eichhorn Labs at Maryland. The first successful MHCR experiment was conducted on March 25 2010, producing 120 mL of a GaCl•THF solution. After a number of modifications to the reactor system, we have established the ability to reproducibly generate viable AlCl, AlBr, GaCl, and GaBr solutions and reproduce previously-published metalloid clusters.

Both $[Al_{77}(NTMS_2)_{20}]^{2-}$ and $[Ga_{22}Br_{12}(NTMS_2)_{10}]^{2-}$ clusters have been reproduced and structurally characterized.

To diversify known low-valent aluminum and gallium chemistry, a number of novel ligand systems have been explored as part of the thesis worked described herein. Amidinate ligands were employed to explore the effect of ligand denticity on cluster formation (see Chapter **3**). The synthesis and characterization of three novel aluminum (III) amidinate compounds is described.

In addition to nitrogen-based amidinates, softer phosphorous-based ligands were investigated to better understand the hard/soft nature of monovalent aluminum and gallium (see Chapter **4**). The preparation of two novel paramagnetic Al_3 clusters is described. The paramagnetic nature of these compounds is demonstrated in the solid-state (EPR) and in solution (Evans Method NMR). The bonding is modeled through DFT calculations on a model $[Al_3H_6]^{2-}$ cluster.

2. Metal Halide Co-condensation Reactor Design and Operation.

The discovery and development of metal halide co-condensation techniques has resulted in compounds that have challenged our understanding of the nature of metal-metal bonding. These compounds are formed during disproportionation reactions of metastable metal monohalides.

Introduction of a stream of hydrogen halide gas over molten metals (aluminum, gallium, germanium, tin) at ~1200 K and 10^{-5} torr results in the generation of metal monohalides.[57,97,138,139] Co-condensation of the gas-phase monohalides with a mixed-solvent matrix at 77 K and subsequent thawing and collection under nitrogen results in metastable precursors which can be stored at –80 ºC for months (for cluster synthesis conditions see Section 2.2, for structural details see Section 2.3). Professor Hangeorg Schnöckel at the Karlsruhe Institute of Technology (KIT) in Karlsruhe, Germany has pioneered this preparatory-scale synthetic procedure and we have adapted his methods for use in our laboratory.

2.1. Generation of metastable aluminum and gallium monohalides.

A review of the subhalide chemistry of aluminum and gallium is presented in Chapter **1**. However, the gas-phase generation of aluminum and gallium monohalides is worth revisiting. The general reactor design is based on that of Timms and contains a resistively-heated furnace centered within a stainless steel bell jar.[140]

Aluminum monohalide gases can be generated at high-temperature (approximately 1200 K) and low pressure (ca. 10^{-5} torr) via the reaction of hydrogen halide gas and molten aluminum metal. The interaction between aluminum and HX

results in the gas-phase molecule AlX and hydrogen gas (see Equations **2.1** and **2.2**). Under normal conditions this reaction results in only formation of AlX_3 via Equation **2.1**. At temperatures above 800 K in the gas phase a secondary reaction proceeds via Equation **2.2**, resulting in the formation of primarily AlX. The resultant product distributions typically contain less than 5% AlX_3, though this ratio depends on the hydrogen halide used and the temperature at which the reaction is performed.

$$Al_{(l)} + 3\ HX_{(g)} \xrightarrow{1000\ ^\circ C} 3/2\ H_{2\ (g)} + AlX_{3\ (g)} \qquad (2.1)$$

$$AlX_{3\ (g)} + 2\ Al_{(l)} \xrightarrow{1000\ ^\circ C} 3\ AlX_{(g)} \qquad (2.2)$$

The initial studies of these aluminum monohalide systems were performed by deposition of the generated AlX onto argon matrices. In order to produce further evidence of the existence of AlX and to produce increased quantities for a preparative scale, the reactor system was modified to co-condense the generated AlX molecules at 77 K in an organic solvent matrix.

A schematic diagram of the reactor can be seen in Figure **2.1**. The reactor design contains a diffusion pump (**A**) backed by a mechanical oil pump (**B**). These pumps evacuate a chamber containing a graphite furnace containing open crucibles filled with aluminum metal (**C**). The furnace is heated resistively by a tungsten filament approximately 3 meters long. The furnace is surrounded by a water-cooled jacket (**D**).

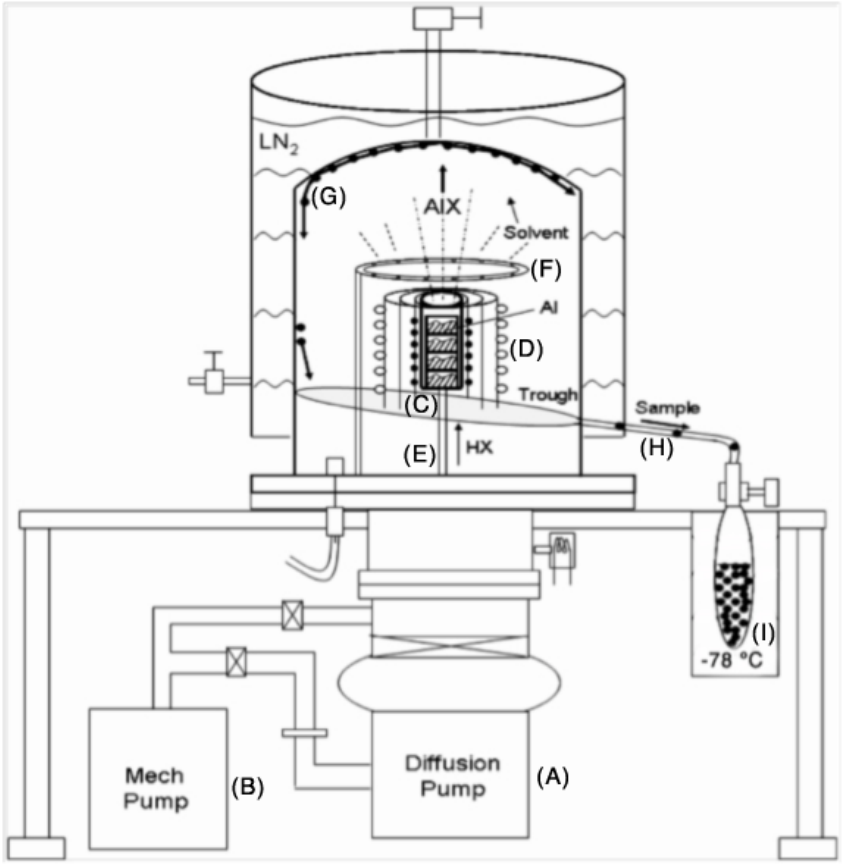

Figure 2.2: Schematic diagram of MHCR. Reactor consists of a graphite furnace containing Al metal, resistively heated furnace, solvent inlet, cooled stainless steel condensation surface, interior trough, and cooled collecting Schlenk.

During operation of the reactor, hydrogen halide gas is introduced into the furnace through a quartz tube (**E**). The generated gas-phase AlX is then co-condensed with gas-phase solvent introduced through a stainless steel halo (**F**) onto the bell jar surface (**G**). Upon completion of the reaction the liquid nitrogen is drained and the deposition matrix thawed. The resultant solution melts down the reactor walls and travels through a stainless steel trough (**H**) into a cooled Schlenk vessel stored at –78 ºC (**I**). The resultant metastable solution can be stored for months at -80 °C.[98] The resultant metal-to-halide ratio is directly proportional to the furnace temperature (i.e. lower temperature yields $AlBr_{1.2}$ while higher temperature will yield $AlBr_{0.9}$).

2.2. Metal Halide Co-condensation Reactor Design.

To successfully produce aluminum and gallium monohalides, a Metal Halide Co-condensation Reactor (MHCR) was designed, fabricated, and assembled in collaboration with Professor Schnöckel, the Bowen Research Group at The Johns Hopkins University and Dr. James Lightstone of the Indian Head Division, Naval Surface Warfare Center. Over the course of six months (October 2009 – March 2010) the reactor was assembled in the Bowen Labs by the author and Dr. Xiang Li.

The first successful MHCR experiment was conducted on March 25 2010, producing 120 mL of a GaCl•THF solution. After a number of modifications to the reactor system, we have established the ability to reproducibly generate viable AlCl, AlBr, GaCl, and GaBr solutions. These modifications include addition of a stainless steel drain tube, performed by Howard Grossenbacher (UMD Aerospace Machine Shop), conversion of gas and solvent inlets from Swagelok to KF connections, storage of metastable monohalide solutions in Schlenk flasks equipped with glass J. Young valves, and installation of a heavy-duty variac (Mastech) to power the resistively heated furnace.

2.2.1. Mass Flow Controller.

The most significant operational change in the UMD MHCR is the use of STEC SEC-4400MC mass flow controllers (MFCs) to introduce hydrogen halide gases into the system. The KIT reactor was designed such that HX was stored at sub-atmospheric pressure in a blown glass bulb and the gas flow was controlled manually by needle valve. The gas delivery was monitored by use of a capacitance manometer, which tracked the pressure in the HX delivery chamber. As the HX reservoir pressure dropped over the course of the reaction the needle valve would need to be adjusted to maintain the proper

gas flow rate. Over time the needle valves degrade due to exposure to corrosive HX, requiring frequent replacement.

The MFCs utilized in the UMD design actively adjust gas delivery, compensating for changes in pressure on both the inlet and outlet sides. This real-time adjustment allows for much more reproducible and accurate gas-delivery. To calculate the flow rate in standard cubic centimeters per minute (sccm), the Ideal Gas Law is reorganized to solve for volume (Equation **2.3**):

$$V = \frac{nRT}{P} \tag{2.3}$$

A typical co-condensation experiment produces 40 mmol of AlX•D over the course of 120 minutes.[97] Calculating the total volume of HX at standard temperature and pressure and using the value of 8.314 cm^3 MPa mol^{-1} K^{-1} for R, results in the following (Equation **2.4**):

$$V = \frac{nRT}{P} = \frac{0.04 mol \bullet 8.314472 \frac{cm^3 \bullet MPa}{mol \bullet K}}{0.101325 \ MPa} = 978.12 \ cm^3 \tag{2.4}$$

Dividing this value over the 120 minutes required for a typical run results in a calculated flow rate of 8.15 sccm.

The entire gas-delivery system has been modified with more modern equipment in the UMD MHCR design. HCl and HBr tanks are connected to their respective MFCs via stainless steel regulators and stainless tubing. Each HX delivery system is connected to an argon line and isolated by a stainless steel stop-valve. This allows for the MFCs to

be purged with and stored under argon after HX introduction is complete, preserving the MFCs from degradation.

The gas flow rate has been found to be a very important variable during the operation of the MHCR. In terms of operational output we value as high a flow rate as possible, as a full reactor run is a two-day process. If the flow rate is too high, however, the resultant solutions do not yield crystalline products (as discovered by trial and error with variable flow rates). As such, the empirically determined optimal flow rate is approximately 8 sccm.

The flow rate in the MHCR is most effectively monitored via the increase in outgas pressure. While the MFC units are controlled digitally, the solenoid valves that control the unit degrade over time upon exposure to corrosive HX. By monitoring the outgas pressure (and overall chamber pressure) the proper flow rate can be achieved. For the UMD MHCR design we have determined the maximum working outgas pressure is between 50 and 55 mtorr (increased from ~30 mtorr prior to HX addition). The overall chamber pressure during gas and solvent addition during a successful reactor run is 1.8-2.2 $\times 10^{-5}$ torr. Higher flow rates (upwards of 10 sccm) result in a higher outgas (80 mtorr) and chamber pressures (3.5 $\times 10^{-5}$ torr) which ultimately do not yield crystalline products.

2.2.2. Water-cooling.

The water-cooling jacket surrounding the reactor furnace has been improved in the UMD model to deliver more uniform cooling. The Karlsruhe design employs wrapped copper tubing welded to a stainless jacket, a design with a relatively small

actively-cooled surface area. The UMD design contains a barrel-shaped water jacket that increases the cooled surface area, thus allowing for better heat dissipation.

2.2.3. Thermocouple additions.

Two K-type thermocouples have been installed in the interior of the MHCR design to allow for monitoring of the furnace temperature. One thermocouple is rested on the outside of the tantalum heat shield and connected via multimeter during the bake-out and gas inlet phases of a co-condensation experiment. During a typical co-condensation reaction the second thermocouple is not utilized.

The temperatures on the outside of the heat shield are significantly lower than those at the top of the furnace (where the oxidation reactions take place). While the temperature relevant to the reaction process is that inside the reactor, an active thermocouple cannot be inserted into the reaction zone as it will react with the active gases genererated. Taking this problem into account a calibration experiment was designed wherein the second thermocouple was placed in the aperture of the furnace and each thermocouple connected to a multimeter and the reactor furnace slowly heated up to ~ 1000 ºC. K-type thermocouple voltage calibration curves are well-known and were used to determine the temperature of the reactor interior. The resulting data were plotted and a calibration curve established for the outer thermocouple. This outer thermocouple is used during typical co-condensation experiments. By combining the calibration curve data with the known K-type calibration values (See Figure 3.2), the reactor temperature can be unobtrusively monitored via the outer thermocouple during a co-condensation experiment.

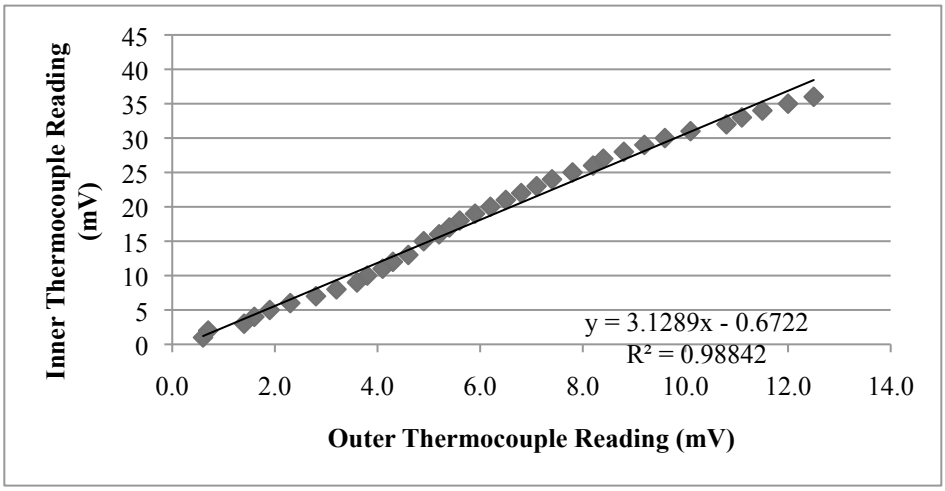

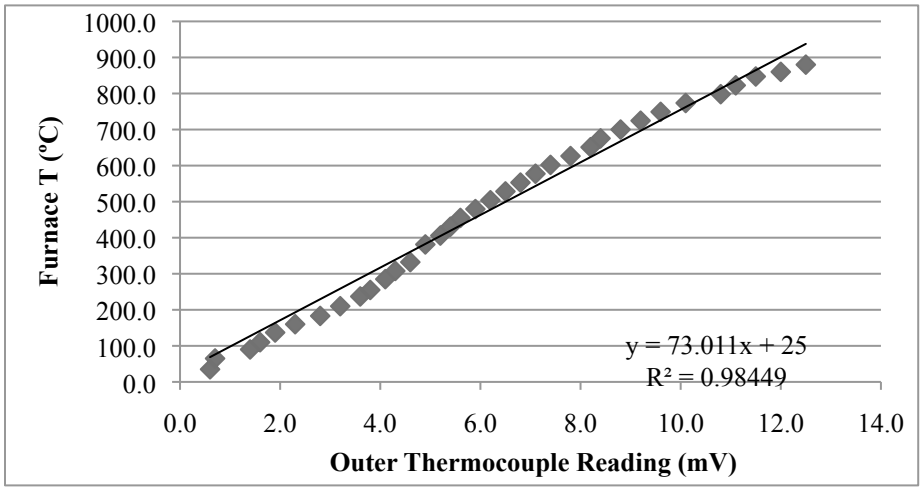

Figure 2.3: Two-thermocouple calibration curve (above) and resultant exterior thermocouple temperature plot (below).

In a typical co-condensation experiment the furnace voltage is set to 120 V. The outer thermocouple reads in the range of 11.6-12.0 mV, corresponding to a furnace temperature of approximately 900 ºC (1173 K).

2.2.4. Mohr Titration.

To obtain an accurate measurement of the halide content of AlX/GaX solutions a Mohr titration is performed on a small aliquot of the co-condensation mixture.[141] In a typical measurement, 1 mL of AlX solution is hydrolyzed with distilled water (see

Equation **2.5**). A dilute potassium dichromate solution is added and the homogeneous yellow solution titrated with 0.1000 M $AgNO_3$. The initial reaction occurs between Ag+ and Cl- ions, forming a white AgCl precipitate (Equation **2.6**). The endpoint of the titration is indicated by formation of red Ag_2CrO_4 (Equation **2.7**). The metal content of the solutions are determined by pre- and post-weighing the furnace assembly.

$$2\ AlCl\ +\ 15\ H_2O \longrightarrow 2\ [Al(H_2O)_6]^{3+}\ +\ 2\ HCl\ +\ H_2 \qquad (2.5)$$

$$NaCl_{(aq)}\ +\ AgNO_{3(aq)} \rightarrow NaNO_{3(aq)}\ +\ AgCl_{(s)} \qquad (2.6)$$

$$K_2CrO_{4(aq)}\ +\ 2\ AgNO_{3(aq)} \rightarrow Ag_2CrO_{4(s)}\ +\ 2\ KNO_3 \qquad (2.7)$$

2.3. Experimental Details.

The experimental procedure for a metal halide co-condensation reaction is a two-day process. A typical experiment ('run') will produce 45 mmol of metal halide. The experimental procedure for an aluminum run is identical to that of a gallium run, differing only in the identity of the metal loaded into the furnace inserts. Similarly, the procedure for producing a metal chloride is identical to that for generating a metal bromide, differing only in the identity of the connected HX gas.

All solvents are purified by distillation and stored over activated molecular sieves under an argon atmosphere prior to use. All solvents are distilled under an argon atmosphere from sodium benzophenone ketyl (toluene, THF, ether) or calcium hydride (triethylamine). All stainless tubing connected to HX lecture bottles is stored under argon and actively purged with argon when exposed to air. Exposure of MFC and attached tubing to air is kept to a minimum.

2.3.1. Metal Halide Co-condensation Reactor Preparation.

The following data were produced during a typical aluminum chloride reactor run, performed on May 12 2011 (notebook reference: DHM-2-46). On May 11, aluminum metal was loaded into graphite furnace inserts and the furnace was assembled with six filled inserts and held together by a graphite rod. The entire furnace assembly was weighed (65.4736 g) and placed inside the silica furnace tube. The HX inlet tubing was attached, the Ultratorr connection between the tubing and quartz reactor tube hand-tightened, and the HX tube connected to the Ultratorr gas inlet. The resistance across the furnace was measured with a multimeter (5.7 Ohm).

The 30 L stainless steel bell jar was placed on top of the reactor assembly and affixed with twelve bolts. The HX inlet tubing was connected to the MFC via a three-way valve and the MFC purged with argon. A 250 mL J. Young valve-equipped Schlenk flask was attached to the drain spout on the bell jar.

The 350 mL solvent addition flask was prepared with 120 mL toluene and 40 mL diethyl ether, cooled to –78 ºC, and degassed. The flask was then connected to the reactor assembly via a 250 mL two-necked round bottom flask. Once all glassware has been introduced the MFC argon purge is stopped and the reactor assembly evacuated with a mechanical pump overnight (23 mtorr ultimate vacuum on diffusion pump outgas thermocouple controller).

2.3.2. Aluminum monochloride synthesis.

After overnight evacuation the diffusion pump heater and cooling water were turned on. The outgas pressure rose to 60 mtorr before returning to 29 mtorr. After an hour the valve between reactor chamber and the mechanical pump was closed and the

diffusion pump butterfly valve opened. The outgas pressure immediately jumped from 29 mtorr to 100 mtorr. The ion gauge was turned on and degassed at this point. The ultimate vacuum reached in the reactor chamber was 8.3×10^{-6} torr and the outgas pressure 30 mtorr.

After an hour of evacuation by diffusion pump the resistive furnace heating variac voltage was slowly increased from 0 to 125 V. The chamber pressure rose to 1.5×10^{-4} torr over the course of 25 minutes and the outgas pressure rose from 30 to 45 mtorr. The thermocouple voltage rose from 0.0 mV to 12.4 mV over the next hour as the reactor chamber heated up. The current flowing through the reactor furnace was 3.8 Ampere.

After two hours of heating the chamber pressure had dropped to 2.5×10^{-5} torr. At this time, the solvent mantle and o-ring heating belt were turned on. Following this the bell jar jacket was filled with liquid nitrogen. The outgas pressure dropped from 45 mtorr to 25 mtorr and the chamber pressure dropped from 2.5×10^{-5} to 3.2×10^{-6} torr.

Upon cooling of the chamber to 77 K, the solvent was introduced into the chamber by a slow dropwise addition (approximately two drops every three seconds). The chamber pressure rose to 8.5×10^{-6} torr, and the outgas pressure rose from 25 to 30 mtorr.

After ten minutes of solvent addition the HCl regulator was manually closed, the HCl lecture bottle opened, and the regulator slowly opened to introduce HCl gas to the MFC. The HCl delivery was steadily increased from 2 sccm to 6 sccm (30% of MFC maximum) over the course of 45 seconds. During this increase the outgas pressure rose from 30 to 50 mtorr as H_2 gas is formed and removed as a byproduct. Upon addition of

HCl the chamber pressure increased to 2.2×10^{-5} torr. The minimum delivery pressure from the regulator to the MFC was maintained for safety purposes. At this point the co-condensation stage is reached and AlCl being produced. The chamber pressure was within the acceptable range of $1.5 – 2.5 \times 10^{-5}$ torr during the metal monohalide generation stage. Periodic reopening of the HCl bottle and addition of liquid nitrogen to the bell jar are required every twenty minutes.

After three hours of AlCl generation the HCl flow was stopped. The remaining solvent in the delivery flask (approximately 15 mL) was subsequently condensed on the reactor walls. After addition of the remaining solvent the diffusion pump was isolated from the chamber by closing the butterfly valve and the diffusion pump and furnace heaters turned off. The liquid nitrogen in the bell jar was drained and the reactor chamber and MFC filled to 0.7 atm with ultrapure argon. The MFC was isolated from the chamber and exposed to three pump/purge cycles with argon. The collection Schlenk was cooled to –78 ºC with dry ice and the flask sidearm cooled with dry ice.

After 45 minutes the solution thaw and drain were complete and the resultant $AlCl•Et_2O$ solution collected in the cooled Schlenk flask. The Schlenk was sealed and transferred to a –80 ºC freezer. The reactor assembly was disassembled and cleaned with acetone, dilute nitric acid, and again with acetone until no yellowing of the acetone wash was observed. The total time required for this reactor run was approximately 24 hours total across two days. The total time required during the second day was 10 hours.

Small aliquots (3 x 1 mL) of the solution were subsequently titrated by the Mohr method and the chloride concentration determined to be 307 mM. The furnace assembly

was weighed post-reaction (64.2778 g) and the aluminum loss recorded (1.1958 g, 44.3 mol). The concentration of aluminum in solution was determined to be 277 mM, resulting in a final Al:Cl ratio of 1:1.1.

2.3.3. Synthesis and characterization of $[Ga_{22}]^{2-}$ and $[Al_{77}]^{2-}$ clusters.

In order to determine the viability of aluminum and gallium monohalides generated by the MHCR, experimental procedures reported in the literature were repeated in the Eichhorn Lab in collaboration with Dr. Yang Peng. These experiments were performed concurrently with the work presented in Chapters **3** and **4**. It should be noted that the crystalline products reported below were formed after reduction of HX flow rate during metal halide generation from 10 to 6 sccm.

2.3.3.1. $[Ga_{12}Br_2(GaBrNTMS_2)_{10}]^{2-}$.

The reaction of metastable GaBr•THF with $Li(NTMS_2)$ was carried out at –78 ºC. The resultant red solution was warmed to room temperature overnight and subsequently heated to 55 ºC for 2 hours. The dark red solution was filtered, concentrated, and stored in a freezer at –15 ºC. The few resultant yellow crystals gave a weak diffraction pattern with a unit cell matching that of the previously-reported $[Ga_{12}Br_2(GaBrNTMS_2)_{10}]^{2-}$ cluster **1**.[70] The crystal structure was solved and found to be identical to the original structure reported by Schnepf (see Figure **2.3**).

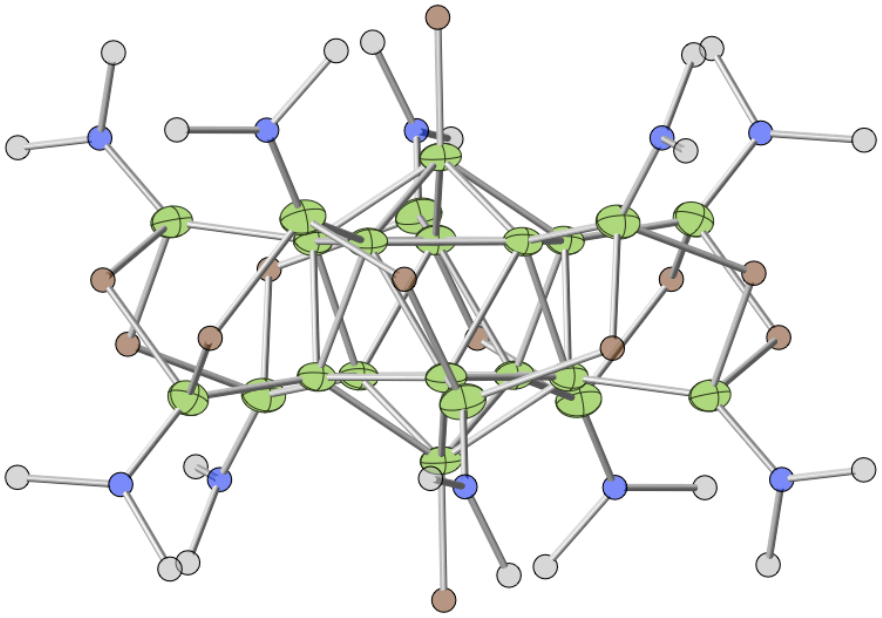

Figure 2.3: X-ray crystal structure of **1**. Green = gallium, blue = nitrogen, silver = silicon, brown = bromine. Thermal ellipsoids displayed at 50% probability, methyl groups omitted for clarity.

This result demonstrates the viability of GaBr solutions produced by the UMD metal halide co-condensation reactor. Following the characterization of 1, efforts were focused on generating viable aluminum solutions.

2.3.3.2. $([Li(OEt_2)_3(\mu_2\text{-}Cl)]^+)_2[Al_{77}(NTMS_2)_{20}]^{2-}$.

A solution of cold AlCl•Et_2O was mixed with solid $LiNTMS_2$ at room temperature and subsequently heated to 65 ºC. Upon filtration, concentration, and subsequent storage at 65 ºC, the dark brown solution produced a few black crystals of $([Li(OEt_2)_3(\mu_2\text{-}Cl)]^+)_2[Al_{77}(NTMS_2)_{20}]^{2-}$ (**2**) after two weeks. The Al_{77} dianion in **2** (see Figure 2.4) is structurally identical to the $[Al_{77}(NTMS_2)_{20}]^{2-}$ anion in $([Li(OEt_2)_3(\mu_2\text{-}I)]^+_2[Al_{77}(NTMS_2)_{20}]^{2-})$ (**2a**) reported by Ecker.[27] The only difference between **2** and **2a** is the identity of the cationic unit, which contains a bridging chloride ion in **2** rather than the bridging iodide present in **2a**.

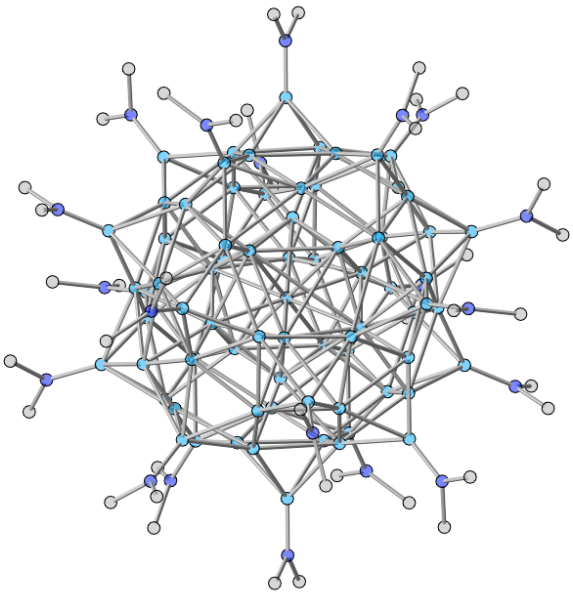

Figure 2.4: X-ray crystal structure of the anionic $[Al_{77}(NTMS_2)_{20}]^{2-}$ cluster **2**. Light blue = aluminum, blue = nitrogen, silver = silicon. Thermal ellipsoids displayed at 50% probability, methyl groups omitted for clarity.

The synthesis of **2** from a solution of AlCl•Et_2O establishes the viability of metastable AlCl solutions produced in the MHCR. More intriguingly, it shines light on a second reaction pathway by which Al_{77} clusters can be produced. Previously, the reaction of AlCl•Et_2O with $LiNTMS_2$ has produced $[Al_7(NTMS_2)_6]^-$, $[Al_{12}(NTMS_2)_8]^-$, and $[Al_{69}(NTMS_2)_{18}]^{3-}$ clusters (see Section 1.2.4.2.1 for details). The formation of the Al_{77} cluster from the reaction of AlCl•Et_2O and $LiNTMS_2$ is highly unexpected and suggests special stability of the $[Al_{77}(NTMS_2)_{20}]^{2-}$ cluster.

Crystals of **2** have been produced during three separate reactions from the same AlCl•Et_2O solution, and the repeated synthesis and further characterization is ongoing. The successful synthesis and structural characterization of **1** and **2** demonstrate the ability of the MHCR described above to generate viable metastable aluminum and gallium monohalides for use in disporportionation reactions. Furthermore, both chloride and

bromide solutions have produced crystalline products, allowing for four different elemental identities of viable precursor solutions (AlCl, AlBr, GaCl, GaBr).

3. Preparation and Characterization of Aluminum (III) Amidinate Complexes.

3.1. Introduction.

Aluminum (III) compounds are important Lewis Acids employed in a number of applications, most famously as co-catalysts in the Ziegler-Natta process. Amidinate ligands of the formula $[RC(NR)_2]^-$ are not as well-studied as many other ligand types, mostly finding uses in lanthanide and actinide chemistry.[142]

Numerous aluminum metalloid cluster compounds have been reported by Schnöckel and coworkers, ranging in size from 7 to 77 atoms.[17,27] These remarkable compounds are synthesized from metastable aluminum monohalide precursors AlX•D (X = Cl, Br, I; D = Et_2O, THF, dioxane, NEt_3) generated at approximately 1200 K in a metal halide co-condensation reactor. Upon warming above –78 ºC the solutions begin to undergo disproportionation reactions, according to Equation **3.1**.

$$3AlX \xrightarrow{heat} 2\ Al + AlX_3 \qquad (3.1)$$

Cluster formation is highly dependent on the binary makeup of the precursor solution (both identity of halide and metal:halide ratio), the temperature of reaction, order of reaction steps, and ligand type. The ligands studied by Schnöckel include η^5-carbon and carbon/phosphorous ligands,[12,24] amide ligands,[17,26,27] phosphide ligands,[14] and alkoxides.[20] The sensitivity of aluminum monohalides to reaction conditions has resulted in a wide variety of structures with a limited number of ligand compounds.

We have recently constructed a Schnöckel-type metal halide co-condensation reactor (MHCR) in collaboration with the Bowen group at The Johns Hopkins

University. Our initial studies have been focused on expanding the variety of ligands reacted with aluminum monohalides. Oxygen-based ligands have been reported twice as ligands in Al-cluster compounds, but have not been extensively studied.[10,20] We initially considered employing carboxylate ligands due to their bidentate nature — no metalloid aluminum or gallium clusters with bidentate ligands have been reported. However, concerns of aluminum oxidation via oxygen transfer from the carboxylates precluded the use of carboxylate ligands.

As an alternative to carboxylates, amidinate-type ligands were selected for use. Amidinates are bidentate, isolelectronic with carboxylates, straightforward to prepare, (see Scheme **3.1**), and are known to stabilize reduced-state aluminum compounds.[7] Additionally, numerous metalloid aluminum clusters with nitrogenous ligands have been reported in the literature.[13,17,18,26,27] The steric bulk of amidinates can be finely tuned by changing the N-bound R group (R = alkyl, aryl). As such, the relationship between ligand bulk and cluster formation can be investigated.

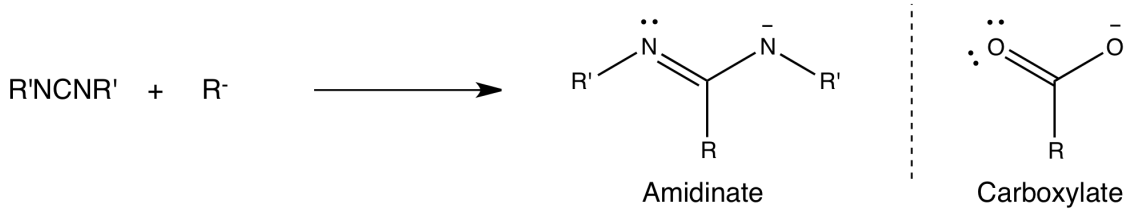

Scheme 3.1: Synthesis and structure of amidinate ligands (left). A generic carboxylate ligand is shown at right for comparison.

We have prepared the neutral aluminum (III) amidinate complexes $Al(PhC(N^iPr)_2)_3$ (**3**), $Al(PhC(NCy)_2)_3$ (**4**), and $Al(PhC(N^iPr)_2)_2Cl$ (**5**) during concurrent ligand metathesis and disproportionation reactions of metastable AlCl•THF. The formation of aluminum cluster compounds via disproportionation requires, by atomic

balance, formation of aluminum (II) and (III) species. Formation of these aluminum (III) compounds suggests viability of future metalloid aluminum amidinate clusters via disproportionation reactions.

3.2. Synthesis of Aluminum (III) Amidinates 3, 4, and 5.

Metastable AlCl generated at 1200 K was trapped in a solvent matrix (3:1 toluene:THF, 160 mL) at 77 K. The resulting reddish-brown solution was warmed to ~200K and collected in a Schlenk vessel stored at –80 ºC. This solution was mixed at –78 ºC with Li[PhC(N^{i}Pr)$_2$] for two hours and subsequently heated to 80 ºC for nineteen hours. The reaction mixtures were then cooled to room temperature, the solvent removed *in vacuo*, and the resultant dark brown residue taken up in pentane. The solution was removed from the colorless lithium chloride byproduct via cannula filtration and subsequently concentrated. Upon standing for two weeks at –15 ºC **3** crystallized from the dark brown solution as colorless plates. Heteroleptic aluminum amidinates **4** and **5** were prepared via similar procedures.

3.3. Solid-state structures of 3, 4, and 5.

The x-ray crystal structure of **3** is shown in Figure **3.1**. Compound **3** is a homoleptic molecule centered about a hexacoordinate aluminum atom. The Al–N bond lengths in **3** are on average 2.016(25) Å. The N–C$_{iPr}$ bond distances are 1.474(1) Å, and the N–C(N) bonds are 1.334(1) Å. The N–Al–N angles average 65.6º±0.4º. the N–C–N angles 111.6±0.9º. These bond distances and angles are in close agreement with those in the homoleptic aluminum guanidinate complex (Me$_2$NC(N^{i}Pr)$_2$)$_3$Al, which has Al–N bonds averaging 2.024(1) Å, N–C$_{ipr}$ bonds of 1.408(2) Å and N–C(N) bonds of 1.331(2) Å. The N–Al–N bond angle is 65.7±0.1º.[143]

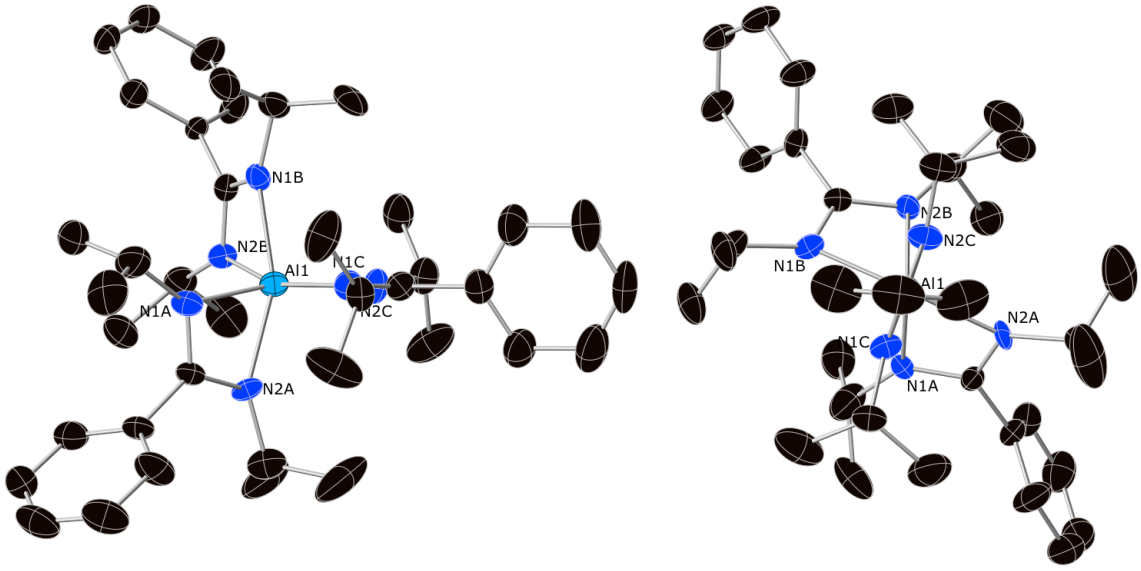

Figure 3.1: Side (left) and top (right) views of **3**. Aluminum = light blue, nitrogen = blue, carbon = black. Hydrogens omitted for clarity, thermal ellipsoids shown at 50% probability.

The heteroleptic amidinates **4** and **5** both adopt pentacoordinate C_2 structures (see Figure **3.2**). The central aluminum atoms in both **4** and **5** adopt trigonal bipyramidal coordination geometries, with the single chlorine atoms residing in the trigonal plane.[144] The Al–N bond distances in **4** are on average 1.946(3) Å (1.961(35) Å in **5**), shorter than those in **3** due to the decreased coordination number. The Al–Cl bond distances for **4** and **5** are 2.20(1) and 2.19(1) Å, respectively. The N–C(N) and N–C_R bonds in **4** are 1.500(1) and 1.334(1) Å, respectively (1.468(2) and 1.321(1) Å in **5**).

The structures of **4** and **5** are quite similar to the heteroleptic aluminum amidinate Al(MeC(N^{i}Pr)$_2$)$_2$Cl.[144] The Al–N bond lengths in Al(MeC(N^{i}Pr)$_2$)$_2$Cl are 1.98(6) Å and the Al–Cl bonds 2.16(1) Å. The N–C_{iPr} bonds in Al(MeC(N^{i}Pr)$_2$)$_2$Cl are 1.47(1) Å, the N–C(N) bonds 1.33(1) Å.

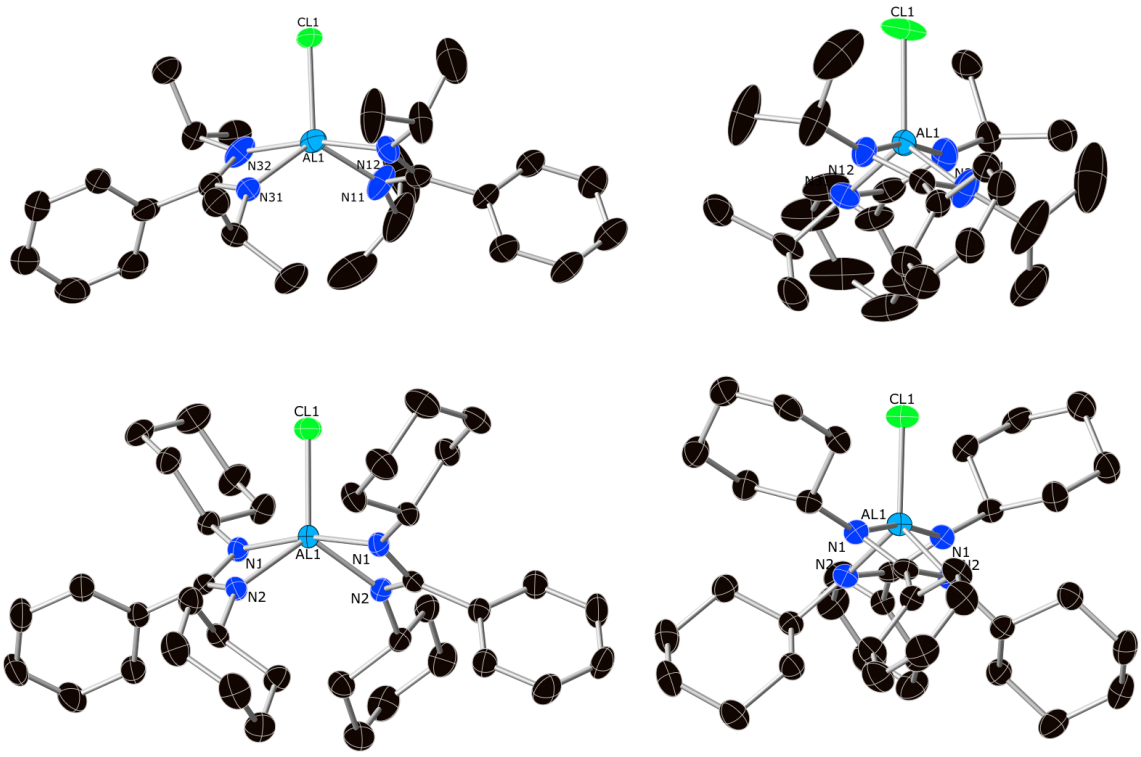

Figure 3.2: X-ray crystal structures of **4** (top) and **5** (bottom). Two views of each structure are shown. Aluminum = turquoise, nitrogen = blue, carbon = black. Hydrogens omitted for clarity, thermal ellipsoids shown at 50%.

The ligand moieties are largely unaffected upon ligation to aluminum, as would be expected. The x-ray crystal structure of Li[PhC(N^{i}Pr)$_2$]•THF (**6**) has been recorded, showing that **6** is dimeric in the solid state. The lithium atoms in **6** are tetravalent, each bound to one bridging and two terminal nitrogen atoms as well as a THF molecule. The N–C(N) bonds in **6** are 1.35 Å, and the N–C–N bond angle is 116.2º. A summary of bond distances and angles in **3**, **4**, **5**, and **6** can be found in Table **3.1**.

Table 3.1: Selected Bond Distances and Angles in **3**, **4**, **5** and **6**

$Al(PhC(N^iPr)_2)_3$ (**3**)

Atoms	distance/angle
Al–N1A	1.979(4)
Al–N1B	2.018(6)
Al–N2A	2.018(4)
Al–N2B	2.018(6)
Al–N3A	2.030(5)
Al–N3B	2.030(5)
$N–C_r$	1.474(1)
N–C(N)	1.334(1)
N–C–N	111.6±0.9º
N–Al–N	65.58±0.3º

$Al(PhC(N^iPr)_2)_2Cl$ (**4**)

Atoms	distance/angle
Al–N11	1.894(2)
Al–N12	1.914(1)
Al–N31	1.983(1)
Al–N32	1.990(1)
Al–Cl	2.195(1)
$N–C_r$	1.500(1)
N–C(N)	1.334(1)
N–C–N	109.7±0.2º
N–Al–N	68.0±0.1º
N–Al–Cl	108.0±12.9º

$Al(PhC(NCy)_2)_2Cl$ (**5**)

Atoms	distance/angle
Al–N1A	1.926(1)
Al–N1B	1.926(1)
Al–N2A	1.996(3)
Al–N2B	1.996(3)
Al–Cl	2.186(1)
$N–C_r$	1.468(2)
N–C(N)	1.321(1)
N–C–N	111.0±0.1º
N–Al–N	68.03±0.1º
N–Al–Cl	109.8±13.8º

$[LiPhC(N^iPr)_2)•THF]_2$ (**6**)

Atoms	distance/angle
Li1–N2	2.012(2)
Li1–N3	2.042(2)
Li1–O1	1.938(3)
N–C(N)	1.345(2)
$N–C_r$	1.448(1)
N–C–N	116.2±0.1º
N–Li–N	88.0±22.0º
N–Li–O	117.3±3.4º

3.4. Discussion.

Metastable aluminum (I) halides are known to undergo disproportionation reactions and form aluminum metal and aluminum trihalides at temperatures above –78 ºC (Equation **5.1**). In order to stabilize metalloid aluminum clusters ($Al_nR_mX_l$ or Al_nR_m where $n > |m + l|$), nucleophilic ligand compounds are added to undergo ligand metathesis reactions. Due to the high reactivity of many aluminum monohalide solutions, these reactions are typically run at –78 ºC and subsequently allowed to warm. The simplest model for these reactions is a ligand metathesis reaction followed by subsequent disproportionation of 'AlR' compounds (Equation **5.2**). However, evidence for this mechanism is not abundant and it is possible for the reaction to proceed via disproportionation followed by ligand metathesis—or for the processes to occur concurrently (Equation **5.3**).

$$3\ AlCl \rightarrow 2\ Al + AlCl_3 \tag{5.1}$$

$$3\ AlCl \bullet Et_2O + 3\ LiR \xrightarrow{-LiCl} 3\ AlR \bullet Et_2O \xrightarrow{heat} 2\ Al + AlR_3 \tag{5.2}$$

$$3\ AlCl \bullet Et_2O \xrightarrow{heat} 2Al + AlCl_3 \xrightarrow{3\ LiR} 2\ Al + AlR_3 + 3\ LiCl \tag{5.3}$$

The formation of **1** does not provide any significant insight into elucidating the mechanism of the reaction of AlCl•THF with lithium amidinates, as trisubstituted homoleptic aluminum (III) structures are the product of both reaction pathways. The structures of **4** and **5** do little to provide insight into the reaction mechanism, as aluminum (III) compounds are known to undergo ligand exchange reactions (Equation **5.4**).[143]

$$AlCl_3 + 2\ AlR_3 \rightarrow 3\ AlClR_2 \tag{5.4}$$

Taking Equation **5.4** into account, we cannot definitively assign a mechanism for formation of **3**, **4** and **5** from AlCl•THF solutions as the products could arise from a number of different pathways. The dark color of the reaction mixtures and slight aluminum mirror deposition in all reactions suggest viability of amidinate ligands in metalloid cluster synthesis, and investigations are ongoing with metastable aluminum and gallium monohalide solutions. Further, it may be possible to reduce **4** and **5** to aluminum (II) derivatives.[7]

3.5. Experimental Details.

General considerations: All reactions are performed under a dinitrogen atmosphere in a glovebox or under argon using standard Schlenk techniques. Toluene, diethyl ether and tetrahydrofuran were purified by distillation from sodium benzophenone ketyl under a dinitrogen atmosphere. All purified solvents were stored in modified Schlenk vessels over 3 Å molecular sieves under a dinitrogen atmosphere. X-ray crystallographic analysis was performed by Dr. Peter Zavalij at the University of Maryland.

Al(PhC(N^{i}Pr)$_2$)$_3$ (**3**) and *Al(PhC(N^{i}Pr)$_2$)$_2$Cl* (**4**) : Li(PhC(N^{i}Pr)$_2$) (1.45 g, 7.0 mmol) was dissolved in toluene (10 mL) and cooled to –78 ºC. To this suspension was added cold AlCl•THF (6.6 mmol, 17.6 mL of a 380 mmol solution in tol:THF 3:1) via syringe. The resultant brown reaction mixture was warmed to rt over the course of two hours and then heated to 60 ºC for 16 h. The reaction mixture was subsequently cooled to room temperature and the solvent removed in vacuo. Extraction of the brown residue into pentane (50 mL) and filtration via cannula resulted in a dark brown solution. This solution was concentrated to ~10 mL, from which colorless blocks of **3** were obtained.

Further filtration and concentration of the solution resulted in a few pale yellow crystals of **4**.

Al(PhC(NCy)$_2$)$_2$Cl (**5**): Dicyclohexylcarbodiimide (1.044 g, 5.06 mmol) was dissolved in 10 mL toluene at room temperature. To this solution was added phenyllithium (5.06 mmol, 2.5 mL of a 2.0 M solution in dibutyl ether) and the reaction mixture stirred for one hour. The resultant yellow solution was cooled to –78 ºC and cold AlCl•THF (4.82 mmol, 20 mL of a 240 mM solution in toluene:THF 3:1) was added quickly via syringe. The resultant brown solution was slowly warmed to room temperature overnight. The reaction mixture was subsequently concentrated to ca. 10 mL, filtered via cannula, and stored at –15 ºC for ten days, after which a few pale yellow plates of **5** formed on the glass wall.

4. $Li_2[Al_3(PR_2)_6]$•$2Et_2O$: A Neutral Al_3 Radical Cluster

4.1. Introduction.

Over the course of the past twenty-five years there has been an increased focus on the low oxidation state chemistry of the main group elements.[145] A number of compounds have been prepared via reductive pathways, employing large organic ligands to kinetically stabilize the low-valent compounds.[3,9,146] These methods, which utilize traditional reducing reagents (alkali metals, KC_8, sodium naphthalide) have proven to be successful in reducing higher-oxidation state precursors. New reducing reagents such as Jones' Mg (I) dimer have shown great promise in reducing main-group compounds.[7,147,148] However, reductive methods rarely produce cluster compounds containing more than two main-group atoms; a few examples of such compounds include Uhl's $[Al_{12}{}^{i}Bu_{12}]^{2-}$, Robinson's $[Ga_3Ar''_3]^{2-}$, and Power's $[Ga_4Ar^*_2]^{2-}$ and $[Al_3Ar''_3]^{2-}$ clusters (Ar'' = C_6H_3-2,6-(C_6H_2-2,4,6-Me_3)$_2$); Ar* = C_6H_3-2,6-(C_6H_2-2,4,6-$^{i}Pr_3$)$_2$).[4,33,84,95]

An alternative route to low-valent compounds involves the use of metastable main-group monohalides prepared via sonication (M = Ga) or by high-temperature metal halide co-condensation techniques (M = Al, Ga, Ge, Sn).[82,98,149] Subsequent ligand metathesis and disproportionation reactions with these solutions (which often occur concurrently) have resulted in a number of remarkable metalloid cluster compounds, including (but not limited to) $[Al_{77}(N(TMS)_2)_{20}]^{2-}$, $[Ga_{84}(N(TMS)_2)_{20}]^{4-}$, $[Ge_{14}[Ge(TMS)_3]_5]^{3-}$, and $Sn_{10}[Si(TMS)_3]_6$ (TMS = $Si(CH_3)_3$).

While the number of aluminum cluster compounds has been steadily increasing since the discovery of metastable monohalide precursors, the scope of ligands used has been rather limited. Phosphide ligands have been used in preparing clusters upon reaction

with aluminum and gallium monohalides, but only two phosphides (lithium di-tert-butylphosphide and lithium di-isopropylphosphide) have been reported. We hypothesized that soft phosphorous-based ligands could stabilize low-valent aluminum and gallium clusters. With this in mind, we selected lithium diphenylphosphide and lithium dicyclohexylphosphide as ligands to employ in reactions with metastable Group 13 monohalides.

The novel Al cluster compounds $Li_2Al_3(PR_2)_6$•$2Et_2O$ clusters (**7** R = Ph, **8** R = Cy) have been synthesized by reaction of metastable AlCl•Et_2O at –78 ºC with $LiPR_2$ in a toluene:THF mixture after warming to room temperature and subsequent heating to 65 ºC. Both **7** and **8** crystallize as orange plates in moderate yields. The average oxidation state of aluminum atoms in **7** and **8** is +1.33. Compound **8** is paramagnetic in the solid-state and in solution, as determined by EPR and NMR spectroscopic techniques.

4.2. Synthesis of $Li_2[Al_3(PR_2)_6]$ clusters 7 and 8.

Metastable AlCl generated at 1200 K was trapped in a solvent matrix (4:1 toluene:Et_2O, 160 mL, Al:Cl ratio 1:1.03) at 77 K. The resulting reddish-brown solution was warmed to ~200K and collected in a Schlenk vessel stored at –198 K. This solution was mixed at –78 ºC with $LiPPh_2$ for two hours and subsequently warmed to room temperature. The resulting dark brown solution was concentrated to half volume, filtered to remove LiCl, and further concentrated to ~10 mL before being heated to 65 ºC for 48 hours, after which orange blocks of $Li_2[Al_3(PPh_2)_6]$•$2Et_2O$ (**7**) formed on the walls of the flask. A similar procedure using a different AlCl•Et_2O solution (3:1 toluene:Et_2O, 160 mL, Al:Cl ratio 1:1.10) and $LiPCy_2$ produced $Li_2[Al_3(PCy_2)_6]$•$2Et_2O$ (**8**) in low yield.

The average oxidation state of aluminum atoms in **7** and **8** is (+1.33), requiring partial oxidation of aluminum during cluster formation; the oxidation state of the AlCl precursors used in forming **7** and **8** are (+1.0) and (+1.1), respectively. Metastable aluminum monohalide solutions are known to undergo disproportionation reactions at temperatures above 198 K, not requiring external oxidizing or reducing agents to produce oxidized and reduced products.[97] Through disproportionation, **7** and **8** are formed (Equation **4.1**).

$$4\ AlCl \bullet Et_2O + 6\ LiPR_2 \xrightarrow{heat} Li_2[Al_3(PR_2)_6] \bullet 2Et_2O + Al + 4LiCl \qquad (4.1)$$

The orange crystals of **7** and **8** are extremely air- and moisture-sensitive in solution and in the solid state. **7** is soluble in benzene and benzene:DMF (5:1 v:v) mixtures but decomposes in THF. The diphenylphosphide complex **1** has been characterized by single-crystal X-ray diffraction, ^{1}H NMR (Evans Method), and solid-state EPR spectroscopy. The dicyclohexylphosphide complex **8** has been characterized by single-crystal X-ray diffraction.

4.3. Solid-State Structures.

The $Li_2[Al_3(PPh_2)_6]\bullet 2Et_2O$ (**7**) complex crystallizes from toluene in a triclinic unit cell. In the solid-state **7** exhibits whole-molecule disorder, having two equally populated orientations of the Al_3 core and six phosphide ligands. The lithium ions are the only atoms common to both orientations (See Figure **4.1**). In addition to being randomly disordered, the crystals of **7** are multiply twinned and contain a disordered solvate molecule. However, the multiple disorders were successfully modeled to give a reliable structural solution (See Figure **4.2**). A summary of the crystallographic data for **7** can be found in Table **4.1**. Selected bond distances and angles are given in Table **4.2**.

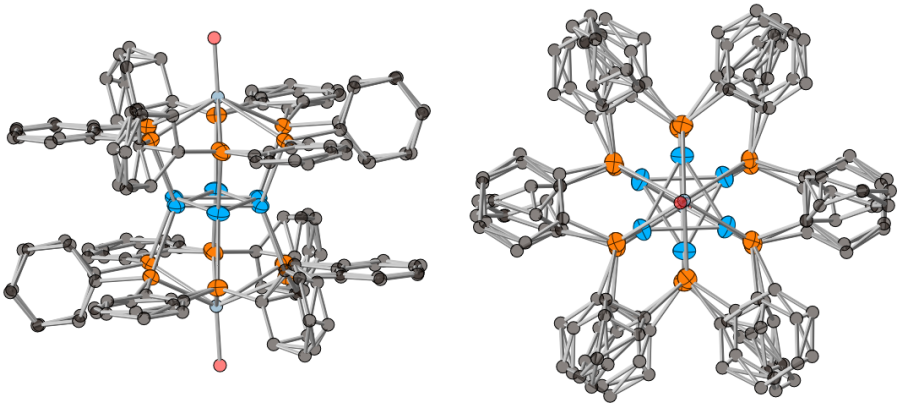

Figure 4.1: View along C_2 (left) and C_3 (right) axes of disordered X-ray crystal structure of **7**. Aluminum = blue, phosphorous = orange, carbon – black, lithium = light blue, oxygen = red. Hydrogen atoms and disordered diethyl ether carbon atoms omitted for clarity. Thermal ellipsoids (Al, P) shown at 50% probability.

Table 4.1. X-ray Crystallographic data for $Li_2[Al_3(PPh_2)_6]$•$2Et_2O$ (**7**).

Compound	$C_{87}H_{88}Al_3Li_2O_2P_6$	β (°)	107.2191(12)
Formula Weight	1446.21	γ (°)	117.4940(12)
Temperature (K)	80	volume (Å^3)	1998.7(3)
Wavelength (Å)	12.8213(10)	Z = 1	
Crystal system	Triclinic	Dcalc (Mg/m^3)	1.202
Space group	P -1	ab. coeff.,mm^{-1}	0.214
Unit cell dimensions		final R indices	
a (Å)	12.8213(10)	R_1, I>2σ(I)	7.22%
b (Å)	13.7634(11)	wR_2, (all data)a	14.62%
c (Å)	13.9032(11)	GOF	1.000
α (º)	95.5268(13)		

$$R_{int} = \Sigma|F_o^2 - F_o^2(\text{mean})| / \Sigma[F_o^2] \qquad R_1 = \Sigma||F_o| - |F_c|| / \Sigma|F_o|$$
$$\text{GOF} = S = \{\Sigma[w(F_o^2 - F_c^2)^2] / (n - p)\}^{1/2} \qquad wR_2 = \{\Sigma[w(F_o^2 - F_c^2)^2] / \Sigma[w(F_o^2)^2]\}^{1/2}$$

The $Li_2[Al_3(PPh_2)_6]$•$2Et_2O$ molecule (Figure 1) exhibits virtual D_{3h} point symmetry, defined by the principle 3-fold rotation axis residing along the Li–O bonds and passing through the center of the Al_3 triangle. The average Al–Al bond distances are

2.625(8) Å and the average Al–Al–Al bond angles 60.0±0.3º in **7.** Each aluminum atom is four-coordinate, with bonds to the other two aluminum atoms in the ring and two phosphide ligands above and below the Al_3 plane. The aluminum atoms in **7** have distorted tetrahedral geometry.

The six phosphorous atoms in **7** are four-coordinate and have distorted tetrahedral geometry. Each phosphorus is coordinated to two Ph rings, one Al atom and a Li^+ ion. The average Al–P bond distance in **7** is 2.370(6) Å and the average P–Al–P bond angle is 134.0±0.5º. The average P–Al–Al bond angle in **7** is 109.8±1.3º.

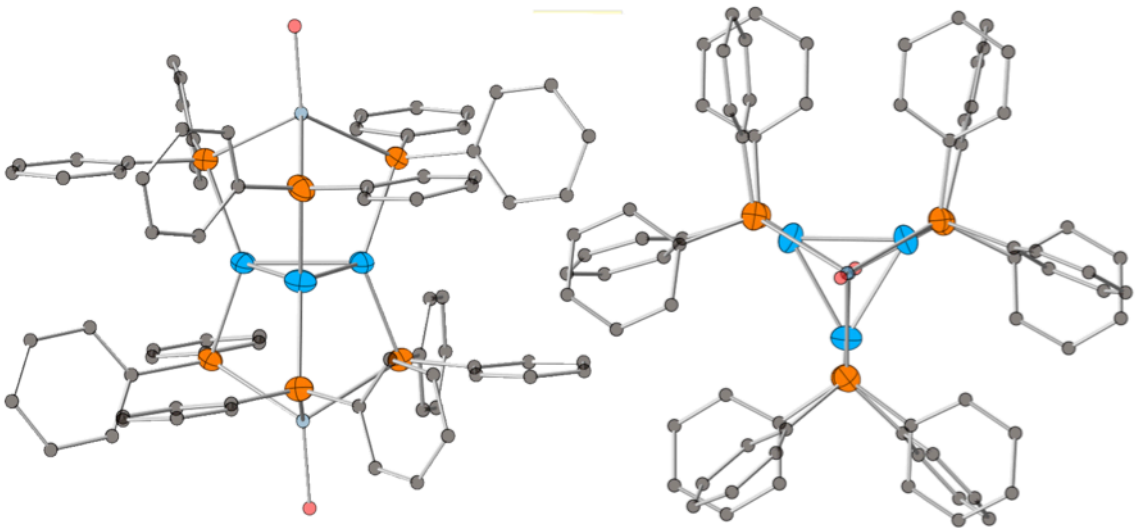

Figure 4.2: X-ray crystal structure of **7** along C_2 axis (left) and along C_3 axis (right). Aluminum = blue, phosphorous = orange, carbon – black, lithium = light blue, oxygen = red. Hydrogen atoms and disordered carbon atoms of bound diethyl ether moieties omitted for clarity. Thermal ellipsoids (Al, P) shown at 50% probability.

The Li^+ ions are tetrahedrally coordinated by three PPh_2 ligands and an Et_2O molecule and cap both sides of the Al_3 plane (Figure **4.2**). The bonding scenario is reminiscent of the capping Na^+ ions in $Na_2[Al_3R_3]$ cluster reported by Wright.[4] The P–Li bonds average 2.704(7) Å in **7**. Both lithium ions have distorted tetrahedral geometries in

7. The remaining Li coordination site is occupied by one disordered diethyl ether molecule (Li–O bond distance = 1.926(1) Å). A full crystallographic report and labeled structure for **7** is given in Appendix **B**.

The X-ray crystal structure of $Li_2[Al_3(PCy_2)_6]$•2 Et_2O (**8**) has proven much more difficult to refine than that of **7**. The crystals of **8** are multiply twinned and exhibit whole-molecule disorder. The entire molecule is distributed equally over two orientations with the exception of the lithium atoms, similar to **7**. In addition to the core disorder, the twelve cyclohexyl groups in **8** each occupy three separate orientations. As such, only a preliminary crystal structure for **8** is reported here. A drawing of the $Li_2Al_3P_6O_2$ core with the non-phosphorous-bound cyclohexyl carbon atoms omitted is shown in Figure **4.3**.

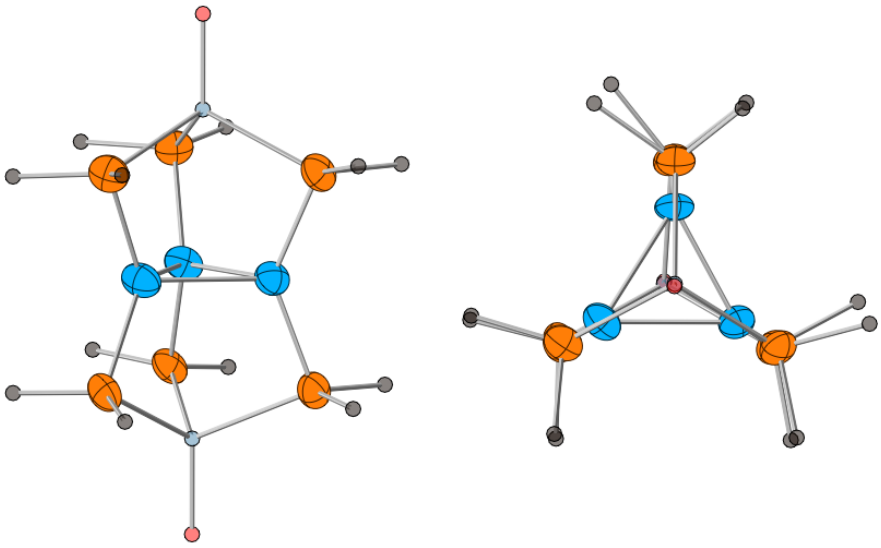

Figure 4.3: Preliminary X-ray crystal structure of **8**. Disordered cyclohexyl groups, diethyl ether ethyl groups and hydrogen atoms omitted for clarity. Aluminum = blue, phosphorous = orange, carbon = black, lithium = light blue, oxygen = red. Thermal ellipsoids displayed at 50% probability.

Table 4.2: Selected bond distances and angles in $Li_2[Al_3(PPh_2)_6]$•2 Et_2O. (**7**)

Atoms	**1**	Atoms	**1**	Atoms	**1**
Al1–Al2	2.617(2)	Al3–P3A	2.368(3)	P3B–Li	2.788(4)
Al2–Al3	2.633(2)	Al3–P3B	2.367(1)	Li–O	1.926(1)
Al1–Al3	2.617(2)	P1A–Li	2.646(2)	P–C (avg)	1.833(12)
Al1–P1A	2.368(1)	P1B–Li	2.689(1)	Al–Al–Al	60.0±0.3º
Al1–P1B	2.368(2)	P2A–Li	2.702(2)	P–Al–P	134.0±0.5º
Al2–P2A	2.369(2)	P2B–Li	2.720(1)	C–P–C	109.8±1.3º
Al2–P2B	2.379(1)	P3A–Li	2.677(2)	P–Li–P	102.9±1.6º

Compounds 1 and 2 contain mixed valent Al (two Al^{+1} and one Al^{+2}) and a total of 17 cluster valence electrons. The odd number of electrons gives rise to non-integral Al-Al bond orders and a paramagnetic S= ½ ground state. At first glance the Al_3 core in **7** is very structurally similar to $Na_2[AlAr'']_3$ (**9**, Ar'' = C_6H_3-2,6-(C_6H_2-2,4,6-Me_3)$_2$), reported by Wright *et al.*[4] However, upon closer inspection it becomes clear that the Al–Al bonding in **7** is significantly different than that in **9**. If one were to only consider the covalent radii of aluminum atoms in **7** and **9** based on the average oxidation state, it would be expected that the bonds in **7** would be longer than those in **9.** In fact, the Al–Al bond lengths in **1** (2.625(8) Å) are significantly longer than the 2.520(1) Å Al–Al distances in **9**. This discrepancy is a result of the higher bond order in **9**; in **9** there are three more electrons present in the Al_3 core. This results in an average bond order of 1.33 in **9**, compared to the 0.83 bond order in **7**. Discussions of the electronic structure are given in Section **4.5**.

The Al_3 core in **9** also directly interacts with the coordinated sodium atoms, interactions which are known to stabilize low-valent metal clusters.[33] In **7** the coordinated lithium atoms serve to template the formation of the Al_3 core, holding the cluster together.

4.4. NMR and EPR spectroscopic studies.

To test for paramagnetism the Evans Method was employed.[150] A small amount of **7** (11.5 mg, 0.00870 mmol) was dissolved in a 5:1 mixture of benzene:DMF (0.50 mL) and sealed in a J. Young NMR tube containing a capillary containing a blank sample of the same 5:1 benzene:DMF mixture. The ^{1}H NMR spectrum was recorded and the contact shift was calculated ($\Delta\nu$ = 23.79 Hz, ν = 400.116 MHz, see Figure **4.4**).

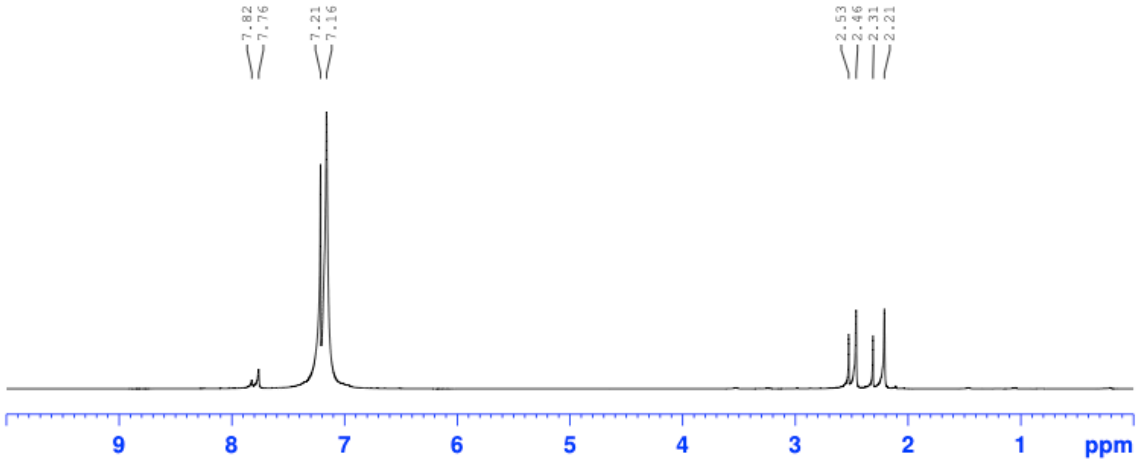

Figure 4.4: Evans Method ^{1}H NMR spectrum (400.12 MHz, 294 K) of a 1.74 mM solution of **7** in benzene/DMF (5:1) with internal capillary filled with benzene/DMF (5:1).

The molar paramagnetic moment χ^P_M is determined using Equation **4.2**:

$$\chi_M^P = \frac{3\Delta\nu M^P}{4\pi\nu m^P} + \chi_0 M^P + \chi_0 M^P \frac{(d_0 - d_s^p)}{m^P} - \chi_M^{dia} \qquad (4.2)$$

Where $\Delta\nu$ is the resulting paramagnetic contact shift in Hz ($|\nu-\nu_0|$), M^P is the molecular weight of **7** in g/mol, ν is the NMR field strength in Hz, m^P is the concentration of **7** in mg/mL, χ_0 is the paramagnetic susceptibility of the solvent, d_0 the density of pure solvent in g/mL, and d_s^p the density of paramagnetic solution in g/mL. χ_m^{dia} is the diamagnetic moment for the solute, calculated to be -0.00086628 emu for **7** using standard tables.[151] The second term can be ignored, as the internal capillary of the same solvent corrects for the solvent susceptibility in the solution. With low concentrations of low density solutes, the third term can also be ignored, as $|d_0-d_s^p|$ approaches zero. With these approximations, Equation **4.2** reduces to Equation **4.3**:

$$\chi_M^P = \frac{3\Delta\nu M^P}{4\pi\nu m^P} - \chi_M^{dia} \qquad (4.3)$$

Inserting the values calculated above, we arrive at a molar paramagnetic susceptibility for **7** of 0.00176263 emu. Inserting this value for $\chi^P{}_M$ into Equation **4.4**

$$\mu_{eff} = 2.828\sqrt{\chi_M^P T} \qquad (4.4)$$

results in the calculated effective magnetic moment is 2.03 Bohr Magneton for **7**. The value for one free electron is equal to 1.73 Bohr Magneton based on Equation **4.5**, where for one free electron S = ½ and g = 2.0023 (the gyromagnetic ratio of an electron).

$$\mu_{eff} = g\sqrt{S(S+1)} \qquad (4.5)$$

The magnetic moment derived from the ^{1}H NMR data confirms that the complex is paramagnetic with an S=1/2 ground state.

To gain more information about the nature of the unpaired electron in **7** the EPR spectrum was recorded in the solid state (see Figure **4.5**). In the solid state a single resonance is observed at g = 2.0023 with complex hyperfine interactions that give rise to a 15 line multiplet. Aluminum has a nuclear spin of 5/2; phosphorous has a nuclear spin of ½. In order to extract more information about the electron, future studies will include recording the EPR spectrum of **7** in benzene solution.

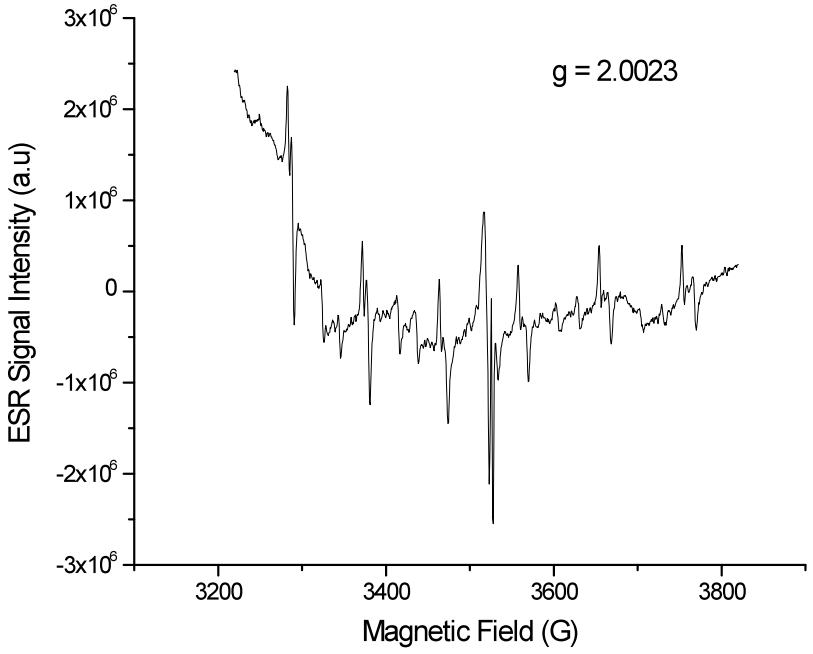

Figure 4.5: Solid-state EPR spectrum of **7**. The fifteen-absorbance signal is symmetrical about the absorbance center at g = 2.0023.

4.5. Electronic Structure and Bonding.

The bonding in **7** has been modeled by using an idealized $[Al_3H_6]^{2-}$ cluster **7a**. Like the core of parent cluster **7**, the total number of electrons in **7a** is 17. The six Al–H bonds require twelve electrons, leaving the remaining five electrons to populate Al–Al

bonding orbitals. The result is a total of 2.5 Al–Al bonds and an average Al–Al bond order of 0.83.

The symmetry operations for the D_{3h} space group were performed on the model compound **7a**. The Al *3s* and *3p* orbitals and six H *1s* orbitals were included. In the D_{3h} point group, the Al $3p_x$ and $3p_y$ orbitals transform together. The resultant irreducible representations are shown in Table **4.3**.

Table 4.3: Irreducible representations for atomic orbitals in $[Al_2H_6]^{2-}$

D_{3h}		E	2 C_3	3 C_2	σ_h	2 S_3	3 σ_v	Mulliken symbols
3 Al	s	3	0	1	3	0	1	e', a_1'
	p_z	3	0	1	3	0	1	e', a_1'
	p_x,p_y	6	0	-2	0	0	0	a_2', a_2", e', e"
6 H	s	6	0	0	0	0	2	a_1', e', a_2", e"

To visualize the molecular orbitals and obtain a better qualitative understanding the bonding in **7,** single-point DFT calculations (6-31G*, Hyperchem) were performed on **7a** (see Figure **4.6**). The atoms in **7a** have 17 available valence electrons. The lowest-energy orbitals are the six involved in Al–H bonding. The filling of these orbitals leaves five electrons to populate the Al–Al bonding orbitals. The HOMO for **7a** is a partially-filled e' set of orbitals. The results of the calculations support our hypothesis that the unpaired electron resides in the Al_3 core, and is consistent with the EPR data.

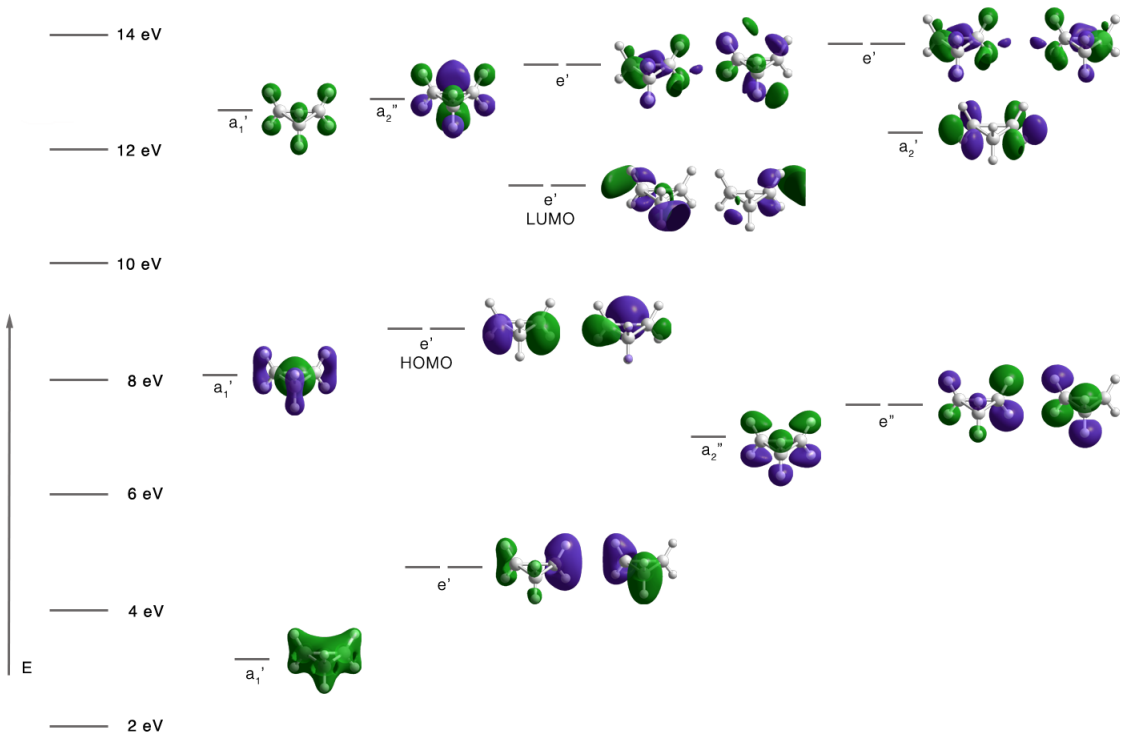

Figure 4.6: Calculated MO diagram for D_{3h}-symmetric model $[Al_3H_6]^{2-}$ cluster **7a**.

4.6. Discussion.

The formation of $Li_2[Al_3R_6]$ clusters **7** and **8** from two separate $AlCl{\bullet}Et_2O$ solutions and with two different ligands suggests relatively high stability of the $Li_2[Al_3(PR_2)_6]$ unit (R = alkyl, aryl). This apparent stability is reminiscent of that of the $[Al_4(P^tBu_2)_mX_{6-m}]$ clusters reported by Henke *et al.* (**10a**, m = 6; **10b** m = 5, X = Br; **10c** m = 5, X = Cl). The average oxidation state of aluminum in **10a-c** is +1.5, similar to the oxidation state in **7** and **8** (+ 1.33). All three $Al_4(P^tBu_2)_6$ compounds **10a-c** are synthesized using different precursor solutions (all varying in concentration), yet all three have markedly similar structures. Similarly, **7** and **8** have both been synthesized from differing precursor solutions (**7** from a 220 mM solution of $AlCl_{1.03}{\bullet}Et_2O$ in 4:1 toluene: Et_2O v:v; **2** from a 270 mM solution of $AlCl_{1.10}{\bullet}Et_2O$ in 3:1 toluene:Et_2O) and contain similar $Li_2[Al_3(PR_2)_6]{\bullet}2$ D structures. This type of generality and reproducibility is

unusual in low valent Al chemistry and is encouraging for developing a systematic investigation of AlCl reactivity.

The lithium ions in **7** and **8** seem to play a role in stabilizing the cluster – when potassium diphenylphosphide was reacted with $AlCl{\bullet}Et_2O$, no $K_2[Al_3(PPh_2)_6]$ clusters crystallized out of the concentrated reaction mixture. Similar ion-specific templating has been previously reported in the $K_2[Ar^*_2Ga_2]Ga_2$ cluster.[33]

4.7. Experimental.

General considerations. All reactions are performed under a dinitrogen atmosphere in a glovebox or under argon using standard Schlenk techniques. Toluene, diethyl ether and tetrahydrofuran were purified by distillation from sodium benzophenone ketyl under a dinitrogen atmosphere. All purified solvents were stored in modified Schlenk vessels over 3 Å molecular sieves under a dinitrogen atmosphere. $AlCl{\bullet}Et_2O$ solutions were generated at 1200 K in a modified Schnöckel-type metal halide co-condensation reactor and stored at –80 ºC.[97] Details of the reactor design and operation are given in Chapter **2**. The chloride content of $AlCl{\bullet}Et_2O$ solutions was determined by Mohr titration.[141]

X-ray crystallographic analysis was performed by Dr. Peter Zavalij at the University of Maryland. The ^1H NMR spectra were recorded at 294 K on a Bruker AM-400 spectrometer operating at 400.1 MHz using a BBI probe. Conventional ESR spectra were obtained with a Bruker EMX ESR Spectrometer (Billerica, MA). All ESR measurements were carried out using the following settings: 3525 G center field; 2.5 mW microwave power, 800 G scan range and 3 G field modulation. All EPR measurements were performed in replicates at ambient temperature.

$Li_2[Al_3(PPh_2)_6]$•$2Et_2O$ (**7**): A solution of n-butyllithium (5.36 mmol, 1.88 mL of a 2.89 M solution in hexanes) was added dropwise to a solution of diphenylphosphine (5.36 mmol, 1.0 g) in diethylether (20 mL) and the resultant yellow solution stirred at room temperature for two hours. The solvent was then reduced *in vacuo* to *ca.* 5 mL and the reaction mixture cooled to –78 ºC. To this yellow suspension was added AlCl•Et_2O (5.10 mmol, 23.2 mL of a 220 mM solution in 4:1 toluene:Et_2O (v:v), Al:Cl ratio 1:1.03) and the resultant heterogenous red mixture stirred at –78 ºC for two hours. The reaction mixture was warmed to room temperature overnight and subsequently concentrated to half volume *in vacuo*. The resultant dark red mixture was filtered via cannula, concentrated to approximately 10 mL, and heated to 65 ºC. After 48 hours, orange plates of **7** formed on the walls of the vessel (120 mg, .0857 mmol, 5% yield based on Al).

$Li_2[Al_3(PCy_2)_6]$•$2Et_2O$ (**8**): A solution of n-butyllithium (2.50 mmol, 0.86 mL of a 2.89 M solution in hexanes) was added dropwise to a solution of dicyclohexylphosphine (2.50 mmol, 500 mg) in diethylether (10 mL) and the resultant pale yellow solution stirred at room temperature for two hours. The solvent was reduced in vacuo to 5 mL and the reaction mixture cooled to –78 ºC. To this yellow suspension was added AlCl•Et2O (2.40 mmol, 8.9 mL of a 270 mM solution in 3:1 toluene:Et_2O (v:v), Al:Cl ratio 1:1.10) and the resultant heterogenous red mixture stirred at –78 ºC for two hours. The reaction mixture was warmed to room temperature overnight and subsequently concentrated to half volume in vacuo. The resultant dark red mixture was filtered via cannula, concentrated to approximately 8 mL, heated to 65 ºC for 48 hours and subsequently cooled to room temperature. After two weeks orange plates of 8 formed on the walls of the vessel (10 mg, .007 mmol, 0.8% yield based on Al).

5. Conclusions.

The reduced oxidation state chemistry of aluminum is quite simply not well-studied. The dearth of examples of reduced oxidation state aluminum compounds is a direct result of the thermodynamic and kinetic instability of such species. While the number of known compounds is limited, the need to develop this chemistry and prepare new metalloid aluminum clusters is important for a number of reasons. First and foremost the chemistry of low-valent aluminum is largely unexplored and unknown; the first well-characterized example of such a compound was reported in 1988.[9] An increased number of such compounds must be prepared and characterized in order better understand the fundamental nature of low-valent aluminum chemistry; only after such gains are made can experiments be rationally designed. Second, the small number of known compounds are rare examples of large clusters that represent the transition between molecular compounds and nanocluster materials. There are no good examples of well-defined compounds that fall in between the molecular and bulk metallic states; large metalloid clusters are perfect candidates for such studies. Third, aluminum nanoparticles such as those demonstrated in the ALICE project have demonstrated great potential.[152] Based on theoretical calculations, metalloid aluminum clusters should have very high heats of combustion, making them excellent candidates for energetic materials. Fourth, the catalytic properties of low-valent aluminum compounds are not known and should be explored, as aluminum compounds are important in a number of industrial processes. A fundamental understanding of disproportionation and cluster growth processes are critical in advancing these goals; this study has focused on these aspects of metalloid cluster formation.

To date, all examples of low-valent aluminum compounds have come from reductive chemistry or through the disproportionation of ill-defined metastable aluminum monohalide precursors. The resultant products are often not predictable and can difficult to reproduce. Currently, the disproportionation of metastable aluminum monohalides remains the only synthetic route to successfully produce metalloid cluster compounds. A controlled, rational methodology is essential in order to better understand the basic nature of such materials and to increase our ability to predict reaction products.

One rather lofty goal in low-valent aluminum chemistry is to selectively synthesize a specific cluster compound from monohalide precursors through reductive methods, rather than through the atom-inefficient disproportionation pathways utilized to date. During the course of this study we have made a number of empirical observations regarding the effects of reducing agents on aluminum monohalides. First, the reduction potential for aluminum monohalides seems to be far smaller than that of aluminum (III) compounds; deposition of aluminum metal is observed during the reaction of AlCl or AlBr with common reducing agents such as KC_8, methyllithium, phenyllithium, n-butyllithium, lithium aluminum hydride, sodium borohydride, and sodium triethylborohydride. In the presence of ligands, however, deposition of aluminum metal was not always observed. By combining this knowledge with electrochemical methods, it should be possible to find an appropriate reducing agent that allows for partial reduction of monovalent aluminum species to reliably form metalloid cluster compounds.

One of the most readily controlled variables in cluster formation is the nature of the added ligand. We surmised that phosphorous-based ligands could have favorable orbital overlap with aluminum and would stabilize low-valent aluminum compounds. To

test this hypothesis, we explored the reactions between $LiPPh_2$ and $LiPCy_2$ with $AlCl{\bullet}Et_2O$, which resulted in the Al_3 clusters **7** and **8**. The only other reported aluminum phosphide clusters prepared via disproportionation are the $Al_4(P^tBu_2)_6$, $Al_8Br_8(P^tBu_2)_6$, and $Al_2(P^tBu_2)_4$ clusters reported by Henke et al.[10,14,19] Based on these results, it seems as though dialkylphosphides stabilize low-valent aluminum compounds with oxidation states between +1 and +2 (for **7**, the average oxidation state is +1.33; for $Al_2(P^tBu_2)_4$ it is +2). More examples of aluminum phosphides are needed to better understand whether the apparent stabilization is a consequence of the electronic nature of phosphide ligands or a result of their steric requirements, though the tendency of aluminum phosphides to form small aluminum clusters should be noted.

The nature of aluminum-ligand interactions can be extended beyond that of just phosphorous. In combining empirical evidence obtained during the course of this study with reported compounds in the literature, we have observed an interesting trend in low-valent aluminum amide chemistry – the only crystalline aluminum amide compounds produced in our laboratory and reported in the literature contain nitrogen-silicon bonds. Future studies with varied nitrogenous ligands may provide insight into this apparent phenomenon, and may prove to be a crucial step in forming low-valent aluminum amidinate compounds.

There is significant interest in aluminum cluster compounds for applications as energetic materials. The oxidation of aluminum is highly exothermic ($2\ Al + 3/2\ O_2 \rightarrow Al_2O_3$; $\Delta H = -1676\ kJ\ mol^{-1}\ Al_2O_3$). While the thermodynamic energy content in aluminum metal is very high, the kinetics of combustion are slow due to the presence of an ever-present aluminum oxide surface layer. A number of techniques to form and

passivate aluminum nanoparticles have been attempted to date, though none have been found to work particularly well. A number of methods involving passivation of aluminum nanoparticles with perfluoro-fatty acids have been published, through the stability of such compounds may be an issue.[153] Large metalloid clusters are on the same dimensional scale as small nanoparticles and are kinetically passivated by an outer shell of ligands. As such, metalloid aluminum clusters are particularly well-suited for testing as energetic materials.

Ab-initio calculations on the $Al_{50}Cp^*_{12}$ metalloid cluster have shown an extremely high heat of combustion (11.5 kcal/cm^3), over three times that of conventional explosives such as RDX.[154] Metalloid aluminum cluster compounds are of particular interest in this field due to their low oxidation state and high theoretical heats of combustion. Formation of metalloid aluminum clusters in conjunction with energetic anionic ligands may yield particularly high-energy species.

Aluminum-containing compounds also have important roles in catalytic processes. Methylaluminoxane $(Al(CH3)_xO_y)_n$ is a polymeric oxide of trimethylaluminum that is commonly used as part of the Ziegler-Natta olefin polymerization process. This ill-defined white solid has been found to be essential in increasing the efficiency of the polymerization process. Raney Nickel is an aluminum/nickel alloy that is commonly used as a hydrogenation catalyst for olefin reduction. Like methylaluminoxane, the chemical identity of Raney Nickel is not well-defined. Both of these compounds are used in industrial processes and demonstrate the catalytic potential for aluminum-containing compounds.

Reduced oxidation state intermediates are quite common in catalytic processes; it is quite possible that metalloid aluminum clusters may have useful catalytic activity. The catalytic properties of low-valent aluminum compounds are almost totally unknown and may prove to be quite intriguing. In particular, mixed-valent aluminum clusters such as **7** and **8** may exhibit activity as catalysts or additives. It has been shown that low-valent Group 14 compounds exhibit unusual reactivity;[155] it may be possible that similarly surprising reactions occur at low-valent aluminum centers.

5.1: Contributions of this study.

Using the solutions generated by our reactor, two novel Al_3 clusters ($Li_2[Al_3(PPh_2)_6]$•2 Et_2O **7** and $Li_2[Al_3(PCy_2)_6]$•2 Et_2O **8**) with strikingly similar core architectures have been successfully prepared by the reaction between AlCl•Et2O and lithium dialkylphosphides. The resulting Al_3 clusters were characterized in the solid state (single-crystal X-ray diffraction, EPR) and in solution (^{1}H NMR). These two compounds are the third and fourth examples of Al_3 clusters reported in the literature and were found to be paramagnetic. In addition to measurements taken via solid-state EPR spectroscopy, the paramagnetic nature of these compounds was explored by solution NMR techniques previously not employed to characterize reduced-state aluminum compounds. The electronic structure of the model $[Al_3H_6]^{2-}$ cluster was calculated using DFT methods in order to gain further insight into the electronic structure of the Al_3 core in **7**.

Compounds containing aluminum in the +1.33 oxidation state are not well-known; only one other example an aluminum compound with average oxidation state +1.33 has been reported in the literature, namely the paramagnetic $(^tBu_3Si)_4Al_3$ cluster reported by Wiberg et al.[11] In addition to $(^tBu_3Si)_4Al_3$ there has only been one other Al_3

cluster reported in the literature: Power's $Na_2[AlAr"]_3$.[4] The discovery of Al_3 clusters **7** and **8** provides a third Al_3 cluster topology: the paramagnetic $[Al_3R_6]^{2-}$ architecture. In addition to having a novel architecture, clusters **7** and **8** have the lowest oxidation state of all aluminum phosphide compounds reported to date.

During the course of this study, the largest metalloid aluminum cluster $[Al_{77}(NTMS)_{20}]^{2-}$ **1** has been reproduced multiple times from the reaction of $LiNTMS_2$ with metastable $AlCl{\bullet}Et_2O$. The synthesis of **1** from $AlCl{\bullet}Et_2O$ demonstrates the potential to synthesize identical cluster compounds from differing precursor solutions – a significant step in increasing the reproducibility of metalloid cluster synthesis. The successful synthesis of **1** from both $AlCl{\bullet}Et_2O$ and $AlI{\bullet}Et_2O$ is an especially promising result, which suggests an inherent stability of the $[Al_{77}(NTMS_2)_{20}]^{2-}$ metalloid cluster. In addition to **1**, **7**, and **8**, the $[Ga_{22}Br_{12}(NTMS_2)_{10}]^{2-}$ cluster **2** and novel aluminum (III) amidinates **3**, **4**, and **5** were synthesized and characterized during this study.

Appendix A. Metal Halide Co-condensation Reactor Parts List.

HX-tank-to-reactor connections (*italicized items doubled*, supplier in parentheses)

- HCl and HBr lecture bottles, 0.5 and 1.0 lb respectively (Airgas East) **NOTE:** when connected to regulators, tanks must be stored vertically due to presence of pressurized HX liquid in tanks
- *Stainless steel regulators* (Lecture Bottle SS 3000PSI, 015 Del Range, CGA 180 – Airgas East)
- *¼" NPT-to-1/4" SS tube adapter exiting regulator*
- *¼" SS tubing, bent, to ¼" SS Union Tee* (Union tee to ¼" tubing to ¼" half-turn stop valve, connected to argon tank)
- *¼" SS tubing to ¼" tubing-to-VCR fitting adapter, connected via self-centering VCR ring to STEC-4400 MFC*
- *MFC connected to ¼" SS tubing via self-centering ring and VCR-to-KF25 adapter (Ideal Vacuum)*
- Half-turn ¼" SS tubing stopper connected in-line to delivery tubing with ¼" tubing elbow and KF25 terminus (Swagelok)
- KF25-to-Male ½" NPT connected to reactor base plate (Ideal Vacuum)
- ½" NPT-to-1/4" Ultratorr connection on top of base plate, to S-tube, connected to quartz tube via 3/8" Ultratorr (Swagelok)

Argon tank-to-reactor connections (*italicized items doubled*)

- Gas regulator, 3000PSI to 3/8" tubing to ¼" tubing
- *¼" tubing to ¼" tubed Union Cross*
- *¼" tubing via ¼" elbow connected to ¼" tubing to ¼" half-turn stop valve*
- ¼ tubing to brass bellows valve, connected to ½" male NPT to base plate

Solvent addition flask-to-tank connections

- 350 mL solvent addition flask with Teflon stopcock and male 24/40 ground glass drip joint greased with Apiezon T grease (Chemglass)
- 250 mL two-neck round bottom flask (Chemglass)
- 250 mL round bottom flask heating mantle connected to 12A variac via three-way electrical splitter (VWR)
- Stainless steel 24/40 taper joint greased with Apiezon T grease welded to ¼" SS tubing connected to brass bellows valve (Quark, welding by JHU)
- ¼" SS tubing welded to KF25 connection, connected to KF25-to-1/2" male NPT adapter attached to base plate (Ideal Vacuum, welding by UMD)
- ¼" SS tube/solvent inlet wand connected to inlet via ultratorr connection (JHU)

Solution collection:

- 250 mL solvent receiving flask with glass J Young valve connected to SS drain spigot tapered to 14/20 joint, greased with Apiezon N low-T grease (Quark Glass)
- Spigot connected internally to trough inside bell jar with 7° decline angle (machined and welded to drain tube at UMD)

Internal assembly:

- Threaded rods screwed into base plate, sheathed in SS tube to support cooling water can (Lesker)
- Cooling water jacket, supported on rods, secured with washers and hex nuts. Water inlet and outlet via bent ¼" SS tubes connected to Ultratorr connections. (JHU)
- Tantalum heat shield supported by four slotted tantalum rods. Rods secured on alumina disc with tantalum bolts above and below disc. (Thermo Shield)
- Tungsten heating element connected to bottom tantalum element, wrapped around alumina tube and fixed on top of furnace assembly (resistance: 4-6 Ohm) (Midwest Tungsten Service, Inc., Willowbrook, IL)
- Alumina disc, machined with ten holes. Eight at 2.0" apart, two at 1.8", center-to-center. Center hole of 3/8". (IHDIV)
- Tantalum rods connecting to either end of heating element. (JHU)
- Tungsten rod connecting electrical connection to top of furnace, covered by ceramic beads (A.D. Mackay))
- Tantalum screws, washers, furnace pieces (Thermo Shield, Los Altos, CA)
- Threaded ceramic tube, silica 33 OD, 25 ID, 108mm length (Friatec N.A., Odessa, FL)

Feed-throughs in baseplate:

- Baseplate (Lesker)
- KF25-to-1/4" Ultratorr for HX inlet (Ideal Vacuum)
- KF25-to-1/4" Ultratorr for solvent inlet (Ideal Vacuum)
- ½" male NPT-to-1/4" ultratorr for water inlet (Swagelok)
- ½" male NPT-to-1/4" ultratorr for water outlet (Swagelok)
- ½" male-NPT rough vacuum gauge under baseplate (Swagelok)
- ½" male-NPT-to ¼" Swagelok tube for argon inlet (Ideal Vacuum)
- Electrical feedthrough, sealed ceramic disc for current introduction (MPF Products, Gray Court, SC)
- Electrical feedthrough for 2 K-type thermocouples, sealed ceramic disc (Lesker)
- 3 x ½" male NPT caps (Lesker)

Diffusion pump:

- Edwards Diffstak 160 diffusion pump
- Santovac-5, 250 mL
- *Edwards Diffstak O-ring*

Mechanical Pump:

- Welch Duoseal 1397 mechanical pump
- Welded foreline pipe (MDC Vacuum products)
- *Edwards KF25 Speedivalve*

Reactor Chamber:

- 30L Stainless Steel Bell Jar with internal trough at 7 degree slope (Lesker)
- KF16 cap (Lesker)
- KF16 o-ring and centering piece (Ideal Vacuum)
- KF16 clamp (Ideal Vacuum)
- Mica band heater (Thermal Devices, Mount Airy, MD)

Pressure monitoring:

- *Thermocouple pressure gauge, Varian 801* (Lesker)
- *Thermocouple pressure gauge controller, Varian 801* (Lesker)
- Model 531 Ion Gauge (Lesker)
- Ion Gauge Controller (Lesker)

Solvent distillation setup:

- 1 L two- or three-neck round bottom flask with solvent (toluene, diethyl ether or THF) over sodium benzophenone ketyl radical
- Flask connected to 500 mL reservoir distillation head (Chemglass)
- Freshly distilled solvent transferred via Teflon cannula to flat-bottom 1 L flask containing activated molecular sieves

Graphite furnace:

- One 3.28” × 0.938 O.D. graphite tube fused to a 3/8” quartz tube (SICJHOVEN, GMSI Graphite Specialists, Tempe, AZ)
- Six graphite inserts, 0.625” diameter (SICJHINSERT, GMSI)

Variac:

- Mastech 5KVA 0-250V, 20A variac

Appendix B. Crystal Structure Report for $Li_2[Al_3(PPh_2)_6]$•2 Et_2O (UM2157)

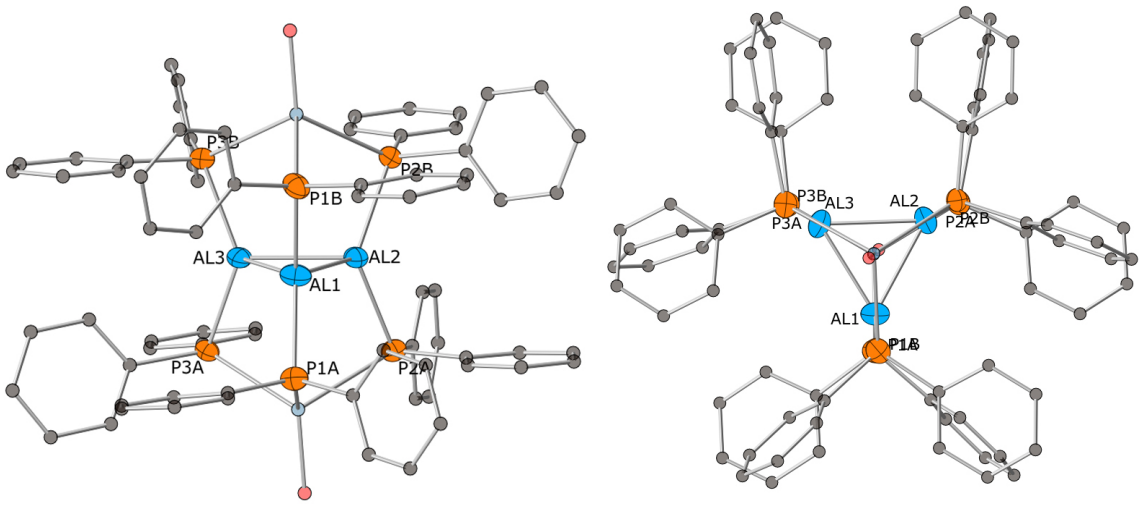

Figure B4: X-ray crystal structure of $Li_2[Al_3(PPh_2)_6]$•2 Et_2O viewed along C_2 (left) and C_3 (right) axes. Aluminum and phosphorous atoms are labeled. Blue = Al, orange = P, light blue = Li, red = O, black = C. Thermal ellipsoids are shown at 50% probability, disordered carbon atoms in Et_2O and all hydrogens omitted for clarity.

A orange prism-like specimen of $C_{87}H_{88}Al_3Li_2O_2P_6$, approximate dimensions 0.22 mm × 0.28 mm × 0.38 mm, was used for the X-ray crystallographic analysis. The X-ray intensity data were measured on a Bruker Smart Apex2, CCD system equipped with a graphite monochromator and a MoKα fine focus sealed tube (λ = 0.71073 Å). Data collection temperature was 80 K.

The total exposure time was 22.75 hours. The frames were integrated with the Bruker SAINT software package using a narrow-frame algorithm. The integration of the data using a triclinic unit cell yielded a total of 27162 reflections to a maximum θ angle of 28.00° (0.76 Å resolution), of which 9586 were independent (average redundancy 2.834, completeness = 99.3%, R_{int} = 2.55%, R_{sig} = 3.07%) and 7555 (78.81%) were greater than $2\sigma(F^2)$. The final cell constants of *a* = 12.8213(10) Å, *b* = 13.7634(11) Å, *c* = 13.9032(11) Å, α = 95.5268(13)°, β = 107.2191(12)°, γ = 117.4940(12)°, *V* = 1998.7(3) $Å^3$, are based upon the

refinement of the XYZ-centroids of 8032 reflections above 20 σ(I) with 4.464° < 2θ < 57.99°. Data were corrected for absorption effects using the multi-scan method (SADABS). The calculated minimum and maximum transmission coefficients (based on crystal size) are 0.8720 and 0.9540.

The structure was solved and refined using the Bruker SHELXTL Software Package, using the space group P-1, with Z = 1 for the formula unit, $C_{87}H_{88}Al_3Li_2O_2P_6$. The final anisotropic full-matrix least-squares refinement on F^2 with 903 variables converged at R_1 = 7.22%, for the observed data and wR_2 = 14.62% for all data. The goodness-of-fit was 1.000. The largest peak in the final difference electron density synthesis was 0.244 $e^-/Å^3$ and the largest hole was -0.512 $e^-/Å^3$ with an RMS deviation of 0.047 $e^-/Å^3$. On the basis of the final model, the calculated density was 1.202 g/cm^3 and F(000), 761 e^-.

APEX2 Version 2010.11-3 (Bruker AXS Inc.)

SAINT Version 7.68A (Bruker AXS Inc., 2009)

SADABS Version 2008/1 (G. M. Sheldrick, Bruker AXS Inc.)

XPREP Version 2008/2 (G. M. Sheldrick, Bruker AXS Inc.)

XS Version 2008/1 (G. M. Sheldrick, *Acta Cryst.* (2008). A**64**, 112-122)

XL Version 2008/4 (G. M. Sheldrick, *Acta Cryst.* (2008). A**64**, 112-122)

Platon (A. L. Spek, *Acta Cryst.* (1990). A**46**, C-34)

Table B1: Sample and crystal data for UM2157.

Identification code	2157
Chemical formula	$C_{87}H_{88}Al_3Li_2O_2P_6$

Formula weight	1446.21	
Temperature	80(2) K	
Wavelength	0.71073 Å	
Crystal size	0.22 × 0.28 × 0.38 mm	
Crystal habit	orange prism	
Crystal system	triclinic	
Space group	P -1	
Unit cell dimensions	a = 12.8213(10) Å	α = 95.5268(13)°
	b = 13.7634(11) Å	β = 107.2191(12)°
	c = 13.9032(11) Å	γ = 117.4940(12)°
Volume	1998.7(3) $Å^3$	
Z	1	
Density (calculated)	1.202 Mg/cm^3	
Absorption coefficient	0.214 mm^{-1}	
F(000)	761	

Table B2. Data collection and structure refinement for UM2157.

Diffractometer	Bruker Smart Apex2, CCD
Radiation source	fine focus sealed tube, MoKα
Theta range for data collection	2.23 to 28.00°
Index ranges	$-16 \leq h \leq 16$, $-18 \leq k \leq 18$, $-18 \leq l \leq 18$
Reflections collected	27162
Independent reflections	9586 [R(int) = 0.0255]

Coverage of independent reflections	99.3%	
Absorption correction	multi-scan	
Max. and min. transmission	0.9540 and 0.8720	
Structure solution technique	direct methods	
Structure solution program	SHELXS-97 (Sheldrick, 2008)	
Refinement method	Full-matrix least-squares on F^2	
Refinement program	SHELXL-97 (Sheldrick, 2008)	
Function minimized	$\Sigma\, w(F_o^2 - F_c^2)^2$	
Data / restraints / parameters	9586 / 692 / 903	
Goodness-of-fit on F^2	1.000	
Final R indices	7555 data; I>2σ(I)	$R_1 = 0.0722$, $wR_2 = 0.1407$
	all data	$R_1 = 0.0897$, $wR_2 = 0.1462$
Weighting scheme	$w=1/[\sigma^2(F_o^2)+(0.01P)^2+3.18P]$, $P=(\max(F_o^2,0)+2F_c^2)/3$	
Largest diff. peak and hole	0.244 and -0.512 eÅ^{-3}	
R.M.S. deviation from mean	0.047 eÅ^{-3}	

$R_{int} = \Sigma|F_o^2 - F_o^2(\text{mean})| / \Sigma[F_o^2]$ $\quad R_1 = \Sigma||F_o| - |F_c|| / \Sigma|F_o|$

$\text{GOF} = S = \{\Sigma[w(F_o^2 - F_c^2)^2] / (n - p)\}^{1/2}$ $\quad wR_2 = \{\Sigma[w(F_o^2 - F_c^2)^2] / \Sigma[w(F_o^2)^2]\}^{1/2}$

Table B3. Bond lengths (Å) for UM2157.

Al1-P1A	2.3674(18)	Al1-P1B	2.3674(18)
Al1-Al3	2.617(2)	Al1-Al2	2.626(2)
Al2-P2B	2.3686(17)	Al2-P2A	2.3789(17)
Al2-Al3	2.6330(19)	Al3-P3A	2.3682(16)
Al3-P3B	2.3696(17)	P1A-C11A	1.826(5)
P1A-C21A	1.835(4)	P1A-Li1#1	2.646(5)

C11A-C16A	1.391(5)	C11A-C12A	1.394(5)
C12A-C13A	1.376(6)	C12A-H12A	0.95
C13A-C14A	1.371(6)	C13A-H13A	0.95
C14A-C15A	1.373(5)	C14A-H14A	0.95
C15A-C16A	1.398(6)	C15A-H15A	0.95
C16A-H16A	0.95	C21A-C26A	1.389(5)
C21A-C22A	1.396(4)	C22A-C23A	1.373(6)
C22A-H22A	0.95	C23A-C24A	1.372(6)
C23A-H23A	0.95	C24A-C25A	1.375(5)
C24A-H24A	0.95	C25A-C26A	1.393(6)
C25A-H25A	0.95	C26A-H26A	0.95
P2A-C31A	1.826(6)	P2A-C41A	1.838(4)
P2A-Li1#1	2.702(5)	C31A-C36A	1.394(7)
C31A-C32A	1.399(6)	C32A-C33A	1.380(7)
C32A-H32A	0.95	C33A-C34A	1.374(9)
C33A-H33A	0.95	C34A-C35A	1.378(7)
C34A-H34A	0.95	C35A-C36A	1.406(8)
C35A-H35A	0.95	C36A-H36A	0.95
C41A-C46A	1.387(6)	C41A-C42A	1.398(5)
C42A-C43A	1.373(7)	C42A-H42A	0.95
C43A-C44A	1.379(7)	C43A-H43A	0.95
C44A-C45A	1.381(6)	C44A-H44A	0.95
C45A-C46A	1.385(7)	C45A-H45A	0.95
C46A-H46A	0.95	P3A-C51A	1.832(5)

P3A-C61A	1.837(4)	P3A-Li1#1	2.677(5)
C51A-C56A	1.391(6)	C51A-C52A	1.396(6)
C52A-C53A	1.382(6)	C52A-H52A	0.95
C53A-C54A	1.371(8)	C53A-H53A	0.95
C54A-C55A	1.375(6)	C54A-H54A	0.95
C55A-C56A	1.401(7)	C55A-H55A	0.95
C56A-H56A	0.95	C61A-C66A	1.385(5)
C61A-C62A	1.395(5)	C62A-C63A	1.379(8)
C62A-H62A	0.95	C63A-C64A	1.386(7)
C63A-H63A	0.95	C64A-C65A	1.383(7)
C64A-H64A	0.95	C65A-C66A	1.386(8)
C65A-H65A	0.95	C66A-H66A	0.95
P1B-C11B	1.831(5)	P1B-C21B	1.835(4)
P1B-Li1	2.689(5)	C11B-C16B	1.392(6)
C11B-C12B	1.396(6)	C12B-C13B	1.379(7)
C12B-H12B	0.95	C13B-C14B	1.374(8)
C13B-H13B	0.95	C14B-C15B	1.378(7)
C14B-H14B	0.95	C15B-C16B	1.399(8)
C15B-H15B	0.95	C16B-H16B	0.95
C21B-C26B	1.387(6)	C21B-C22B	1.395(5)
C22B-C23B	1.372(7)	C22B-H22B	0.95
C23B-C24B	1.378(7)	C23B-H23B	0.95
C24B-C25B	1.378(6)	C24B-H24B	0.95
C25B-C26B	1.384(7)	C25B-H25B	0.95

C26B-H26B	0.95	P2B-C31B	1.835(5)
P2B-C41B	1.838(4)	P2B-Li1	2.720(5)
C31B-C36B	1.394(6)	C31B-C32B	1.397(6)
C32B-C33B	1.379(7)	C32B-H32B	0.95
C33B-C34B	1.379(8)	C33B-H33B	0.95
C34B-C35B	1.376(7)	C34B-H34B	0.95
C35B-C36B	1.399(7)	C35B-H35B	0.95
C36B-H36B	0.95	C41B-C42B	1.392(5)
C41B-C46B	1.393(5)	C42B-C43B	1.378(8)
C42B-H42B	0.95	C43B-C44B	1.386(7)
C43B-H43B	0.95	C44B-C45B	1.384(6)
C44B-H44B	0.95	C45B-C46B	1.384(8)
C45B-H45B	0.95	C46B-H46B	0.95
P3B-C51B	1.827(6)	P3B-C61B	1.833(4)
P3B-Li1	2.788(5)	C51B-C56B	1.394(7)
C51B-C52B	1.395(6)	C52B-C53B	1.378(7)
C52B-H52B	0.95	C53B-C54B	1.376(9)
C53B-H53B	0.95	C54B-C55B	1.380(7)
C54B-H54B	0.95	C55B-C56B	1.405(8)
C55B-H55B	0.95	C56B-H56B	0.95
C61B-C66B	1.386(6)	C61B-C62B	1.396(5)
C62B-C63B	1.372(7)	C62B-H62B	0.95
C63B-C64B	1.377(7)	C63B-H63B	0.95
C64B-C65B	1.383(6)	C64B-H64B	0.95

C65B-C66B	1.385(7)	C65B-H65B	0.95
C66B-H66B	0.95	C1-C2	1.51(3)
C1-H1A	0.98	C1-H1B	0.98
C1-H1C	0.98	C2-C3	1.39
C2-C7	1.39	C3-C4	1.39
C3-H3	0.95	C4-C5	1.39
C4-H4	0.95	C5-C6	1.39
C5-H5	0.95	C6-C7	1.39
C6-H6	0.95	C7-H7	0.95
Li1-O1X	1.926(8)	Li1-O1Y	1.926(12)
Li1-P1A#1	2.646(5)	Li1-P3A#1	2.677(5)
Li1-P2A#1	2.702(5)		

Symmetry transformations used to generate equivalent atoms: #1 -x+2, -y+1, -z+1

Table B4. Bond angles (°) for UM2157.

P1A-Al1-P1B	134.40(8)	P1A-Al1-Al3	109.28(7)
P1B-Al1-Al3	110.09(7)	P1A-Al1-Al2	109.89(7)
P1B-Al1-Al2	109.04(7)	Al3-Al1-Al2	60.29(6)
P2B-Al2-P2A	134.14(7)	P2B-Al2-Al1	109.81(6)
P2A-Al2-Al1	109.27(7)	P2B-Al2-Al3	109.27(6)
P2A-Al2-Al3	110.66(6)	Al1-Al2-Al3	59.68(6)
P3A-Al3-P3B	133.52(7)	P3A-Al3-Al1	109.84(7)
P3B-Al3-Al1	111.00(7)	P3A-Al3-Al2	108.35(6)
P3B-Al3-Al2	110.66(6)	Al1-Al3-Al2	60.03(6)
C11A-P1A-C21A	101.6(2)	C11A-P1A-Al1	107.5(2)

C21A-P1A-Al1	109.60(16)	C11A-P1A-Li1#1	120.2(2)
C21A-P1A-Li1#1	124.32(19)	Al1-P1A-Li1#1	92.18(10)
C16A-C11A-C12A	118.2(5)	C16A-C11A-P1A	123.4(4)
C12A-C11A-P1A	118.3(4)	C13A-C12A-C11A	121.3(5)
C13A-C12A-H12A	119.3	C11A-C12A-H12A	119.3
C14A-C13A-C12A	120.3(6)	C14A-C13A-H13A	119.8
C12A-C13A-H13A	119.8	C13A-C14A-C15A	119.4(6)
C13A-C14A-H14A	120.3	C15A-C14A-H14A	120.3
C14A-C15A-C16A	121.1(6)	C14A-C15A-H15A	119.5
C16A-C15A-H15A	119.5	C11A-C16A-C15A	119.6(5)
C11A-C16A-H16A	120.2	C15A-C16A-H16A	120.2
C26A-C21A-C22A	117.7(4)	C26A-C21A-P1A	121.9(4)
C22A-C21A-P1A	120.4(4)	C23A-C22A-C21A	121.6(5)
C23A-C22A-H22A	119.2	C21A-C22A-H22A	119.2
C24A-C23A-C22A	120.3(6)	C24A-C23A-H23A	119.9
C22A-C23A-H23A	119.9	C23A-C24A-C25A	119.0(6)
C23A-C24A-H24A	120.5	C25A-C24A-H24A	120.5
C24A-C25A-C26A	121.2(6)	C24A-C25A-H25A	119.4
C26A-C25A-H25A	119.4	C21A-C26A-C25A	119.9(5)
C21A-C26A-H26A	120.1	C25A-C26A-H26A	120.1
C31A-P2A-C41A	103.1(3)	C31A-P2A-Al2	104.7(5)
C41A-P2A-Al2	110.56(14)	C31A-P2A-Li1#1	121.2(4)
C41A-P2A-Li1#1	123.61(18)	Al2-P2A-Li1#1	91.16(10)
C36A-C31A-C32A	118.0(6)	C36A-C31A-P2A	123.8(6)

C32A-C31A-P2A	118.1(6)	C33A-C32A-C31A	121.2(8)
C33A-C32A-H32A	119.4	C31A-C32A-H32A	119.4
C34A-C33A-C32A	120.8(8)	C34A-C33A-H33A	119.6
C32A-C33A-H33A	119.6	C33A-C34A-C35A	119.1(9)
C33A-C34A-H34A	120.5	C35A-C34A-H34A	120.5
C34A-C35A-C36A	120.9(9)	C34A-C35A-H35A	119.6
C36A-C35A-H35A	119.6	C31A-C36A-C35A	119.9(7)
C31A-C36A-H36A	120.1	C35A-C36A-H36A	120.1
C46A-C41A-C42A	117.6(4)	C46A-C41A-P2A	123.1(4)
C42A-C41A-P2A	119.4(4)	C43A-C42A-C41A	120.8(6)
C43A-C42A-H42A	119.6	C41A-C42A-H42A	119.6
C42A-C43A-C44A	121.1(7)	C42A-C43A-H43A	119.4
C44A-C43A-H43A	119.4	C43A-C44A-C45A	118.9(7)
C43A-C44A-H44A	120.5	C45A-C44A-H44A	120.5
C44A-C45A-C46A	120.2(7)	C44A-C45A-H45A	119.9
C46A-C45A-H45A	119.9	C45A-C46A-C41A	121.4(6)
C45A-C46A-H46A	119.3	C41A-C46A-H46A	119.3
C51A-P3A-C61A	102.6(2)	C51A-P3A-Al3	108.74(19)
C61A-P3A-Al3	110.52(13)	C51A-P3A-Li1#1	119.4(2)
C61A-P3A-Li1#1	122.50(17)	Al3-P3A-Li1#1	92.22(10)
C56A-C51A-C52A	117.7(5)	C56A-C51A-P3A	124.1(4)
C52A-C51A-P3A	118.2(4)	C53A-C52A-C51A	122.0(6)
C53A-C52A-H52A	119.0	C51A-C52A-H52A	119.0
C54A-C53A-C52A	119.9(6)	C54A-C53A-H53A	120.1

C52A-C53A-H53A	120.1	C53A-C54A-C55A	119.4(7)
C53A-C54A-H54A	120.3	C55A-C54A-H54A	120.3
C54A-C55A-C56A	121.2(7)	C54A-C55A-H55A	119.4
C56A-C55A-H55A	119.4	C51A-C56A-C55A	119.7(5)
C51A-C56A-H56A	120.1	C55A-C56A-H56A	120.1
C66A-C61A-C62A	118.0(4)	C66A-C61A-P3A	122.4(3)
C62A-C61A-P3A	119.6(3)	C63A-C62A-C61A	121.0(5)
C63A-C62A-H62A	119.5	C61A-C62A-H62A	119.5
C62A-C63A-C64A	120.6(7)	C62A-C63A-H63A	119.7
C64A-C63A-H63A	119.7	C65A-C64A-C63A	118.9(7)
C65A-C64A-H64A	120.6	C63A-C64A-H64A	120.6
C64A-C65A-C66A	120.5(7)	C64A-C65A-H65A	119.8
C66A-C65A-H65A	119.8	C61A-C66A-C65A	121.1(5)
C61A-C66A-H66A	119.5	C65A-C66A-H66A	119.5
C11B-P1B-C21B	102.4(3)	C11B-P1B-Al1	110.0(2)
C21B-P1B-Al1	111.55(15)	C11B-P1B-Li1	118.3(2)
C21B-P1B-Li1	120.6(2)	Al1-P1B-Li1	93.76(11)
C16B-C11B-C12B	117.6(5)	C16B-C11B-P1B	123.8(5)
C12B-C11B-P1B	118.6(5)	C13B-C12B-C11B	121.0(6)
C13B-C12B-H12B	119.5	C11B-C12B-H12B	119.5
C14B-C13B-C12B	120.9(6)	C14B-C13B-H13B	119.6
C12B-C13B-H13B	119.6	C13B-C14B-C15B	119.5(8)
C13B-C14B-H14B	120.2	C15B-C14B-H14B	120.2
C14B-C15B-C16B	119.8(7)	C14B-C15B-H15B	120.1

C16B-C15B-H15B	120.1	C11B-C16B-C15B	121.1(5)
C11B-C16B-H16B	119.4	C15B-C16B-H16B	119.4
C26B-C21B-C22B	117.5(5)	C26B-C21B-P1B	123.0(4)
C22B-C21B-P1B	119.5(4)	C23B-C22B-C21B	121.6(6)
C23B-C22B-H22B	119.2	C21B-C22B-H22B	119.2
C22B-C23B-C24B	120.1(7)	C22B-C23B-H23B	119.9
C24B-C23B-H23B	119.9	C23B-C24B-C25B	119.4(7)
C23B-C24B-H24B	120.3	C25B-C24B-H24B	120.3
C24B-C25B-C26B	120.3(7)	C24B-C25B-H25B	119.8
C26B-C25B-H25B	119.8	C25B-C26B-C21B	121.0(6)
C25B-C26B-H26B	119.5	C21B-C26B-H26B	119.5
C31B-P2B-C41B	102.3(2)	C31B-P2B-Al2	108.6(2)
C41B-P2B-Al2	111.80(13)	C31B-P2B-Li1	120.2(2)
C41B-P2B-Li1	119.98(17)	Al2-P2B-Li1	93.47(10)
C36B-C31B-C32B	117.3(5)	C36B-C31B-P2B	124.4(5)
C32B-C31B-P2B	118.2(5)	C33B-C32B-C31B	121.5(6)
C33B-C32B-H32B	119.2	C31B-C32B-H32B	119.2
C34B-C33B-C32B	120.6(6)	C34B-C33B-H33B	119.7
C32B-C33B-H33B	119.7	C35B-C34B-C33B	119.3(7)
C35B-C34B-H34B	120.4	C33B-C34B-H34B	120.4
C34B-C35B-C36B	120.4(7)	C34B-C35B-H35B	119.8
C36B-C35B-H35B	119.8	C31B-C36B-C35B	120.8(6)
C31B-C36B-H36B	119.6	C35B-C36B-H36B	119.6
C42B-C41B-C46B	117.9(4)	C42B-C41B-P2B	119.3(3)

C46B-C41B-P2B	122.7(3)	C43B-C42B-C41B	121.4(5)
C43B-C42B-H42B	119.3	C41B-C42B-H42B	119.3
C42B-C43B-C44B	120.0(7)	C42B-C43B-H43B	120.0
C44B-C43B-H43B	120.0	C45B-C44B-C43B	119.4(7)
C45B-C44B-H44B	120.3	C43B-C44B-H44B	120.3
C44B-C45B-C46B	120.4(6)	C44B-C45B-H45B	119.8
C46B-C45B-H45B	119.8	C45B-C46B-C41B	120.8(5)
C45B-C46B-H46B	119.6	C41B-C46B-H46B	119.6
C51B-P3B-C61B	102.7(3)	C51B-P3B-Al3	106.0(6)
C61B-P3B-Al3	108.86(15)	C51B-P3B-Li1	122.2(4)
C61B-P3B-Li1	122.96(18)	Al3-P3B-Li1	91.79(10)
C56B-C51B-C52B	117.6(7)	C56B-C51B-P3B	123.6(6)
C52B-C51B-P3B	118.7(6)	C53B-C52B-C51B	121.5(7)
C53B-C52B-H52B	119.3	C51B-C52B-H52B	119.3
C54B-C53B-C52B	120.8(8)	C54B-C53B-H53B	119.6
C52B-C53B-H53B	119.6	C53B-C54B-C55B	119.0(9)
C53B-C54B-H54B	120.5	C55B-C54B-H54B	120.5
C54B-C55B-C56B	120.5(9)	C54B-C55B-H55B	119.8
C56B-C55B-H55B	119.8	C51B-C56B-C55B	120.5(7)
C51B-C56B-H56B	119.8	C55B-C56B-H56B	119.8
C66B-C61B-C62B	117.1(5)	C66B-C61B-P3B	121.9(4)
C62B-C61B-P3B	120.9(3)	C63B-C62B-C61B	121.3(5)
C63B-C62B-H62B	119.3	C61B-C62B-H62B	119.3
C62B-C63B-C64B	121.1(6)	C62B-C63B-H63B	119.5

C64B-C63B-H63B	119.5	C63B-C64B-C65B	118.4(6)
C63B-C64B-H64B	120.8	C65B-C64B-H64B	120.8
C64B-C65B-C66B	120.5(6)	C64B-C65B-H65B	119.8
C66B-C65B-H65B	119.8	C65B-C66B-C61B	121.5(6)
C65B-C66B-H66B	119.2	C61B-C66B-H66B	119.2
C2-C1-H1A	109.5	C2-C1-H1B	109.5
H1A-C1-H1B	109.5	C2-C1-H1C	109.5
H1A-C1-H1C	109.5	H1B-C1-H1C	109.5
C3-C2-C7	120.0	C3-C2-C1	120.3(4)
C7-C2-C1	119.7(4)	C4-C3-C2	120.0
C4-C3-H3	120.0	C2-C3-H3	120.0
C3-C4-C5	120.0	C3-C4-H4	120.0
C5-C4-H4	120.0	C6-C5-C4	120.0
C6-C5-H5	120.0	C4-C5-H5	120.0
C7-C6-C5	120.0	C7-C6-H6	120.0
C5-C6-H6	120.0	C6-C7-C2	120.0
C6-C7-H7	120.0	C2-C7-H7	120.0
O1X-Li1-P1A#1	118.3(4)	O1Y-Li1-P1A#1	117.5(5)
O1X-Li1-P3A#1	116.0(3)	O1Y-Li1-P3A#1	102.5(4)
P1A#1-Li1-P3A#1	104.29(15)	O1X-Li1-P1B	113.2(4)
O1Y-Li1-P1B	112.5(5)	P1A#1-Li1-P1B	128.42(16)
P3A#1-Li1-P1B	51.55(9)	O1X-Li1-P2A#1	109.2(3)
O1Y-Li1-P2A#1	122.7(4)	P1A#1-Li1-P2A#1	104.08(15)
P3A#1-Li1-P2A#1	103.29(15)	P1B-Li1-P2A#1	54.87(9)

O1X-Li1-P2B	121.3(3)	O1Y-Li1-P2B	107.4(3)
P1A#1-Li1-P2B	51.94(9)	P3A#1-Li1-P2B	56.11(9)
P1B-Li1-P2B	101.95(14)	P2A#1-Li1-P2B	129.47(16)
O1X-Li1-P3B	114.2(3)	O1Y-Li1-P3B	128.0(4)
P1A#1-Li1-P3B	54.01(10)	P3A#1-Li1-P3B	129.49(16)
P1B-Li1-P3B	102.77(14)	P2A#1-Li1-P3B	53.79(9)
P2B-Li1-P3B	101.01(15)		

Symmetry transformations used to generate equivalent atoms: #1 -x+2, -y+1, -z+1

Table B5. Data collection details for UM2157.

Axis	**dx/mm**	**2θ/°**	**ω/°**	**φ/°**	**χ/°**	**Width/°**	**Frames**	**Time/s**
Omega	50.059	-31.50	328.50	90.00	54.71	-0.30	610	30.00
Omega	50.059	-31.50	328.50	210.00	54.71	-0.30	610	30.00
Omega	50.059	-31.50	328.50	330.00	54.71	-0.30	610	30.00
Phi	50.059	-31.50	148.50	0.00	54.71	-0.30	900	30.00

Appendix C. Synthesis and Solid-State Structure of Ga_2Br_4•2 $PHCy_2$.

During the course of this study, the Ga (II) dimer Ga_2Br_4•2 $PHCy_2$ (**C1**) was synthesized by the reaction of GaBr•THF with dicyclohexylphosphine in toluene.[137] The resulting colorless blocks were structurally characterized by x-ray crystallography. In the solid-state **C1** has virtual C_{2h} symmetry (see Figure **C1**) and crystallizes as yellow plates.

X-Ray Crystal Structure.

The solid-state structure of **C1** contains a Ga–Ga bond measuring 2.435(1) Å (see Figure **C1**). The Ga–Br bonds average 2.370(10) Å. The Ga–P bond is 2.415(3) Å and the P–C bonds 1.832(2) Å. The Ga–Ga bond has staggered conformation, with the two phosphine ligands arranged anti- to one another (P–Ga–Ga–P torsion angle = 180.0º). The average Br–Ga–P bond angle is 99.7 ± 1.7º. Complete crystallographic data for **C1** can be found in Table **C1**.

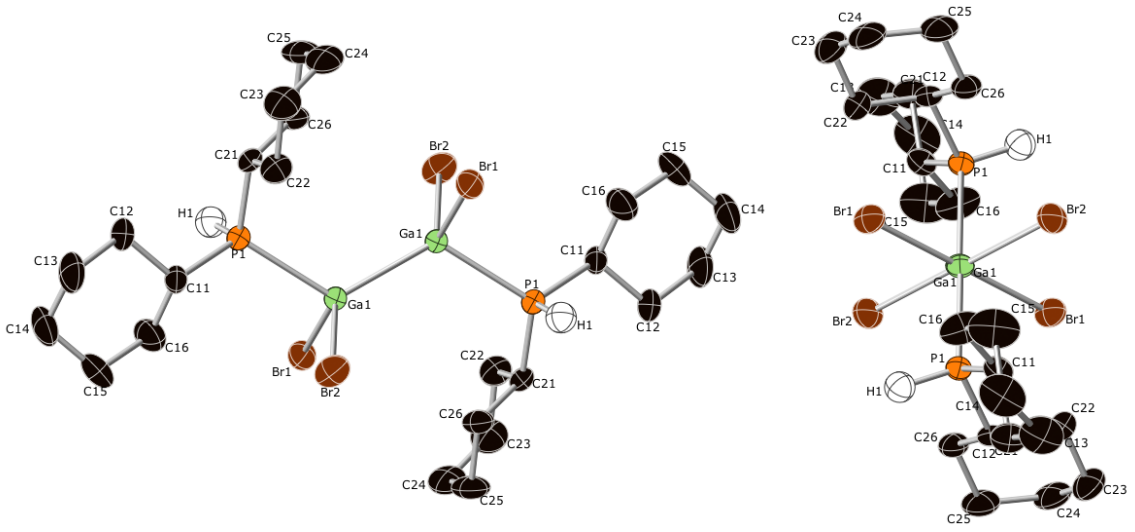

Figure C5: X-ray crystal structure of **C1** viewed from the side (left) and along the Ga–Ga bond axis (right). Gallium = green, bromine = brown, phosphorous = orange, carbon = black hydrogen = white. Thermal ellipsoids shown at 50% probability, hydrogen atoms except phosphine protons omitted for clarity.

Table C1: Crystallographic data for Ga_2Br_4•2$PHCy_2$.

Compound	$C_{24}H_{46}Br_4Ga_2P_2$	β (°)	109.177(2)
Formula Weight	855.63	γ (°)	90.00
Temperature (K)	150(2)	volume (Å^3)	1658.6(3)
Wavelength (Å)	0.71073	Z = 2	
Crystal system	Monoclinic	ab. coeff.,mm^{-1}	6.551
Space group	P -21n	final R indices	
Unit cell dimensions		R_1, I>2σ(I)	3.40%
a (Å)	9.6095(11)	wR_2, (all data)$_a$	6.80%
b (Å)	13.7083(16)	GOF	1.00
c (Å)	13.3305(16)		
α (º)	90.00		

$R_{int} = \Sigma|F_o^2 - F_o^2(\text{mean})| / \Sigma[F_o^2]$ $R_1 = \Sigma||F_o| - |F_c|| / \Sigma|F_o|$

GOF = S = $\{\Sigma[w(F_o^2 - F_c^2)^2] / (n - p)\}^{1/2}$ $wR_2 = \{\Sigma[w(F_o^2 - F_c^2)^2] / \Sigma[w(F_o^2)^2]\}^{1/2}$

NMR Spectroscopy.

In order to confirm the protonation state of the phosphorous atom solution NMR spectra of **C1** were taken. The solution ^{1}H spectrum (See Figure **C2**) of **C1** (C_6D_6) shows typical resonances for the four cyclohexyl groups from δ = 0.98–2.12 ppm. A widely-separated doublet of triplets is observed at δ = 4.10 ppm with coupling constants of 5 and 352 Hz. The small 5 Hz coupling constant is due to three-bond coupling of the P-bound proton to the methine proton on the cyclohexyl groups. The large 352 Hz coupling is indicative of one-bond P–H coupling. In the proton-coupled ^{31}P spectrum (Figure **C2**) the

only resonance is a doublet centered at –36.7 ppm (J = 352 Hz). The combination of ^{31}P and ^{1}H NMR spectra confirm the presence of the phosphine proton. These spectra are nearly identical to the reported spectra for the related Ga_2I_4•2 $PHCy_2$ compound **C2**.[34]

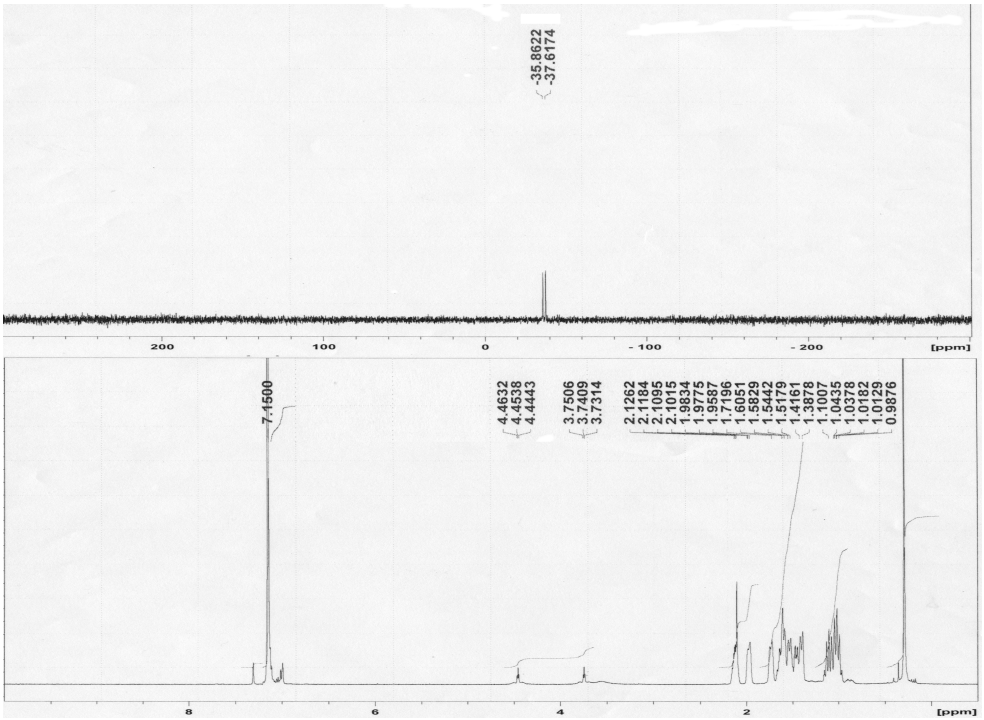

Figure C6: Proton-coupled ^{31}P (201 MHz, C_6D_6, 295 K) and ^{1}H (500 MHz, C_6D_6, 295 K) NMR spectra of **C1**.

Experimental.

Ga_2Br_4•2 $PHCy_2$ (**C1**): Dicyclohexylphosphine (2.5 mmol, 5 g of a 10% w/w solution in hexanes) was dissolved in toluene (5 mL). The solution was cooled to -78 °C and a cold (-78 °C) solution of GaBr•THF_n (6.05 mL of a 380 mM solution in toluene:THF 3:1) was added in one portion. The resultant orange solution was stirred at -78 °C for two hours, after which it was heated to 80 °C for 19h. The resulting dark brown solution was cooled to room temperature, the solvent removed *in vacuo* and the black residue dissolved in toluene (50 mL). The solution was filtered via cannula, concentrated, and cooled to -20

°C. After a week, colorless crystals of **C1** formed (40 mg, 0.047 mmol, 4% yield). ^{1}H NMR (500 MHz, C_6D_6) δ (ppm): 1.03-2.05 (44 H, Cy-H), 4.10 (dt, 2 H, $^{1}J_{(P-H)}$ = 352 Hz, $^{3}J_{(H-H)}$ = 5 Hz, P-H). ^{13}C NMR (125 MHz) δ (ppm): 25.5, 27.2, 30.3, 30.8, 31.1, 31.8. ^{31}P NMR (201.6 MHz) δ (ppm): -36.7 (d, J = 352 Hz).

Bibliography

(1) Greenwood, N. N.; Earnshaw, A. *Chemistry of the Elements*; Second Edition; 2nd ed. Elsevier., 1997.
(2) Surmann, P.; Zeyat, H. *Anal Bioanal Chem* **2005**, *383*, 1009–1013.
(3) Cui, C.; Roesky, H. W.; Schmidt, H.-G.; Noltemeyer, M.; Hao, H.; Cimpoesu, F. *Angew. Chem. Int. Ed.* **2000**, *39*, 4274–4276.
(4) Wright, R. J.; Brynda, M.; Power, P. P. *Angew. Chem. Int. Ed.* **2006**, *45*, 5953–5956.
(5) Wiberg, N.; Amelunxen, K.; Blank, T.; Nöth, H.; Knizek, J. **1998**, *17*, 5431–5433.
(6) Mocker, M.; Robl, C.; Schnöckel, H. *Angew. Chem. Int. Ed.* **1994**, *33*, 862–863.
(7) Bonyhady, S. J.; Collis, D.; Frenking, G.; Holzmann, N.; Jones, C.; Stasch, A. *Nat Chem* **2010**, *2*, 865–869.
(8) Wehmschulte, R. J.; Ruhlandt-Senge, K.; Olmstead, M. M.; Hope, H.; Sturgeon, B. E.; Power, P. P. *Inorg. Chem.* **1993**, *32*, 2983–2984.
(9) Uhl, W. *Z Naturforsch B* **1988**, *43*, 1113.
(10) Henke, P.; Pankewitz, T.; Kloepper, W.; Breher, F.; Schnöckel, H. *Angew. Chem. Int. Ed.* **2009**, *48*, 8141–8145.
(11) Wiberg, N.; Blank, T.; Kaim, W.; Schwederski, B. *Eur. J. Inorg. Chem.* **2000**, 1475–1481.
(12) Dohmeier, C.; Robl, C.; Tacke, M.; Schnöckel, H. *Angew. Chem. Int. Ed.* **1991**, *30*, 564–565.
(13) Mocker, M.; Robl, C.; Schnöckel, H. *Angew. Chem. Int. Ed.* **1994**, *33*, 1754–1755.
(14) Henke, P.; Huber, M.; Steiner, J.; Bowen, K.; Eichhorn, B.; Schnoeckel *J. Am. Chem. Soc.* **2009**, *131*, 5698–5704.
(15) Klemp, C.; Stosser, G.; Krossing, I.; Schnöckel, H. *Angew. Chem. Int. Ed.* **2000**, *39*, 3691–3694.
(16) Uffing, C.; Baum, E.; Koppe, R.; Schnöckel, H. *Angewandte Chemie* **1998**, *37*, 2397–2300.
(17) Purath, A.; Koppe, R.; Schnöckel, H. *Angew. Chem. Int. Ed.* **1999**, *38*, 2926–2928.
(18) Yang, P.; Koppe, R.; Duan, T.; Hartig, J.; Hadiprono, G.; Pilawa, B.; Keilhauer, I.; Schnöckel, H. *Angew. Chem. Int. Ed.* **2007**, *46*, 3579–3583.
(19) Henke, P.; Schnöckel, H. *Chem-Eur. J.* **2009**, *15*, 13391–13398.
(20) Henke, P.; Nils Trapp; Anson, C. E.; Schnöckel, H. *Angew. Chem. Int. Ed.* **2010**, *49*, 3146–3150.
(21) Purath, A.; Dohmeier, C.; Ecker, A.; Koppe, R.; Krautscheid, H.; Schnöckel, H.; Ahlrichs, R.; Stoermer, C.; Friedrich, J.; Jutzi, P. *J. Am. Chem. Soc.* **2000**, *122*, 6955–6959.
(22) Huber, M.; Hartig, J.; Koch, K. *Z Anorg Allg Chem* **2009**, *635*, 423–430.
(23) Klemp, C.; Bruns, M.; Gauss, J.; Haussermann, U.; Stosser, G.; van Wullen, L.;

Jansen, M.; Schnöckel, H. *J. Am. Chem. Soc.* **2001**, *123*, 9099–9106.
(24) Vollet, J.; Hartig, J.; Schnöckel, H. *Angew. Chem. Int. Ed.* **2004**, *43*, 3186–3189.
(25) Huber, M.; Schnepf, A.; Anson, C. E.; Schnöckel, H. *Angew. Chem. Int. Ed.* **2008**, *47*, 8201–8206.
(26) Kohnlein, H.; Purath, A.; Klemp, C.; Baum, E.; Krossing, I.; Stosser, G.; Schnöckel, H. *Inorg. Chem.* **2001**, *40*, 4830–4838.
(27) Ecker, A.; Weckert, E.; Schnöckel, H. *Nature* **1997**, *387*, 379–381.
(28) Hardman, N.; Eichler, B.; Power, P. *Chem Commun* **2000**, 1991–1992.
(29) Jutzi, P.; Neumann, B.; Reumann, G.; Stammler, H.-G. *Organometallics* **1998**, *17*, 1305–1314.
(30) Yu, Q.; Purath, A.; Donchev, A.; Schnöckel, H. *J. Organomet. Chem.* **1999**, *584*, 94–97.
(31) Slattery, J. M.; Higelin, A.; Bayer, T.; Krossing, I. *Angew. Chem. Int. Ed.* **2010**, *49*, 3228–3231.
(32) Hardman, N. J.; Wright, R. J.; Phillips, A. D.; Power, P. P. *J. Am. Chem. Soc.* **2003**, *125*, 2667–2679.
(33) Twamley, B.; Power, P. *Angew. Chem. Int. Ed.* **2000**, *39*, 3500–3503.
(34) Baker, R. J.; Bettentrup, H.; Jones, C. *Eur. J. Inorg. Chem.* **2003**, 2446–2451.
(35) Small, R.; Worrall, I. J. *Acta Crystallographica Section B: Structural …* **1982**, 250–251.
(36) Buchin, B.; Gemel, C.; Cadenbach, T.; Schmid, R.; Fischer, R. A. *Angew. Chem. Int. Ed.* **2006**, *45*, 1074–1076.
(37) Linti, G.; Köstler, W. *European journal of inorganic …* **1998**.
(38) Linti, G.; Zessin, T. *Dalton. Trans.* **2011**, *40*, 5591–5598.
(39) Uhl, W.; Layh, M.; Hildenbrand, T. *J. Organomet. Chem.* **1989**, *364*, 289–300.
(40) Hahn, I.; Reuter, H. *Chemische Berichte* **1996**, *129*, 1425.
(41) He, X.; Bartlett, R. A.; Olmstead, M. M.; Ruhlandt-Senge, K.; Sturgeon, B. E.; Power, P. P. *Angew. Chem. Int. Ed.* **1993**, *32*, 717–719.
(42) Linti, G.; Frey, R.; Köstler, W.; Urban, H. *Eur. J. Inorg. Chem.* **1996**, *129*, 561–569.
(43) Linti, G.; Köstler, W.; Piotrowski, H.; Rodig, A. *Angew. Chem. Int. Ed.* **1998**, *37*, 2209–2211.
(44) Seifert, A.; Linti, G. *Eur. J. Inorg. Chem.* **2007**, *2007*, 5080–5086.
(45) Jantschak, A. *J. Organomet. Chem.* **1998**.
(46) Linti, G. *J. Organomet. Chem.* **1996**, *520*, 107–113.
(47) Linti, G.; Rodig, A. *Chemical Communications* **2000**, 127–128.
(48) Wiberg, N.; Blank, T.; Westerhausen, M.; Schneiderbauer, S.; Schnöckel, H.; Krossing, I.; Schnepf, A. *Eur. J. Inorg. Chem.* **2002**, 351–356.
(49) Uhl, W.; Spies, T.; Haase, D.; Winter, R.; Kaim, W. *Organometallics* **2000**, *19*, 1128–1131.
(50) Loos, D.; Schnöckel, H.; Fenske, D. *Angew. Chem. Int. Ed.* **1993**, *32*, 1059–1060.
(51) Baum, E.; Stosser, G.; Schnöckel, H. *ZEITSCHRIFT FUR …* **2002**.
(52) Loos, D.; Baum, E.; Ecker, A.; Schnöckel, H.; Downs, A. J. *Angew. Chem. Int. Ed.* **1997**, *36*, 860–862.

(53) Uhl, W.; Voß, M.; Luftmann, H. *Chem Commun* **2009**, 6854.
(54) Duan, T.; Henke, P.; Stosser, G.; Zhang, Q.-F.; Schnöckel, H. *J. Am. Chem. Soc.* **2010**, *132*, 1323–1327.
(55) Hartig, J.; Steiner, J.; Stösser, A.; Schnöckel, H. *Chem-Eur. J.* **2007**, *13*, 4475–4482.
(56) Schnepf, A.; Koppe, R.; Schnöckel, H. *Angew. Chem. Int. Ed.* **2001**, *40*, 1241–.
(57) Doriat, C. U.; Friesen, M.; Baum, E.; Ecker, A.; Schnöckel, H. *Angew. Chem. Int. Ed.* **1997**, *36*, 1969–1971.
(58) Wiberg, N.; Blank, T.; Noth, H. *Eur. J. Inorg. Chem.* **2002**, 929–934.
(59) Uhl, W. *Polyhedron* **2002**, *21*, 511–518.
(60) Köstler, W.; Linti, G. *Angew. Chem. Int. Ed.* **1997**, 2644–2646.
(61) Uhl, W.; Cuypers, L.; Harms, K.; Kaim, W.; Wanner, M.; Winter, R.; Koch, R.; Saak, W. *Angew. Chem. Int. Ed.* **2001**, *40*, 566–568.
(62) Uhl, W.; Cuypers, L.; Kaim, W.; Schwederski, B.; Koch, R. *Angew. Chem. Int. Ed.* **2003**, *42*, 2422–2423.
(63) Duan, T.; Stosser, G. *Angew. Chem. Int. Ed.* **2005**.
(64) Kehrwald, M.; Köstler, W.; Rodig, A.; Linti, G.; Blank, T.; Wiberg, N. *Organometallics* **2001**, *20*, 860–867.
(65) Schnepf, A.; Stosser, G.; Koppe, R.; Schnöckel, H. *Angew. Chem. Int. Ed.* **2000**, *39*, 1637–.
(66) Stosser, G.; Schnöckel, H. *Zeitschrift für anorganische ...* **2004**, *630*, 1879–1882.
(67) Donchev, A.; Schnepf, A.; Stosser, G.; Baum, E.; Schnöckel, H.; Blank, T.; Wiberg, N. *Chem-Eur. J.* **2001**, *7*, 3348–3353.
(68) A Schnepf; G Stösser, A.; Schnöckel, H. *J. Am. Chem. Soc.* **2000**, *122*, 9178–9181.
(69) Steiner, J.; Stosser, G.; Schnöckel, H. *Angew. Chem. Int. Ed.* **2004**, *43*, 6549–6552.
(70) Schnepf, A.; Koppe, R.; Weckert, E.; Schnöckel, H. *Chem-Eur. J.* **2004**, *10*, 1977–1981.
(71) Schnepf, A.; Stosser, G.; Schnöckel, H. *Angew. Chem. Int. Ed.* **2002**, *41*, 1882–1884.
(72) Schnepf, A.; Weckert, E.; Linti, G.; Schnöckel, H. *Angew. Chem. Int. Ed.* **1999**, *38*, 3381–3383.
(73) Hartig, J.; Stösser, A.; Hauser, P.; Schnöckel, H. *Angew. Chem. Int. Ed.* **2007**, *46*, 1658–1662.
(74) Hartig, J.; Klöwer, F.; Rinck, J.; Unterreiner, A.-N.; Schnöckel, H. *Angew. Chem. Int. Ed.* **2007**, *46*, 6549–6552.
(75) Duan, T.; Baum, E.; Burgert, R.; Schnöckel, H. *Angew. Chem. Int. Ed.* **2004**, *43*, 3190–3192.
(76) Rodig, A.; Linti, G. *Angew. Chem. Int. Ed.* **2000**, *39*, 2952–2954.
(77) Steiner, J.; Stosser, G.; Schnöckel, H. *Angew. Chem. Int. Ed.* **2004**, *43*, 302–305.
(78) Schnepf, A.; Schnöckel, H. *Angew. Chem. Int. Ed.* **2001**, *40*, 712–715.
(79) Woodward, L. A.; Greenwood, N. N.; Hall, J. R.; Worrall, I. J. *J. Chem. Soc.* **1958**, 1505–1508.

(80) Beamish, J. C.; Wilkinson, M.; Worrall, I. J. *Inorg. Chem.* **1978**, *17*, 2026–2027.
(81) Green, M. *Polyhedron* **1990**, *9*, 2763–2765.
(82) Baker, R.; Jones, C. *Dalton. Trans.* **2005**, 1341–1348.
(83) Hoberg, H.; Krause, S. *Angew. Chem. Int. Ed.* **1976**, *15*, 694–694.
(84) Hiller, W.; Klinkhammer, K.-W.; Wagner, J.; Uhl, W. *Angew. Chem. Int. Ed.* **1991**, *30*, 179–180.
(85) Uhl, W. *J. Organomet. Chem.* **1989**, *368*, 139–154.
(86) Zhu, H.; Chai, J.; Fan, H.; Roesky, H. W.; He, C.; Jancik, V.; Schmidt, H.-G.; Noltemeyer, M.; Merrill, W. A.; Power, P. P. *Angew. Chem. Int. Ed.* **2005**, *44*, 5090–5093.
(87) Hardman, N. J.; Cui, C.; Roesky, H. W.; Fink, W. H.; Power, P. P. *Angew. Chem. Int. Ed.* **2001**, *40*, 2172–2174.
(88) Zhu, H.; Chai, J.; Chandrasekhar, V.; Roesky, H. W.; Magull, J.; Vidovic, D.; Schmidt, H.-G.; Noltemeyer, M.; Power, P. P.; Merrill, W. A. *J. Am. Chem. Soc.* **2004**, *126*, 9472–9473.
(89) Zhu, H.; Chai, J.; Jancik, V.; Roesky, H. W.; Merrill, W. A.; Power, P. P. *J. Am. Chem. Soc.* **2005**, *127*, 10170–10171.
(90) Dohmeier, C.; Schnöckel, H.; Robl, C.; Schneider, U.; Ahlrichs, R. *Angew. Chem. Int. Ed.* **1994**, *33*, 199–200.
(91) Stephan Schulz; Roesky, H. W.; Hans Joachim Koch; George M Sheldrick; Dietmar Stalke; Annja Kuhn *Angew. Chem. Int. Ed.* **1993**, *32*, 1729–1731.
(92) Uffing, C.; Achim Ecker; Koppe, R.; Schnöckel, H. *Organometallics* **1998**, *17*, 2373–2375.
(93) Nguyen, T.; Sutton, A. D.; Brynda, M.; Fettinger, J. C.; Long, G. J.; Power, P. P. *Science* **2005**, *310*, 844–847.
(94) Su, J.; Li, X.-W.; Crittendon, R. C.; Robinson, G. H. *J. Am. Chem. Soc.* **1997**, *119*, 5471–5472.
(95) Li, X.-W.; Xie, Y.; Schreiner, P. R.; Gripper, K. D.; Crittendon, R. C.; Campana, C. F.; Schaefer, H. F.; Robinson, G. H. *Organometallics* **1996**, *15*, 3798–3803.
(96) Quillian, B.; Wei, P.; Wannere, C. S.; Schleyer, P. V. R.; Robinson, G. H. *J. Am. Chem. Soc.* **2009**, *131*, 3168–3169.
(97) Tacke, M.; Schnöckel, H. *Inorg. Chem.* **1989**, *28*, 2895–2896.
(98) Schnöckel, H. *Chem. Rev.* **2010**, *110*, 4125–4163.
(99) Wegner, G.; Berger, R.; Schier, A.; Schmidbaur, H. *Organometallics* **2001**, *20*, 418–423.
(100) Purath, A.; Koppe, R.; Schnöckel, H. *Chem Commun* **1999**, 1933–1934.
(101) Kohnlein, H.; Stosser, G.; Baum, E.; Mollhausen, E.; Huniar, U.; Schnöckel, H. *Angew. Chem. Int. Ed.* **2000**, *39*, 799–801.
(102) Schnepf, A.; Jee, B.; Schnöckel, H.; Weckert, E.; Meents, A.; Lubbert, D.; Herrling, E.; Pilawa, B. *Inorg. Chem.* **2003**, *42*, 7731–7733.
(103) Linti, G.; Seifert, A. *Dalton. Trans.* **2008**, 3688–3693.
(104) Wyckoff, R. *Crystal Structures*; Interscience: New York, NY, 1963.
(105) Wernick, S.; Pinner, R. *The surface treatment and finishing of aluminium and its alloys*; 1972; p. 792.

(106) Kasai, P.; Jones, P. *J. Am. Chem. Soc.* **1984**, *106*, 8018–8020.
(107) Balaji, V.; Sunil, K. K.; Jordan, K. D. *Chem. Phys. Lett.* **1987**, *136*, 309–313.
(108) Qian, B.; Ward, D. L.; Smith, M. R. *Organometallics* **1998**, *17*, 3070–3076.
(109) Uhl, W. *J. Organomet. Chem.* **1993**, *454*, 9–13.
(110) Baker, R.; Davies, A.; Jones, C. *J. Organomet. Chem.* **2002**, *656*, 203–210.
(111) McGrady, G. S.; Turner, J. F. C.; Ibberson, R. M.; Prager, M. *Organometallics* **2000**, *19*, 4398–4401.
(112) Klemp, C.; Koppe, R.; Weckert, E.; Schnöckel, H. *Angew. Chem. Int. Ed.* **1999**, *38*, 1739–1743.
(113) Jiang, W.; Knobler, C. B.; Hawthorne, M. F. *Angew. Chem. Int. Ed.* **1996**, *35*, 2536–2537.
(114) Vollet, J.; Burgert, R.; Schnöckel, H. *Angew. Chem. Int. Ed.* **2005**, *44*, 6956–6960.
(115) Hadiprono, G. Dissertation, University Karsruhe, 2005.
(116) Sheldrick, G. M.; Sheldrick, W. S. *J. Chem. Soc., A* **1969**, 2279.
(117) Köhnlein, H.; Purath, A.; Klemp, C.; Baum, E.; Krossing, I.; Stösser, G.; Schnöckel, H. *Inorg. Chem.* **2001**, *40*, 4830–4838.
(118) Stender, M.; Eichler, B. E.; Hardman, N. J.; Power, P. P.; Prust, J.; Noltemeyer, M.; Roesky, H. W. *Inorg. Chem.* **2001**, *40*, 2794–2799.
(119) Sharma, B. D.; Donohue, J. *Z. Kristallogr.* **1962**, *117*, 293–300.
(120) Çoban, S. Diplomarbeit, Universität Karlsruhe, 1999.
(121) Hardman, N. J.; Wright, R. J.; Phillips, A. D.; Power, P. P. *Angew. Chem. Int. Ed.* **2002**, *41*, 2842–2844.
(122) Beamish, J. C.; Small, R. W. H.; Worrall, I. J. *Inorg. Chem.* **1979**, *18*, 220–223.
(123) Brown, K. L.; Hall, D. *J. Chem. Soc. Dalton Trans.* **1973**, 1843–1845.
(124) Uhl, W.; Schütz, U.; Kaim, W.; Waldhör, E. *J. Organomet. Chem.* **1995**, *501*, 79–85.
(125) Mayo, D. H.; Peng, Y.; Zavalij, P.; Eichhorn, B. W. *Acta Crystallographica E*.
(126) Wallwork, S. C.; Worrall, I. J. *J. Chem. Soc.* **1965**, 1816–1820.
(127) Atwood, D. A.; Atwood, V. O.; Cowley, A. H.; Jones, R. A.; Atwood, J. L.; Bott, S. G. *Inorg. Chem.* **1994**, *33*, 3251–3254.
(128) Greenwood, N. N.; Earnshaw, A. **1998**.
(129) Su, J.; Li, X.-W.; Crittendon, R. C.; Campana, C. F.; Robinson, G. H. *Organometallics* **1997**, *16*, 4511–4513.
(130) Woodward, L.; Garton, G. *J. Chem. Soc.* **1956**, 3723–3726.
(131) Burgert, R.; Stosser, G.; Schnöckel, H. *Eur. J. Mass Spectrom.* **2005**.
(132) Koch, K.; Burgert, R.; Stosser, G.; Schnöckel, H. In *European Journal of Mass Spectrometry*; 2005; Vol. 11, pp. 469–474.
(133) Gauss, J.; Schneider, U.; Ahlrichs, R.; Dohmeier, C.; Schnöckel, H. *J. Am. Chem. Soc.* **1993**, *115*, 2402–2408.
(134) Bono, D.; Hartig, J.; Huber, M.; Schnoeckel, H.; deJOngh, L. J. *J Clust Sci* **2007**, *18*, 319–331.
(135) Bakharev, O.; Bono, D.; Brom, H.; Schnepf, A.; Schnöckel, H.; de Jongh, L. *Phys. Rev. Lett.* **2006**, *96*.
(136) Bono, D.; Schnepf, A.; Hartig, J.; Schnöckel, H.; Nieuwenhuys, G.; Amato, A.; de Jongh, L. *Phys. Rev. Lett.* **2006**, *97*.

(137) Dohmeier, C.; Loos, D.; Schnöckel, H. *Angew. Chem. Int. Ed.* **1996**, *35*, 129–149.
(138) Pacher, A.; Schrenk, C.; Schnepf, A. *J. Organomet. Chem.* **2010**, *695*, 941–944.
(139) Schnepf, A. *Eur. J. Inorg. Chem.* **2008**, 1007–1018.
(140) Timms, P. *Acc. Chem. Res.* **1973**, *6*, 118–123.
(141) Yoder, L. *Journal of Industrial & Engineering Chemistry* **1919**, *11*, 755–755.
(142) Luo, Y.; Yingming Yao; Qi Shen; Sun, J.; Weng, L. *J. Organomet. Chem.* **2002**, *662*, 144–149.
(143) Kenney, A. P.; Yap, G. P. A.; Richeson, D. S.; Barry, S. T. *Inorg. Chem.* **2005**, *44*, 2926–2933.
(144) Coles, M.; Swenson, D.; Jordan, R.; Young, V. *Organometallics* **1997**, *16*, 5183–5194.
(145) *Molecular Clusters of the Main Group Elements*; Driess, M.; Nöth, H., Eds. Driess: Molecular Clusters O-BK; Wiley-VCH Verlag GmbH & Co. KGaA: Weinheim, FRG, 2005; pp. i–xvi.
(146) Pu, L.; Phillips, A. D.; Richards, A. F.; Stender, M.; Simons, R. S.; Olmstead, M. M.; Power, P. P. *J. Am. Chem. Soc.* **2003**, *125*, 11626–11636.
(147) Green, S.; Jones, C.; Stasch, A. *Science* **2007**, *318*, 1754–1757.
(148) Stasch, A.; Jones, C. *Dalton. Trans.* **2011**, *40*, 5659–5672.
(149) Schnepf, A. *Chem Soc Rev* **2007**, *36*, 745–758.
(150) Evans, D. F. *J. Chem. Soc.* **1959**, 2003–2005.
(151) Bain, G. A.; Berry, J. F. *J. Chem. Educ.* **2008**, *85*, 532.
(152) Risha, G.; Connell, T., Jr; Yetter, R. *Aluminum-ice (ALICE) propellants for hydrogen generation and propulsion*; 45th AIAA/ASME/SAE/ASEE Joint Propulsion Conference & Exhibit, 2009.
(153) Jouet, R. J.; Carney, J. R.; Granholm, R. H.; Sandusky, H. W.; Warren, A. D. *Mats. Sci. Tech.* **2006**, *22*, 422–429.
(154) Lightstone, J.; Hooper, J.; Stoltz, C.; Wilson, B.; Mayo, D.; Eichhorn, B.; Bowen, K. *Bulletin of the American Physical Society* **2011**, *Volume 56, Number 6*.
(155) Peng, Y.; Ellis, B. D.; Wang, X.; Fettinger, J. C.; Power, P. P. *Science* **2009**, *325*, 1668–1670.